UNIVERSITÀ DEGLI STUDI DI NAPOLI
FEDERICO II

SCUOLA POLITECNICA E DELLE SCIENZE DI BASE

CORSO DI LAUREA MAGISTRALE IN INGEGNERIA AEROSPAZIALE

DIPARTIMENTO DI INGEGNERIA INDUSTRIALE

MASTER THESIS

AIRCRAFT DIRECTIONAL CONTROL CHARACTERISTICS THROUGH CFD ANALYSES

SUPERVISOR:
Prof. Eng.
FABRIZIO NICOLOSI

CANDIDATE:
CIRO SCALZO
Matr.: M53/000512

CO-SUPERVISOR:
Dr. Eng.
CILIBERTI DANILO

ANNO ACCADEMICO 2015/2016

Fall seven times and stand up eight.

-Japanese proverb

Success is the sum of small efforts, repeated day in and day out.

-Robert Collier

Dedicated to all those who have always believed in me.

Dedicato a tutti quelli che hanno sempre creduto in me.

Abstract

In the present state of the art, the evaluation of aircraft rudder effectiveness in the preliminary design stage is carried out with semi-empirical methods. The main objective of the present thesis work was to build an aerodynamic database to develop a new method for the calculation of rudder effectiveness from the results of CFD RANS analyses, performed on different vertical tail planes geometries. Discrepancies among semi-empirical methods and their underprediction of rudder effectiveness with respect to numerical analyses and wind tunnel tests performed of certain planforms made the choice to attempt a different approach through viscous Navier-Stokes simulations. The main purpose of such analyses was to highlight any functional dependencies of the rudder effectiveness by the geometrical characteristics of the vertical tail plane, such as chord ratio, taper ratio, sweep angle, and rudder span extension. For the realization of the above-mentioned aerodynamic database, numerical analyses of 40 different vertical tail planes geometries have been carried out. RANS simulations have been performed with STAR-CCM+ on the isolated vertical tail planforms at different sideslip and rudder deflection angles. For each planform 7 rudder deflection and, for most of them, 20 sideslip angles have been simulated, yielding to about 4300 runs. The reference geometry for these analyses had been previously investigated at the Department of Industrial Engineering (DII), concerning the research on aircraft directional stability and control.

The results of these numerical analyses have conducted to the implementation of a new method for the calculation of the rudder effectiveness. This method considers the main geometric parameters describing the planform of a vertical tail (stabilizer and rudder) and it is of considerable interest, since it provides results that agree with recent numerical and experimental analyses on regional and general aviation airplanes. Experimental tests are to be conducted in the future on the most relevant geometries to validate the method.

Sommario

Allo stato attuale dell'arte, la valutazione dell'efficacia del timone di un velivolo in fase di progetto preliminare viene effettuata con metodi semi-empirici. L'obiettivo principale del presente lavoro di tesi era quello di costruire un database aerodinamico per sviluppare un nuovo metodo per il calcolo dell'efficacia del timone a partire dai risultati di analisi CFD RANS, eseguite su differenti geometrie di piano di coda verticale. Le discrepanze tra i metodi semi-empirici e la loro sottostima dell'efficacia del timone, rispetto alle analisi numeriche ed i test in galleria del vento eseguiti su alcune forme in pianta, hanno portato alla decisione di tentare un approccio differente attraverso simulazioni di flusso viscoso alla Navier-Stokes. Lo scopo principale di tali analisi era quello di evidenziare eventuali dipendenze funzionali dell'efficacia del timone dalle caratteristiche geometriche del piano di coda verticale, come l'angolo di freccia, il rapporto di rastremazione e l'estensione del timone lungo l'apertura. Per la realizzazione del database aerodinamico sopracitato, sono state effettuate delle analisi numeriche su 40 differenti geometrie di piano di coda verticale. Sono state eseguite simulazioni RANS con il software STAR-CCM+ su forme in pianta di piani di coda verticali isolati a diversi angoli di derapata e deflessione del timone. Per ogni forma in pianta sono state simulate 7 deflessioni del timone e, per la maggior parte di esse, 20 angoli di derapata, arrivando a circa 4300 simulazioni totali. La geometria di riferimento per queste analisi era stata precedentemente analizzata presso il Dipartimento di Ingegneria Industriale (DII), nell'ambito di ricerca riguardante la stabilità ed il controllo direzionale di un velivolo.

I risultati di queste analisi numeriche hanno condotto alla realizzazione di un nuovo metodo per il calcolo dell'efficacia del timone. Questo metodo considera i principali parametri geometrici che descrivono la forma in pianta di un piano di coda verticale (stabilizzatore e timone) ed è di notevole interesse, in quanto fornisce risultati concordanti con recenti analisi numeriche e sperimentali su velivoli regionali e di aviazione generale. In futuro dovranno essere condotte prove sperimentali sulle geometrie più rilevanti per validare il metodo.

ACKNOWLEDGMENTS

There are several people to whom it is right to give my heartfelt thanks at the end of my academic career. First of all, I would like to thank Prof. Fabrizio Nicolosi for giving me the opportunity to work at this thesis project, which has strengthened even more my desire to become a good engineer. But most of all I would like to thank Eng. Danilo Ciliberti, for the incredible support given to me in carrying out all the activities necessary to the writing of this thesis. His kindness and his availability were out of the ordinary. A great person behind a great engineer.

I feel duty also to extend wholeheartedly my thanks to all the members of DAF research group: Eng. Pierluigi Della Vecchia for his incredible knowledge and great availability, Eng. Salvatore Corcione for all the moments spent to think about the players to deploy in fantasy football (and, of course, also for constantly making available, in times of difficulty, his time and his great engineering skills), Eng. Vincenzo Cusati for his innate kindness and Eng.s Luca Stingo, Manuela Ruocco and Vittorio Trifari for sharing with me many days and, above all, living space. I am sure that each of you will achieve his goals, and I wish you sincerely the best.

I also want to thank my family: each of you has a role and a special place in my heart. Thanks to my mother for teaching me the meaning of sacrifice and perseverance and for putting in first place in the last 25 years only and only the good of his children. Thanks to my dad for teaching me to be patient and to live life more carefree (maybe not too carefree...). Finally, thanks to my twin brother, the other side of the coin, for his constant encouragement. I would not trade you for any family in the world.

Another special thanks goes to Grieco family, Michele (with whom I share a passion for airplanes), Ester and Fabiana for the love and support they have always given me. Thanks also to Grandma Maria for her constant interest and for her incredible availability. You welcomed me like a second family and I shall be forever grateful.

Thanks to all the people (friends and family) with whom I have forged close relations over the years and with whom I shared wonderful moments. Make a list would be complicated, but anyone who has ever crossed my path and has walked with me, even only for a stretch, holds a special place in my heart.

Finally, thanks to Alessia, the woman I love, my star, my perfect silence. Thanks for all the comprehension and sacrifices, for being next to me all the time, for everything you have tolerated only for me and for always putting my interests above all things. To me, my love, you are perfect.

SUMMARY

FIGURE INDEX

TABLE INDEX

1. Introduction

1.1 Phenomenology

1.1.1 Concept of stability and equilibrium

The problems of stability and control play a fundamental role in the design of an aircraft. In the strict sense, the static stability expresses the capability of a system to restore an equilibrium condition previously disrupted by an external cause. It is therefore strictly necessary to define the concept of equilibrium, from which the concept of stability will be clearly defined. There are two different types of equilibrium, from which derive two different types of stability, distinguished into:

- **Static Equilibrium**, which condition is obtained when the resultant of all forces and (external) moments is equal to zero. This condition appears to exist only in the case of uniform rectilinear flight (motion in an inertial reference frame);
- **Dynamic Equilibrium**, which condition is obtained each instant during the phase of maneuvered flight; because of the effect of accelerations, inertial forces and moments rise, which have to be balanced in each instant of flight (non-inertial reference frame).

From these two different definitions of equilibrium, the related definitions of stability derive:

- **Static Stability,** which expresses the tendency of the system to return to the initial equilibrium condition after a small initial perturbation (by *small* it is meant that the disturbance must not take the system out of the linear range);
- **Dynamic Stability,** which represents the actual capacity of the system to return to a pre-existing equilibrium condition following a small perturbation.

A static stability does not necessarily imply a dynamic stability, as it can be easily seen from the following example, summarized in Figure 1.

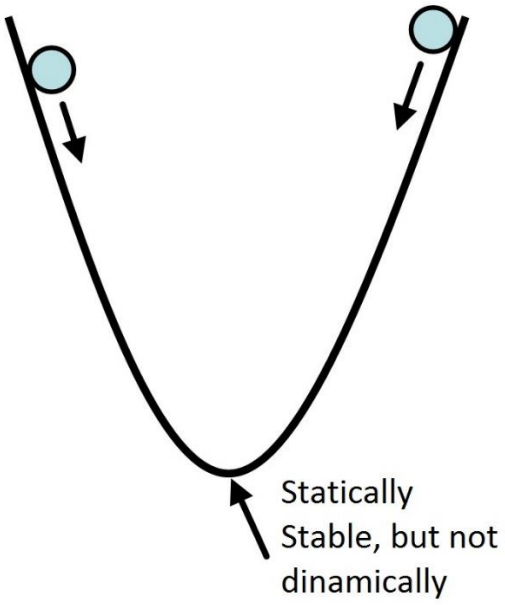

Figure 1: Example of static stability which not implies dynamic stability

In this example, after a small perturbation, which retains the ball within the basin, the system tends to return to the initial equilibrium position and, therefore, is statically stable; but, if the friction forces are not taken into account, the oscillation of the ball is perennial, and then the system is not dynamically stable (the dynamic stability evaluates the damping of the response).

After this quick overview, it is possible to focus on the problem of interest of this thesis.

1.1.2 Vertical tail plane design with reference to stability and control

This thesis deals with vertical tail planes, which provide directional stability and control. A vertical plane is usually made up of two parts: a fixed wing, called *fin*, and a plain flap, the *rudder* (Figure 2a). The fin provides directional stability, while the rudder is the directional control surface.

There is a large variety of tail shapes, often denoted by the letters whose shapes they resemble in front view [1], for instance T, V, H, Y (see Figure 2b).

- The standard configuration with roots of both horizontal and vertical surfaces attached directly to the fuselage is ‘structurally convenient’. Aerodynamic interference with the

fuselage and horizontal tail increase the effectiveness of the vertical tail. However large areas of the tails are affected by the converging fuselage flow, which can reduce the local dynamic pressure;

- A T-tail is often chosen to move the horizontal tail away from engine exhaust and to reduce aerodynamic interference. The vertical tail is in his most effective position, being 'end-plated' on one side by the fuselage and on the other by the horizontal tail. The disadvantages of this arrangement include higher vertical fin loads, potential flutter problems and deep-stall;
- V-tails combine functions of horizontal and vertical tails. They are sometimes chosen because of their increased ground clearance, reduced number of surface intersections, or novel look, but require mixing of rudder and elevator controls and often exhibit reduced control authority in combined yaw and pitch maneuvers;
- H-tails or twin tails use the vertical surfaces as endplates for the horizontal tail, increasing its effectiveness and thus saving vertical tail span. Sometimes are used on propeller aircraft to re-duce the yawing moment associated with propeller slipstream impingement on the vertical tail but more complex control link-ages and reduced ground clearance discourage their more wide-spread use;
- Y-shaped tails have been used when the downward projecting vertical surface can serve to protect a pusher propeller from ground strikes.

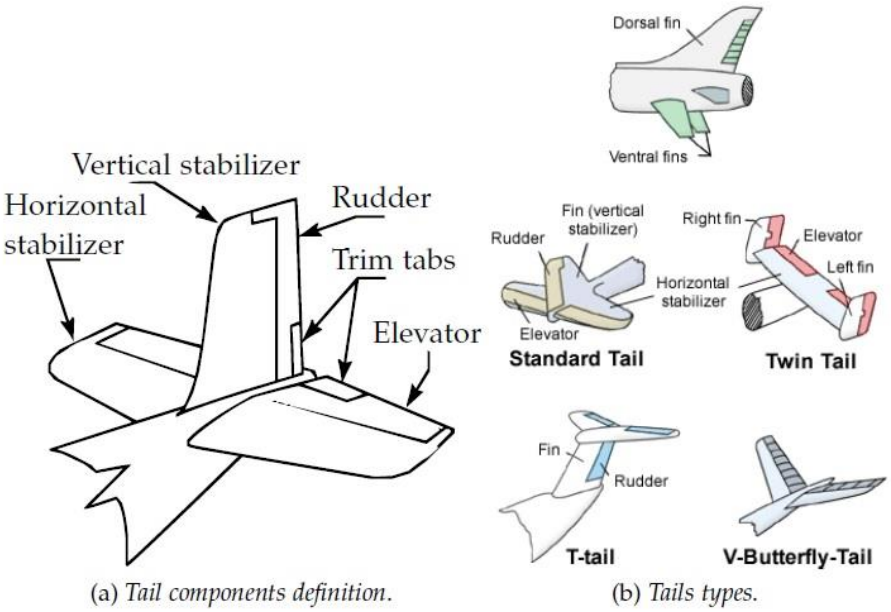

Figure 2: Geometry of various tail arrangements [2],[3].

The problem of directional stability and control is first to ensure that the airplane will tend to remain in equilibrium at zero sideslip (angle between the relative wind and the longitudinal plane of symmetry of the airplane) and second to provide a control to maintain zero sideslip during maneuvers that introduce moments tending to produce sideslip [4]. Although a tailless airplane is realizable, like the flying wing, whose directional stability is given by the swept wing and pushing propellers or an active control of the lateral control surfaces, the vertical tail plane is the main component of directional stability.

From the dynamic point of view, the role of the vertical tail is to provide yaw damping. If the vertical tail (volume coefficient) dimensions are too small, for a given dihedral effect or lateral stability, the aircraft tends to oscillate in yaw as the pilot gives rudder or aileron inputs. This tendency is called dutch roll (see Figure 3) and makes precise directional control difficult [5].

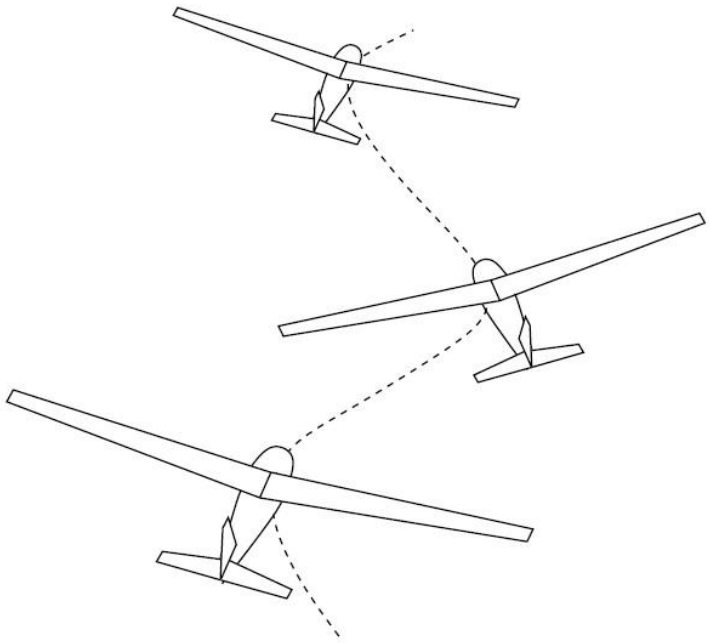

Figure 3: Dutch roll oscillation tendency from insufficient vertical tail volume [5].

Extreme flight conditions often set design requirements for tail surfaces, like minimum control speed with One Engine Inoperative (OEI) or maximum cross-wind capability: stability and control must be ensured even in very large angles of sideslip, up to 25° [7]. Similar requirements are dictated by the European Aviation Safety Agency (EASA) in Europe with Certification Specification, part 25.

Design of vertical planes depends on the type of airplane (and so the flow regime), engine numbers and position, wing-fuselage and horizontal tail position [6]. These factors affect the stability derivatives, which represent the variation of aerodynamic coefficients with the independent variable, the angle of sideslip β. It is somewhat complicated since it involves asymmetrical flow behind the wing-fuselage combination and lateral cross-control (lateral control is provided by ailerons, but side forces on vertical planes cause also a rolling moment).

The following design requirements can be formulated for vertical tail planes [7]:

1. They shall provide a sufficiently large contribution to static and dynamic stability, that is the side-force derivative of the isolated vertical tail

$$C_{Y_{\beta,V}} = C_{L_{\alpha,V}} \cdot \frac{S_V}{S} \qquad (1.1)$$

has to be determined. The vertical tail directional stability derivative is $C_{N_{\beta,V}}$, which is the yawing moment coefficient due to sideslip, however it can be shown that it depends from the coefficient just defined. If a high lift gradient is desirable the aspect ratio should be the largest possible with the minimum sweep. In equation (1.1), $C_{L_{\alpha,V}}$ represents the lift-curve slope of the vertical tail plane, while S_V represents the surface of the above-mentioned plane. Finally, with S is indicated the reference surface used to a-dimension the aerodynamic coefficients (usually is the wing surface).

2. The same can be stated for sufficient control capability. Moreover control should be possible with acceptable control force

$$F = C_h \frac{\rho V^2}{2} S_C \, c_c \qquad (1.2)$$

where C_h indicates the hinge moment coefficient, ρ the density, V the velocity, S_c and c_c the surface and the chord of the control surface.

3. High angles of sideslip (up to 25°) can be reached and this condition is more serious when flying in possible icing conditions. In this case, a low aspect ratio is required and sweep is beneficial (they delay the stall at higher angle of sideslip, but reduce the lift gradient).
4. Equilibrium has to be achieved in all flight conditions. This gives specific requirements on tail surface areas and on the maximum lift coefficient with various amount of control surface deflection and should include the effect of ice roughness.
5. A high aspect ratio has an adverse effect on weight. Also, for T-tails the flutter analysis requires extra care.
6. Excessive taper ratio may lead to premature tip stall. On the other hand, tapering leads to lower height.

So a compromise in high lift gradient and low aspect ratio and taper ratio must be considered. Some indications come from Raymer [8] and are reported in a general fashion in and in function of the wing parameters in Table 2.

	Horizontal tail		Vertical tail	
	A	λ	A	λ
Fighter	3 - 4	0.2 - 0.4	0.6 - 1.4	0.2 - 0.4
Sail plane	6 - 10	0.3 - 0.5	1.5 - 2.0	0.4 - 0.6
Others	3 - 5	0.3 - 0.6	1.3 - 2.0	0.3 - 0.6
T-tail	—	—	0.7 - 1.2	0.6 - 1.0

Table 1: Tail aspect ratio (A) and taper ratio guideline (λ), by Raymer [8].

Wing	Vertical	Comment
Λ_{LE}	35° - 55°	Tail stall later than wing and has a higher critical Mach number.
A	1.3 - 2	Must be lighter than wing.
λ	0.3 - 0.6	Close to an elliptical load and easy to manufacture.
t/c	9% - 12%	Usually similar to wing section's relative thickness.
$\bar{c}_c/c_v$	25% - 50%	Typical plain flaps with same taper ratio of tailplane.

Table 2: Sizing of the vertical stabilizer in function of the wing parameters, by Ramer [8].

1.1.3 Directional Stability

Directional stability is the capability of the vehicle to put its nose in the wind, like a weather vane. If the vane is rotated so its nose points, say, right (and the tail points left) intuition tells that its tail will generate lift that points to the right, in the positive y-direction (see Figure 4). This, in turn, generates a moment whose tendency is to rotate the nose left and align it with the wind.

Since the moment corrects the alignment, it is said to be restoring. The restoring moment is negative because the right-hand rule, the resulting rotation is analogous to grabbing around the z-axis with

the right hand to rotate it with the right thumb pointing upward e in the negative z-direction. The opposite holds true if the weather vane is rotated nose left and a positive moment (thumb pointing down) is then required to bring the nose right to the initial position.

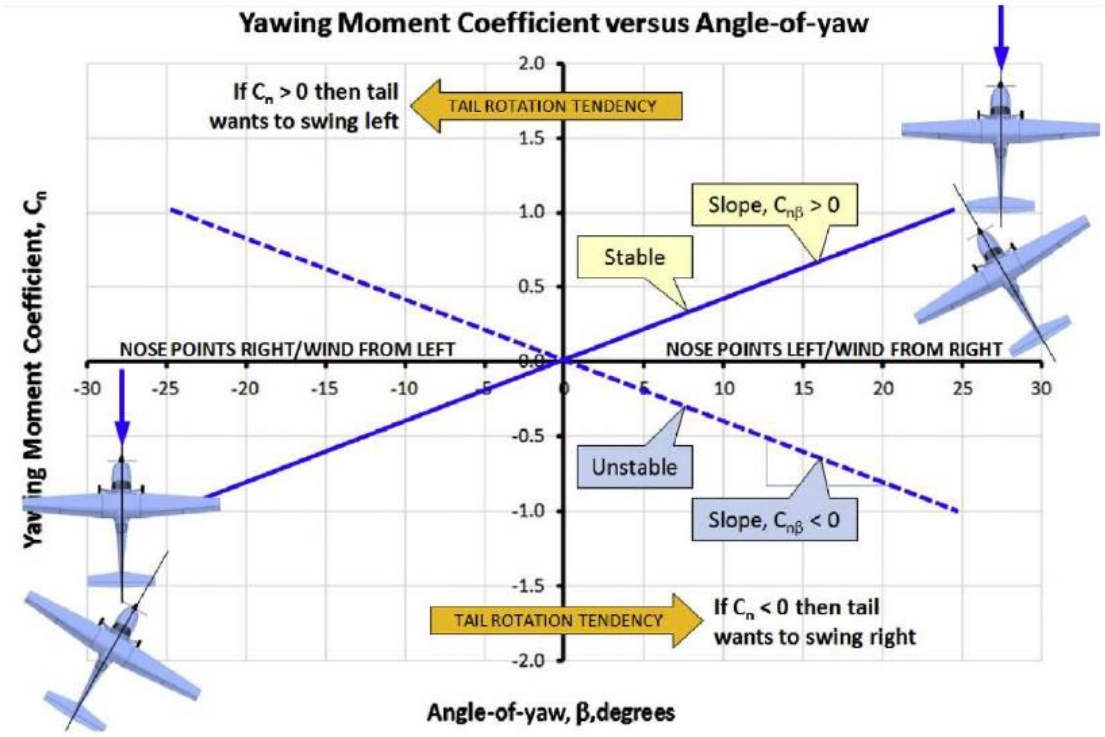

Figure 4: Requirements for static directional stability of an aircraft [9].

In section 1.1.1, it has been introduced the concept of stability and equilibrium in a general sense. Now, after introducing the concept of directional stability, it is then possible to reformulate the previously expressed concepts.

So, in general, if, for example, the airplane is statically stable and the perturbation resulted in an increased angle of attack, there can be three cases:

- in the first case the aircraft responds by decreasing the angle of attack to a value less than the initial equilibrium configuration, leading to a subsequent reaction that further increases the angle of attack, but with subsequent oscillations amplitude gradually smaller, tending to bring it back to the initial equilibrium state. In this case, it is said that the airplane is

dynamically stable and, once trimmed in its equilibrium position, requires no additional corrective action by the pilot to maintain the flight configuration set;

- if the aircraft responds by continuing to oscillate around the position of equilibrium with constant amplitude, it has a neutral dynamic stability;
- on the contrary, if the oscillations around the initial position increase in amplitude over time, it is a dynamically unstable aircraft.

Considering that the motion of an aircraft can be divided into three basic dynamics, longitudinal, lateral, and directional, it is easy to understand that the above-mentioned phenomena, which determine whether or not the system is stable, concern precisely these three dynamics.

The directional stability involves the degrees of freedom related to the forward direction, so the yaw (see Figure 5). Actually considering that coupling phenomena, which also involve the lateral degrees of liberty as roll, arise, these two aspects of stability merge into a single issue, which is called lateral-directional stability. The present thesis work is concerned only on the directional stability and control, so the focus will be pointed on a specific aspect for the design with respect to performance of directional control; therefore, these coupling phenomena will be neglected. In Figure 5 it is also possible to note two different yawing angles, therefore it is important to observe that from an analytical point of view the sideslip angle β is like the yaw angle φ, but in the opposite way.

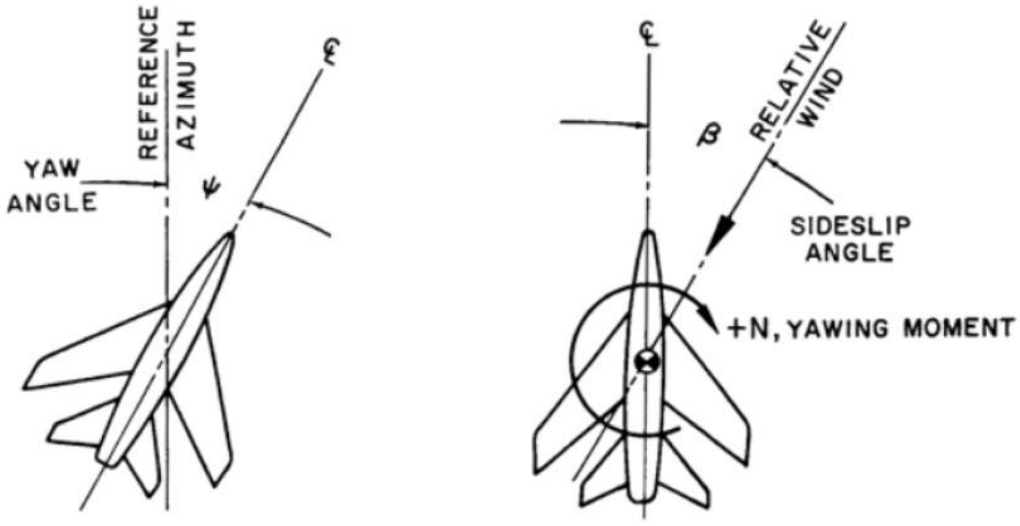

Figure 5: Directional Dynamics.

In general, an airplane is said to be yawed if its centerline is not parallel to the x-z-plane (see Figure 6). This implies a rotation about its vertical axis (the z-axis or the yaw-axis). Based on the assumption that most airplanes are designed to be symmetrical about the x-z-plane, this rotation makes it un-symmetrical with respect to the airflow, which inevitably generates a side-force and a moment about the yaw axis.

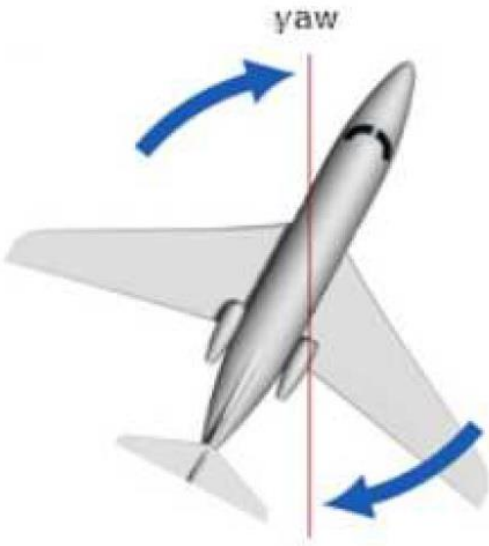

Figure 6: Yaw.

1.2 The problem of control

The yaw equilibrium is mainly kept by the vertical tail plane, with the deflection of its mobile part, the rudder. The deflection of the rudder is assumed positive if the trailing edge is rotated to the left, as shown in Figure 7. This situation produces a lateral force to the right that gives a negative yawing moment. Therefore

$$C_{N_{\delta_r}} < 0 \tag{1.3}$$

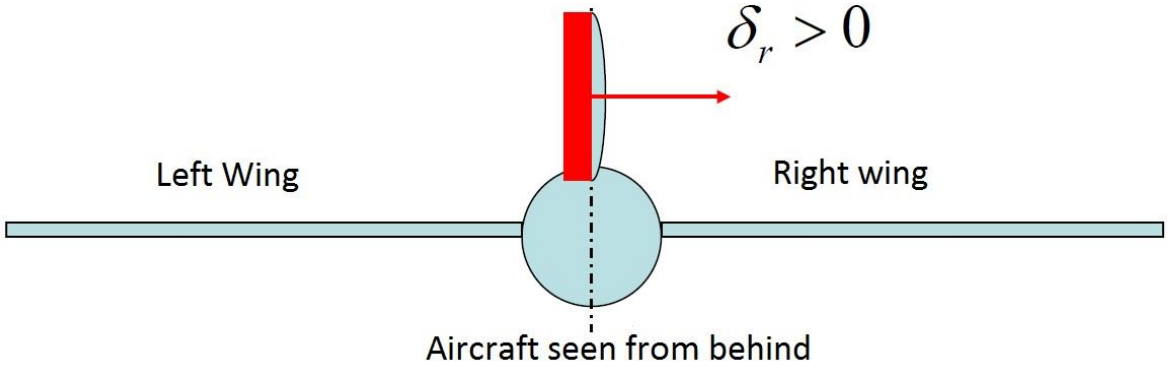

Figure 7: Positive rudder deflection.

The introduction of the rudder is needed to make the aircraft directionally controllable, making it capable of countering sideslip angles β of a certain magnitude. Therefore a close link between β and δ_r do exists; this relationship is linear at low angles of sideslip and rudder deflection.

If the yawing moment provided by $\beta > 0$ is given by

$$N = -L_V \cdot l_v \tag{1.4}$$

(Which is negative because $\beta > 0$ produces L_V to the left, which causes N, the yawing moment, to be in clockwise sense), the coefficient C_N is given by

$$C_N = \frac{N}{q\, S_W b} = -\frac{C_{L_V}\, S_V\, l_V q_V}{q\, S_W b} = -C_{L_V}\, \overline{V_V} \eta_V \tag{1.5}$$

where η_V represents the ratio between the dynamic pressure measured near the vertical tail plane (q_V) and the reference dynamic pressure (q), C_{L_V} represents the lift coefficient of the vertical tail plane and $\overline{V_V} = \frac{S_V l_V}{S_W b}$ represents the volumetric coefficient of the vertical tail plane, which is an important design parameter (already discussed in section 1.1.1).

In equation (1.4), C_{L_V}can be expressed as $C_{L_V} = a_V(\alpha_V + \tau_V \delta_r)$, in which only the contribution of the rudder is desired, i.e. $C_{L_V} = a_V \tau_V \delta_r$. It is therefore possible to obtain

$$C_N = -a_V \overline{V_V} \eta_V \tau_V \delta_r \qquad (1.6)$$

and then

$$C_{N_{\delta_r}} = -a_V \overline{V_V} \eta_V \tau_V \qquad (1.7)$$

which is the *rudder's control power*, similar to the elevator's control power, also negative. In the design phase the numerical value for this control derivative is assumable equal to $C_{N_{\delta_r}} \cong -0.001$. As the average value of C_{N_β}(stability derivative) is about $C_{N_\beta} \cong 0.001$, it follows that 1 degree of rudder deflection δ_r is necessary to obtain directional equilibrium (control) for 1 degree of sideslip angle β. If the directional stability decreases (less C_{N_β}), then the balanceable sideslip angles β increases, because for each degree of deflection δ_r corresponds less than one degree of β. So it is easy to understand why a less stable aircraft means a more controllable aircraft [4].

However, since there are limitations to the feasible deflection δ_r, there will be a maximum value of equilibrable β, which should not be too low. The typical maximum rudder deflections are between 25 and 30 degrees, but non-linear effects on the control derivative begin from δ_r equal to 15 degrees, which lead to the decrease of the rudder efficacy τ_V (small decrease up to 20 degrees and

larger after). Therefore, in the initial phase of the aircraft design it is often assumed a maximum deflection of 25 degrees.

The efficiency τ_V depends certainly from the chords ratio $\frac{c_r}{c_V}$ (where c_r is the rudder chord and c_V is the mean aerodynamic chord of the vertical tail plane's profile), which usually is not constant over the rudder and changes along the span, up to 0.7 in horn balanced configurations. The average value is thus higher, as it can be easily seen in Figure 8.

It is possible to better understand how the effectiveness τ_V changes with the chords ratio and with the rudder deflection from an analysis of the three-dimensional flow on the vertical plane (given the small aspect ratios, the field is strongly three-dimensional and the two-dimensional results have certainly to be correct). From the results of such analysis it may also be searched any other dependency of this parameter from the planform geometric parameters, such as the taper ratio, the sweep angle at the leading edge or the extension of the rudder along the span.

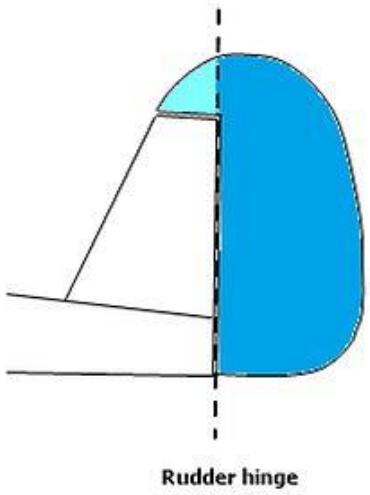

Figure 8: Rudder with horn balance.

The tasks which the rudder must fulfill, which also mark the most critical conditions which size the vertical plane, are the following:

1. Counteract the adverse yaw due to the deflection of the ailerons or roll rate
2. Counteract the slipstream rotation (configurations with frontal propeller engines)
3. Recovery from spin
4. Ensure equilibrium in case of engine failure at the minimum control velocity V_{MC}
5. Control the aircraft in stall condition[1]
6. Ensure the equilibrium in landing in crosswind conditions (high values of sideslip angle β)

Among all the stated conditions, the fourth and the sixth are the most critical from the point of view of the rudder deflections required, thus they often represent the sizing conditions. Observing the expression of $C_{N_{\delta_r}}$ in equation (1.7), it is possible to see how the τ_V parameter plays a primary importance in the estimation of the control derivative. For this reason, its correct evaluation is of fundamental importance and the present thesis work is concerned specifically with the aerodynamic of directional control effectiveness.

1.2.1 Engine Failure

During the take-off phase, if a failure occurs to one of the engines (see Figure 9), with a velocity V greater then V_1 (decision airspeed), on a multi-engine schematized as a twin-engine it is necessary that the rudder is able to balance the yawing moment produced by the operative engine. The take-off is assumed to be the most critical condition since, in addition to the low airspeed, the rudder control power is reduced, given the low value of the dynamic pressure (actually, as can be seen from equation (1.7), there is a reduction of the dynamic pressures ratio, η_V). The yawing moment provided by the operative engine is equal to

$$N = T \cdot l_T \qquad (1.8)$$

[1] The aircraft in stall conditions does not fall straight, but rolls and yaws, and to certify the stall speed is required a demonstration of the ability to control the aircraft.

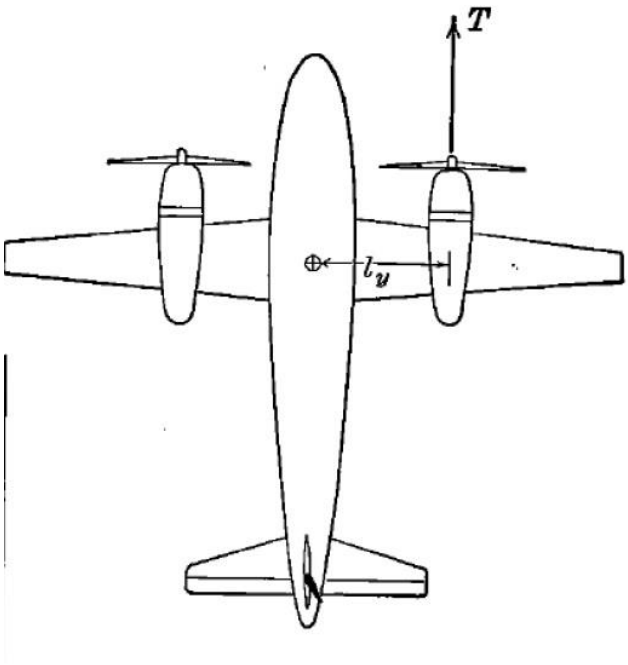

Figure 9: Engine Failure.

This moment must be balanced by the rudder, which has to provide a moment of yaw equal and opposite to the first. This moment is given by the product of the lateral force produced by the vertical plane for the distance of its aerodynamic center from the center of gravity

$$N = Y_V \cdot l_V \qquad (1.9)$$

The regulations state that such a maneuver can be performed with a maximum bank angle of 5 degrees (to compensate for the drift of the aircraft that arises because of the lateral force, see Figure 10). Moreover, typically a residual sideslip angle β of 5 degrees is accepted by regulations. This situation, however, is conservative, since with the presence of this residual sideslip an additional yawing moment (N) arises, due to the directional stability, which would help to control the aircraft in such conditions. Therefore, in order to consider the most conservative case, β is set equal to zero, considering the following equilibrium

$$C_N = C_{N_T} \cdot T + C_{N_{\delta_r}} \cdot \delta_r + C_{N_{\delta_a}} \cdot \delta_a \qquad (1.10)$$

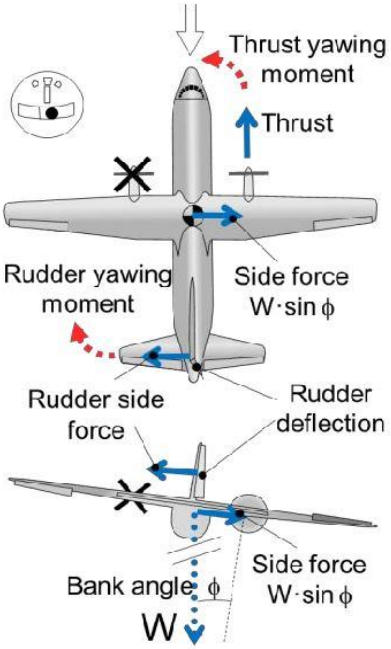

Figure 10: Roll during engine failure.

where δ_a is the deflection of the aileron, due to the bank angle, δ_r is the rudder deflection and T is the thrust provided by the operative engine. In order to find the minimum control speed, which is the minimum velocity at which it is possible to control the airplane in the event of an engine failure (this velocity varies with the engine type), it is necessary to analyze the C_{N_T}, i.e. the derivative of the $C_N$with respect to T. In particular, for a propeller-driven aircraft it can be shown that $C_{N_T} \propto \frac{1}{V^3}$, while for an aircraft with a turbofan engine it can be shown that $C_{N_T} \propto \frac{1}{V}$. In the previously given equation, neglecting the coupling between the lateral-directional motions (and therefore placing δ_a = 0) and placing $\delta_r = \delta_{r_{max}}$ (from which its moment is $N = Y_{max} \cdot l_v$), it is possible to find the intersection between the two remaining contributions, which provides the minimum control speed, V_{MC} (as it can be seen from Figure 11).

The same reasoning can be made in terms of dimensional moment N, where the moment due to asymmetrical thrust, N_T, is a function of the engine type and depends on the airspeed, while the moment due to the rudder increases with the square of the airspeed (see Figure 12). The

requirement imposed by the regulations is that V_{MC} must be less than 1.13 $V_{s_{TO}}$ (which is the stall velocity in take-off conditions). Therefore, if the minimum control speed is greater than this value, it is necessary to act in the preliminary design phase to suitably size the vertical tail plane.

The expression of the total C_N due to the rudder deflection is the following

$$C_N = -a_V \tau_V \eta_V \overline{V_V} \delta_r \qquad (1.11)$$

from which, since $\overline{V_V} = \frac{S_V \cdot l_V}{S \cdot b}$, it is possible to notice that increasing the vertical plane's surface S_V drives up the C_N (due to rudder deflection) curve, which is independent from airspeed, obtaining intersection with the other C_N curve (due to the engine type) to a lower speed, thus giving a lower V_{MC} (as shown in Figure 11).

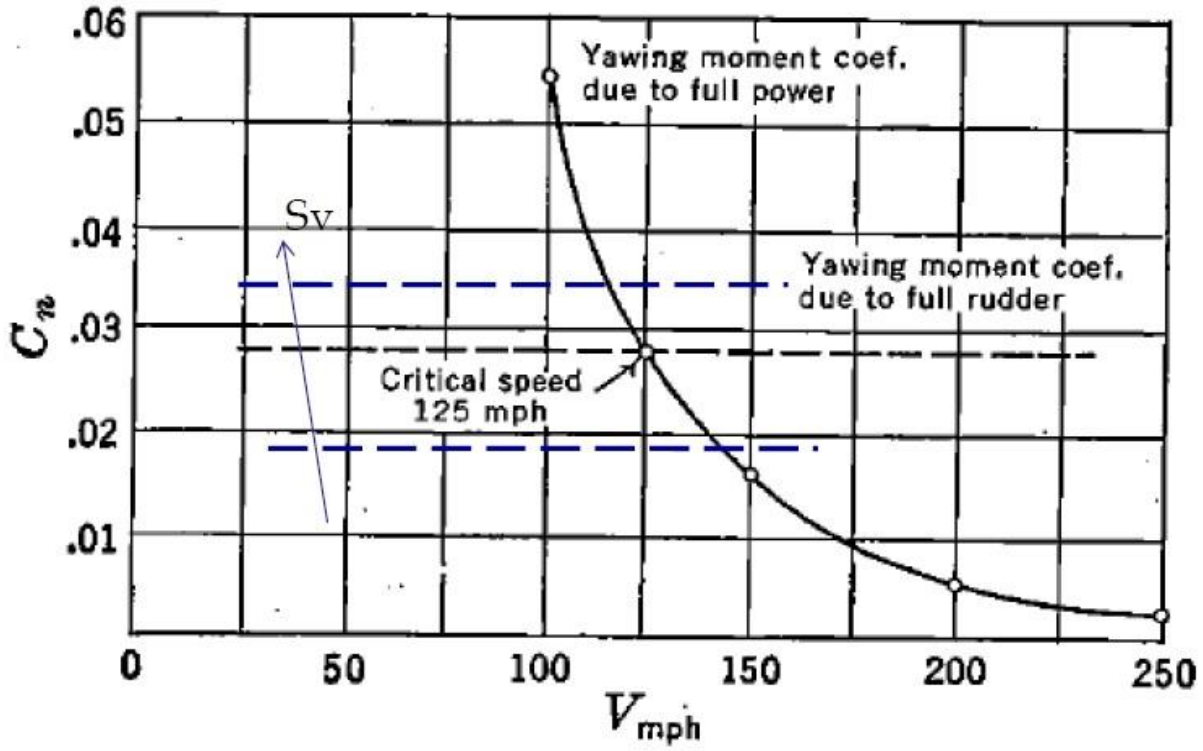

Figure 11: Critical speed from C_N vs V chart.

On the dimensional moment graph, given the expression of N

$$N = -\, a_V \tau_V \eta_V V_V \delta_r \, \frac{1}{2} \, \rho \, V^2 S \, b \qquad (1.12)$$

it is possible to note that with the increase of the vertical tail plane's surface the term proportional to V^2 gets even bigger, increasing the slope of the parabola that is representative of the moment due to the deflection of the rudder, obtaining intersection with the curve due to the engine type to V_{MC} gradually smaller.

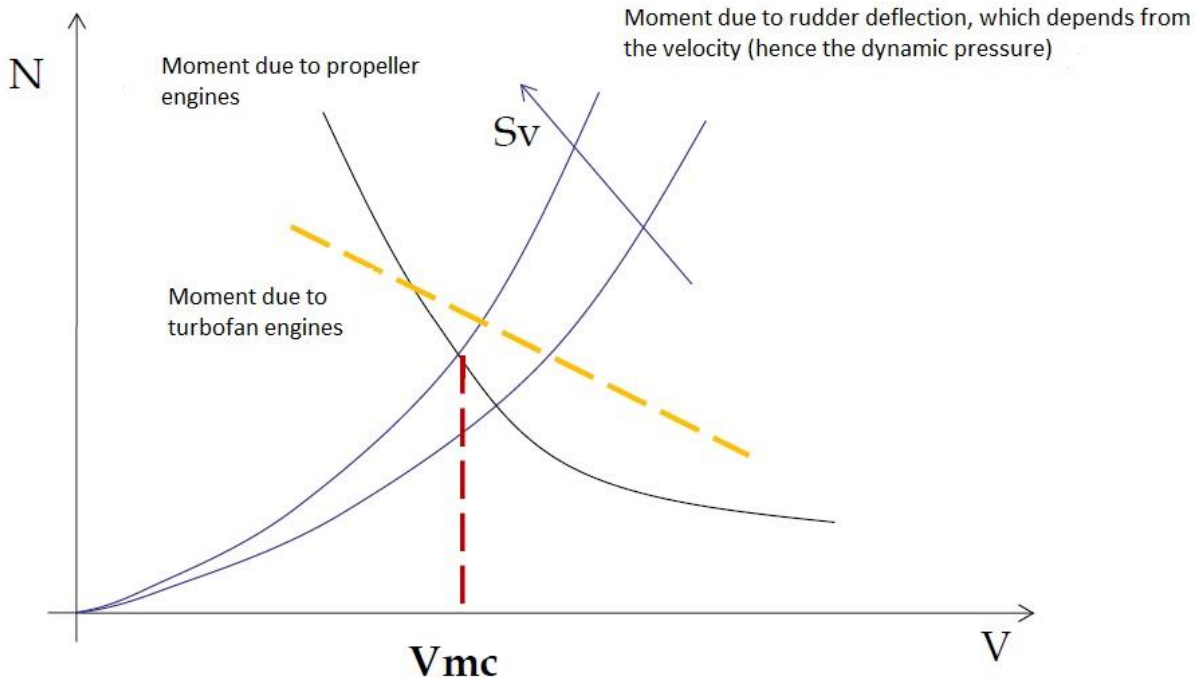

Figure 12: Critical Speed from N vs V chart.

Instead of increasing the surface of the vertical tail plane S_V, it is possible to operate on the effectiveness τ_V managing the chords ratio $\frac{c_r}{c_V}$, which it is possible to make variable along the span, increasing this ratio near the tip (with horn balance configurations, for example). In this way the effect is the same (actually slightly less) of the increase in S_V.

Having a bigger vertical tail plane (increasing S_V) has its considerable disadvantages, including increased costs and, above all, weight, which in turn affects the gravity center position and the longitudinal static stability margin. In addition, a larger vertical tail plane surface gives greater wetted area, S_{wet}. This implies an increase of the parasite drag resulting in reduced maximum airspeed. Therefore, the sizing of the vertical tail plane should be accordingly optimized.

During the wing design, assuming wing-mounted engines, it might be thought that placing the engines in the outer span positions reduces the bending moment (due to the lift) on the wing, thus allowing a lighter construction. However, this configuration is disadvantageous in case of engine failure, because it requires a greater vertical tail to balance the yawing moment due to asymmetric thrust, pushing the tail design to the above-mentioned critical issues.

Finally, it is interesting to note that, for propeller aircraft, the V_{MC} obtained from flight tests are different depending on the engine that goes into failure; the two propellers have in fact the same sense of rotation (co-rotating propellers) and produce different effects on the vertical tail plane, because of their different positions. In this case from the flight test is assessed which of the two is the critical engine (which is responsible for a greater V_{MC}), and in the preliminary design phase only that engine is analyzed.

1.2.2 Landing in headwind condition

It may happen that during the landing the aircraft will encounter strong winds (see Figure 13), which force the aircraft to fly at high angles of sideslip, β; it is therefore necessary that the rudder is able to balance the yawing moment that such currents would cause, in order to maintain the desired flight path. The equilibrium equation in this flight condition is (neglecting the contribution due to the aileron deflection, which is called "crossover effect", and propulsive effects)

$$C_N = C_{N_\beta} \cdot \beta + C_{N_{\delta_r}} \cdot \delta_r = 0 \qquad (1.13)$$

from this equation, the maximum sideslip angle β_{max} that can be balanced with the maximum rudder deflection $\delta_{r_{max}}$ (about 25 degrees) has to be derived, taking into account also the non-linear effects on the stability derivative C_{N_β} and on the control derivative $C_{N_{\delta_r}}$.

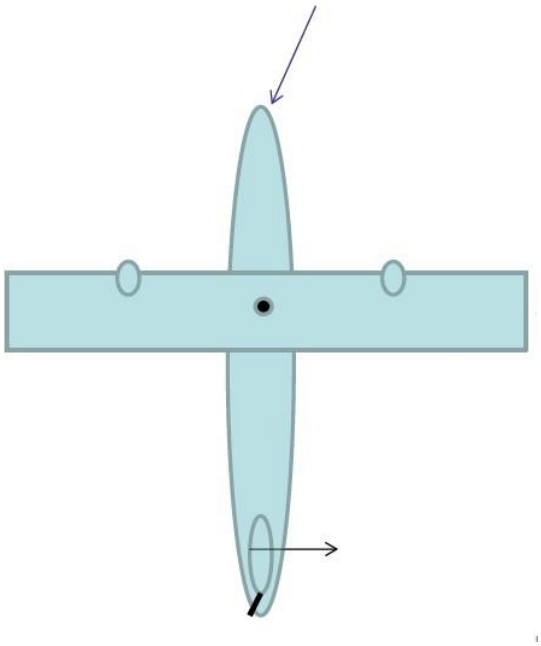

Figure 13: Landing in Headwind conditions.

The non-linear effects on the C_{N_β} are due to the non-linear behavior of the fuselage and to the stall of the vertical plane at high angles of sideslip. The non-linear effects on $C_{N_{\delta_r}}$ are due to the reduction of effectiveness at high rudder's deflection angles.

Looking at the C_{N_β} curve in Figure 14, it is possible to note the presence of a zone in which the vertical plane's lift increases, often due to the presence of a dorsal fin (shown in Figure 15), which is a small delta wing with low aspect ratio mounted to the base of the vertical tail plane. Because of the adherent vortex system along the leading edge (Jones Theory, see [10]), this small fin causes a vortex lift that not only raises the slope of the lift curve, but also considerably delays the stall (with the dorsal fin, the non-linearity in the C_{N_β} curve can be extended up to 35 degrees, as shown by CFD analyses presented in [26] and [13]). The high vorticity does reduce the β incidence at which the upper part of the vertical tail plane works, reducing the flow separation, acting as a turbolator.

The slopes of the two curves (the blue and the purple ones) in Figure 14 should be more or less equal to have a great overall behavior. It is also important to note that the curve of the $C_{N_{\delta_r}}$ decreases at high values of δ_r, because of the reduction in effectiveness previously underlined.

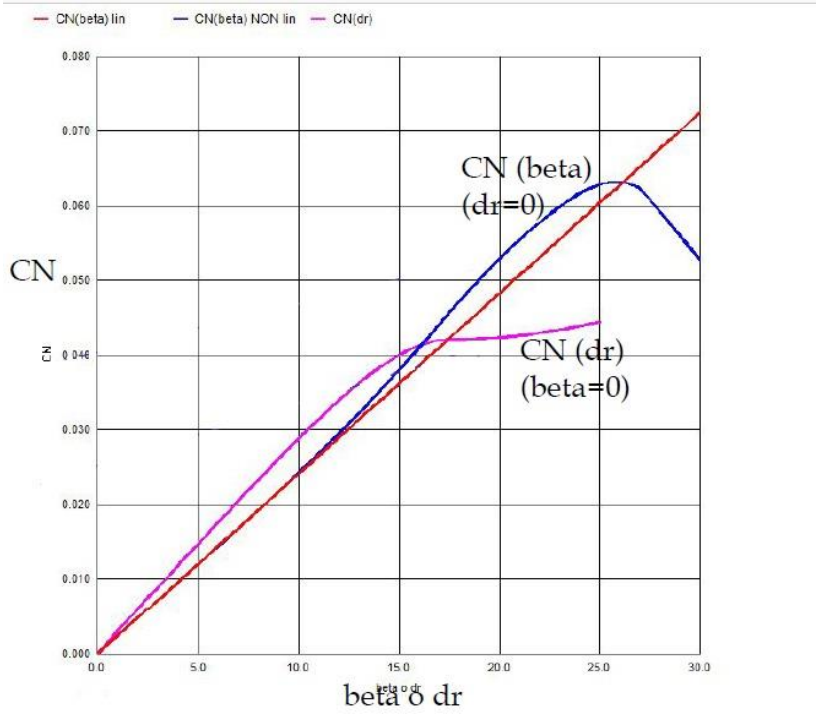

Figure 14: C_{N_β} and $C_{N_{\delta_r}}$ curves as function of β or δ_r.

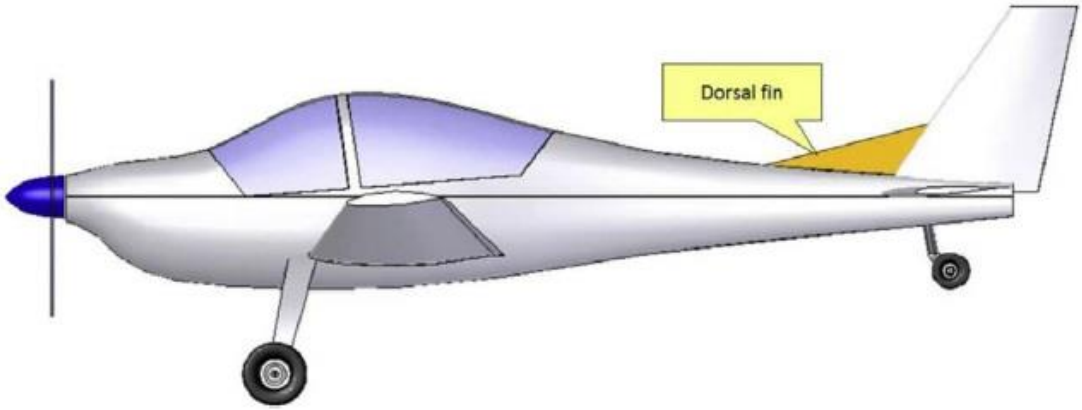

Figure 15: Dorsal fin example.

A too high value of C_{N_β}, which results in a high aircraft stability, implies that even with the rudder at its maximum deflection ($\delta_{r_{max}}$) the yawing moment due to a sideslip angle β cannot be balanced, while with very high values of $C_{N_{\delta_r}}$, directional control of the aircraft becomes too sensitive. In

conclusion, during the preliminary design of the vertical tail plane, it must be checked that the maximum value of β that is possible to balance is not less than 16-18 degrees (see Figure 16), with maximum deflection of the rudder. (In the initial part of Figure 16, the slope of the curves is such that for every degree of rudder's deflection, it is balanced one degree of sideslip). From Figure 16 and other considerations it is then clear that a more controllable aircraft is less stable and vice versa.

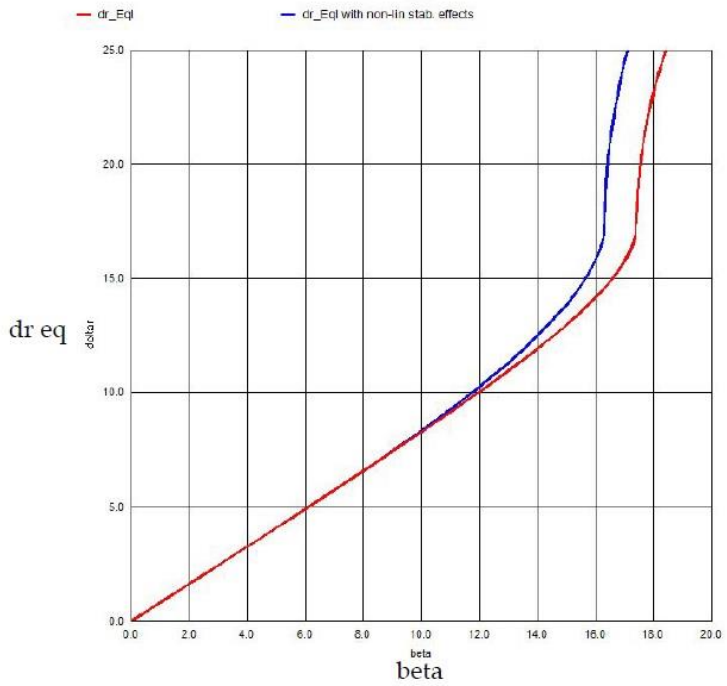

Figure 16: β trend as a function of δ_r.

1.2.3 Rudder lock and dorsal fin as its solution

A dorsal fin is a small surface extension installed at the leading edge of the root of the vertical tail (as shown in Figure 15).

Its purpose is to add directional stability to the aircraft and that way prevent a serious condition known as rudder-lock. The dorsal fin, or dorsal as it is often referred to, can be as simple as a thin flat plate or as complicated as a curved compound surface stamped aluminum fairing riveted to an existing fin. In any case, its presence causes the leading edge to feature a discontinuity and this is imperative to its functionality.

To study the problem of rudder lock it is necessary first to define the concepts of balance rudder deflection ($\delta_{r,eq}$) and floating rudder deflection ($\delta_{r,float}$), both shown in Figure 17:

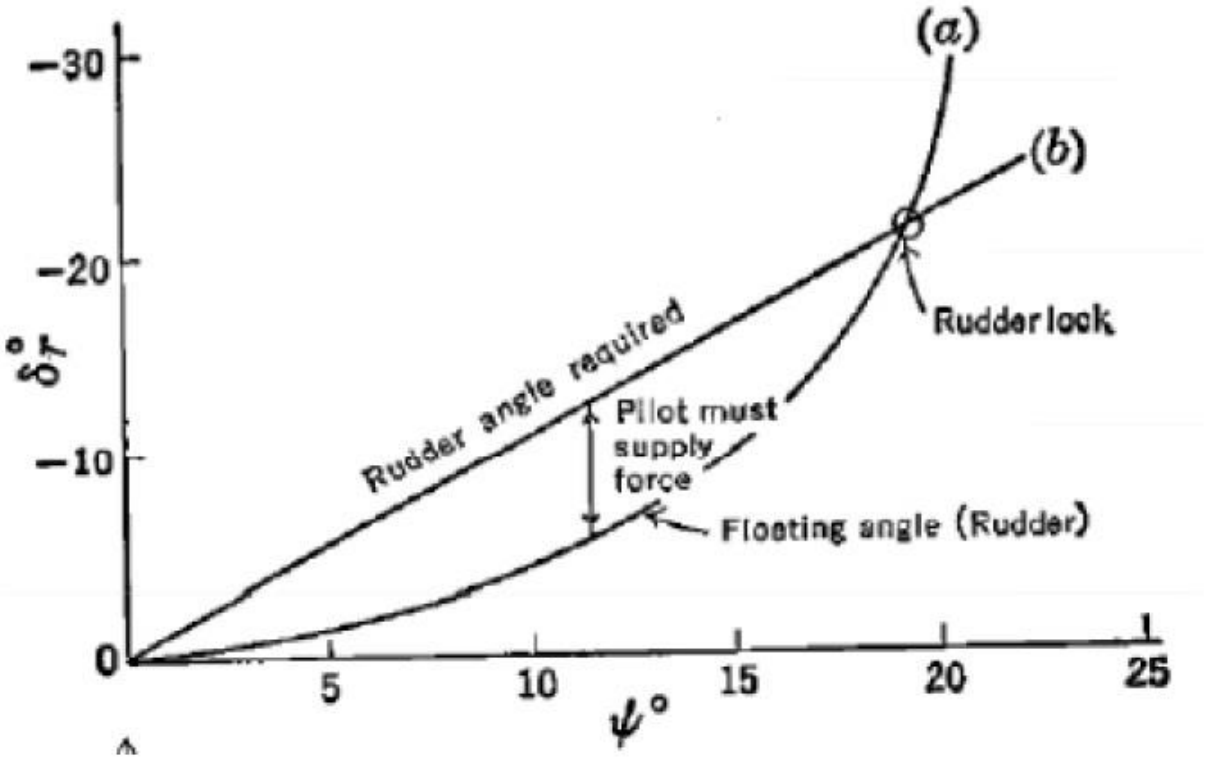

Figure 17: Rudder deflection δr,eq and δr,float [4].

- $\delta_{r,eq}$: it is the deflection which must have the rudder to ensure the balance, so to ensure that the value of the sideslip angle is maintained constant instant by instant. If this deflection is not realized, the inherent stability related to the vertical, lead the nose in the direction flow canceling the sideslip. Increasing the requested sideslip angle such request deflection increases almost linearly.
- $\delta_{r,float}$: it represents the deflection that occurs automatically in free controls for a given value of the sideslip angle, related to aerodynamic phenomena that characterizes the directional control. By increasing the sideslip angle, such deflection increases in a non-linear way.

For every value of the sideslip angle, the pilot must carry an effort that allows to compensate for the gap in δ_r from $\delta_{r,float}$ to $\delta_{r,eq}$. For each value of β this gap is different, as well as the force exerted by the pilot that can be identified in Figure 17.

The phenomenon of rudder lock is largely caused by insufficient directional stability of the airplane at high angles of yaw (AOYs). As the airplane is yawed to a high AOY (for instance in a side-slip maneuver) two things may happen:

1) Case of tail designed with very high aspect ratio (AR)

In this case are achieved very low values of the stall angle, as it can be seen from the chart of lift curves as a function of the aspect ratio AR in Figure 18.

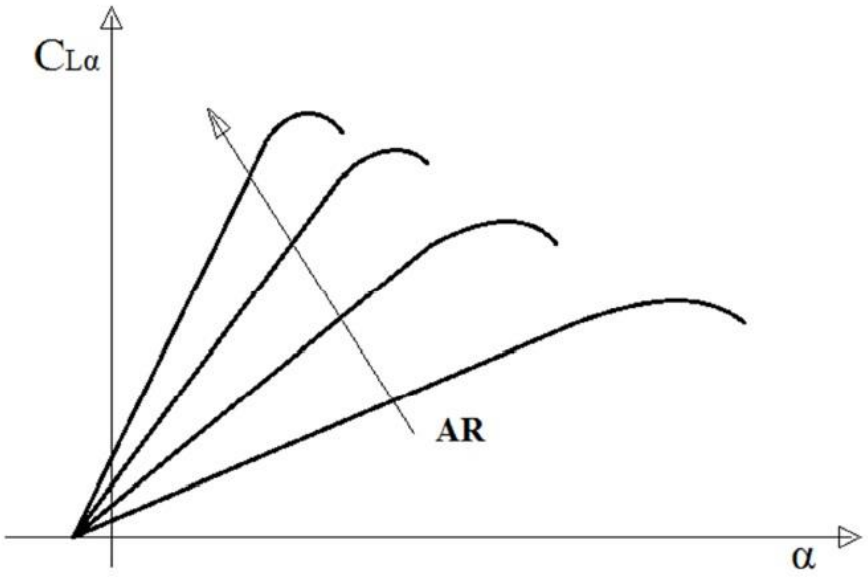

Figure 18: Lift curve as a function of aspect ratio (AR).

When the angle increases approaching the stall condition, a strong reduction of the C_Y and C_N is obtained and the vertical reduces its contribution to stability. This implies a greater ease for the aircraft to change its direction. In particular, the stabilizing moment generated by the tail that has been reduced can become smaller than the destabilizing moment generated by the fuselage.

2) Case of tail designed with very low aspect ratio (AR)

The side loading resulting from the sideslip will tend to force the rudder to the leeward side. This is due to depression that is realized on the leeward side, which is in steady state conditions as stronger as greater is the rudder deflection. As before, by increasing the angle of sideslip, the vertical plane stalls and reduces its contribution to directional stability. In this case, however, to understand the phenomenon of rudder locking, it is important to show the gradients of the pedal force (see Figure 19).

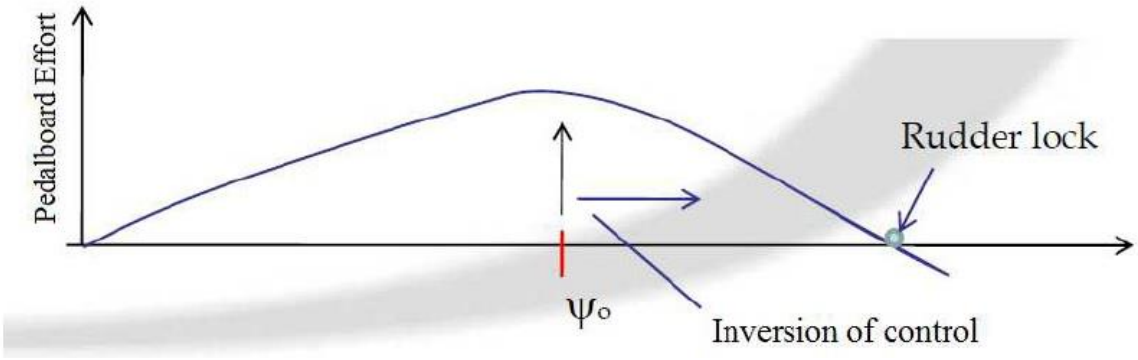

Figure 19: Pedalboard effort as a function of sideslip angle β.

In fact, it is possible to identify a β value for which the $\delta_{r,eq}$ is equals to $\delta_{r,float}$, condition for which the pedal force is null. Intuitively, if the force exerted by the pilot is constant, when the required force tends to zero, it appears that the pilot will push the pedal to the end stop. Any effort to achieve a deflection of the rudder in the opposite direction requires a strong pedal force due to the strong hinge moments generated. If the pilot fails to counteract these moments, the rudder will remain locked.

A solution for the rudder lock condition is to mount a fin on the dorsal [9]. This will partition the vertical into two low-aspect-ratio segments. The smaller one will keep the flow attached to an even higher sideslip angle and this helps maintain sufficient directional stability. Details can be found in Ref. [58].

1.3 Methodology evolution for the study of lateral-directional stability

From the ’30s to the ’50s, in the USA, the National Advisory Committee for Aeronautics (NACA) provided some results on the directional stability on isolated vertical tailplanes, partial and complete aircraft configurations through many hours of wind tunnel tests, results that were summed up in a method of analysis completely reported and described in the USAF DATCOM [11].

From the ’50s to the ’90s in the USA researches were concentrated mainly on high subsonic and supersonic flow field and until the ’70s only wind tunnel tests could fit for the objective. Usually the directional stability of the models tested deteriorated with increasing angle of attack and increasing Mach number. Interference effects had a strong influence upon the vertical-tail effectiveness and, consequently, upon the directional stability. These effects are, for the most part, associated with complex flow involving vorticity or shock waves and therefore were difficult to analyze at that time.

In the ’70s first computer programs began to appear on the scene, with the application of panel methods, and, then, the birth of Computational Fluid Dynamics (CFD). More information on this specific issue are given in the Chapter 3.

Most recent panel codes are used to determine the stability and control derivatives of new aircraft configurations early in the design process, since these parameters are important also to most control law design methods and their early estimate may permit significant improvement in configuration weight, cost, performance and even stealth, through multidisciplinary design.

These panel methods are part of the Computational Fluid Dynamics (CFD), though the approach with the Prandtl-Glauert equation has little physics inside. The Prandtl-Glauert equation model involves only a scalar potential and the free stream Mach number. It’s just the wave equation in a steady compressible flow regime.

Among the different fluid dynamic models which may be employed for the solution of the motion fields that are carried out around geometries of aeronautical interest are the Navier-Stokes equations. Because of the equations complexity that are of mixed hyperbolic-parabolic kind, mediated forms are often used. In this thesis, the term CFD is used to indicate the Reynolds Averaged Navier-Stokes equations (RANS).

Through CFD simulations the aerodynamic characteristics of interest can be investigated. Panels method are not ideal for determining the effects of aerodynamic interference or to simulate the gap of control surfaces, since they solve the flow field by summing the results of distributed aerodynamic singularities. It has been shown by [12] that the aerodynamic interference effects can be caught with RANS calculations. In fact, recent (last 15 years) CFD methods makes use of finite differences, Finite Element Method (FEM) and finite volume methods.

Any further step in stability and control analysis techniques saw a return to the study of the low subsonic flow field.

An example of a discretization in panels of an aircraft geometry can be seen in Figure 20.

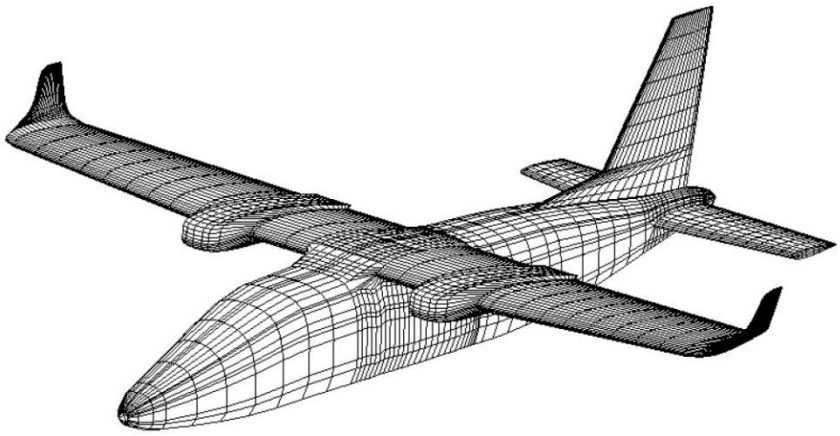

Figure 20: The Tecnam P2012 discretized in panels, taken from the work of Nicolosi, Della Vecchia and Corcione [14].

CFD tools offer significant benefits as a support to the experimental methods to predict aerodynamic parameters [13]. In fact, the wind tunnel is traditionally the primary tool to provide aerodynamic inputs for simulation data bases and to predict stability and control characteristics, but shortcomings exist in wind tunnel testing methods (for example operation at a lower than free flight Reynolds number causes large discrepancies on boundary layer separation in certain configurations) that can result in serious errors in the predicted stability and control characteristics. Moreover wind tunnel tests require both the construction of a model and an adequate test facility. Additionally, the lag time between the paper design and the wind tunnel results can be considerable. Furthermore, any configuration change requires a change of the test model. This greatly increases the cost of the product and the time to market.

On the other hand, the simple theory at the base of the USAF DATCOM or other semi-empirical method is only accurate for preliminary relationships between the overall aircraft geometry and stability.

CFD offers a more direct approach in finding stability coefficients, computing aerodynamic forces and moments by integration of surface pressures along the aircraft boundaries. In general, the most complicated geometry can be solved with the proper selection of a CFD method and right boundary conditions, so it is believed that CFD tools can completely cope with stability and control issues and complement the traditional wind tunnel data sources [13]. The decreasing costs and the increasing power of the computers makes the CFD more and more attractive.

1.4 State of art and new approach for the estimation of effectiveness

In the present state of the art, the evaluation of effectiveness in the preliminary design stage is carried out through the use of semi-empirical methods, such as those proposed in Torenbeek [6], McCormick [16] or Roskam [15] texts. These methods have the great advantage of being quickly applied and easy to understand, but at the same time involve great disadvantages:

- they do not take into account the influence of other wing geometric parameters (leading edge sweep, taper ratio ecc.) that are not the chords ratio $\frac{c_r}{c_V}$ or the deflection of the moveable part (rudder), δ_r.
- the non-linear effects are not taken into account in the correct way. These effects drastically reduce the effectiveness for deflections of rudder greater than 15 degrees;
- these methods come from semi-empirical analysis of obsolete geometries (airplanes of the '40s, mostly military aircrafts).

Discrepancies between these methods, along their obsolete geometries, made the choice to attempt a different approach through the CFD. For the purpose of the introduction, here it is stated that this new procedure, explained in Chapter 4, takes into account 38 different vertical plane configurations, performing CFD analyses in order to highlight the differences between the semi-empirical methods and numerical results.

This procedure is immediate to use, just looking at the analyses matrix presented in Chapter 4 without defining any other parameter, once chosen the vertical plane configuration and its main dimensions and its results are quite different to that provided by the semi-empirical methods. This new procedure, which led to the realization of a new method for the estimation of the effectiveness, was built upon lots of CFD analyses on a typical regional turboprop vertical plane. Experimental tests are to be conducted soon to further validate the method.

2 Semi-empirical Methods

This chapter deals with the effectiveness analysis of the vertical tail of a conventional airplane through semi-empirical methods, available in literature. It is valid for low speed (subsonic) in cruise configuration (low angle of attack, low angle of sideslip). One of the main objectives of this thesis is to compare the results obtained by these methods, which are easy to use and quickly applicable, with those obtained by CFD analyses, which offer results definitely more accurate, but with a much greater computational effort (it takes several days to get the numerical results, whereas it takes only minutes to get an estimation of the effectiveness through the semi-empirical methods). A comparison is therefore a must: similar results would push towards the implementation of such semi-empirical methods, which, at the cost of slightly lower accuracy, enable to save considerable amount of machine hours and man-hours. In contrast, large differences in results would push toward the use of numerical analyses, the results of which should be more accurate.

Methods involved here are proposed by Roskam [15], Torenbeek [6], and McCormick [16]. These methods exploit different basic assumptions to achieve an early estimation of effectiveness during the step of the vertical tail plane preliminary design, differing mainly by the number of wing geometric parameters taken into account.

2.1 Roskam Method

This method, proposed on the text written by J.Roskam [15], is certainly the most comprehensive in terms of wing geometric parameters taken into account, and is therefore the most accurate in the family of semi-empirical methods.

First of all, it is necessary to give the definition of positive rudder deflection, which is one resulting in a negative yawing moment (t.e. rudder to the left).

It is possible then to obtain the expressions that provide $C_{Y_{\delta_r}}$ and $C_{N_{\delta_r}}$, from which it will be possible to extract the term relative to the effectiveness of the mobile part.

The side-force due to rudder derivative, $C_{Y_{\delta_r}}$, may be computed from:

$$C_{Y_{\delta_r}} = \left(\frac{C_{L_{\alpha_V}}}{C_{l_{\alpha_V}}}\right)(k'\ K_b)\left(\frac{C_{l_\delta}}{C_{l_{\delta_{theory}}}}C_{l_{\delta_{theory}}}\right)\left(\frac{(\alpha_\delta)_{C_L}}{(\alpha_\delta)_{c_l}}\right)\frac{S_V}{S} \qquad (2.1)$$

where

- $C_{L_{\alpha_V}}$ is the vertical tail plane's lift-curve slope, found from

$$C_{L_{\alpha,w}} = \frac{2\pi A}{2 + [\frac{B^2A^2}{K^2}\left(1 + \frac{(\tan \Lambda_{\frac{c}{2}})^2}{B^2}\right) + 4\ ]^{\frac{1}{2}}} \qquad (2.2)$$

Which is the Helmbold-Diederich formula [17], with appropriate substitution of vertical tail parameters for wing parameters. In addition to the parameters to replace, in the above equation also appear the compressibility parameter $B = \sqrt{(1 - M^2)}$, the ratio of section lift-curve slope to theoretical thin-section value, $K = \frac{C_{l_\alpha}}{2\pi/B}$, which for thin airfoil ($C_{l_\alpha} \approx 2\pi$) it is equal to B, and the sweep angle at half chord, $\Lambda_{c/2}$. The vertical tail aspect ratio, $A_{V_{eff}}$, must be substituted for the wing aspect ratio, *A*. The effective aspect ratio of the vertical tail may be estimated from:

$$A_{V_{eff}} = \left(\frac{A_{V(f)}}{A_V}\right)A_v\ \left\{1 + \ K_{vh}\left[\left(\frac{A_{V(hf)}}{A_{V(f)}}\right) - 1\right]\right\} \qquad (2.3)$$

where

- b_V and S_V depend on the vertical tail configuration as shown in Figure 21 for a range of vertical tail configurations.

- $\left(\frac{A_{V(f)}}{A_V}\right)$ is the ratio of the vertical tail aspect ratio in the presence of the fuselage to that of an isolated vertical tail. This ratio can be determined from Figure 22.

- $\left(\frac{A_{V(hf)}}{A_{V(f)}}\right)$ is the ratio of the vertical tail aspect ratio in the presence of the horizontal tail and the fuselage to that in the presence of the fuselage alone. This ratio can be determined from Figure 23.

- K_{vh} is a factor which accounts for the relative size of the horizontal and the vertical tail, and it may be determined from Figure 24.

- $C_{l_{\alpha_V}}$ is the vertical tail plane airfoil lift-curve slope and it can be found from several formulas proposed in literature; in the present thesis work, since the vertical tail plane airfoil can be easily treated with the thin profile theory, will be set equal to 2π, in radians.
- k' is a correction factor which accounts for non-linearities at high flap/rudder deflections and is found from Figure 25.
- K_b is the flap-span factor as obtained from the procedure suggested in Figure 26 but with the data from Figure 27.
- $\frac{C_{l_\delta}}{C_{l_{\delta_{theory}}}}$ is found from Figure 28, in which δ_f is the flap (rudder) deflection in radians.
- $C_{l_{\delta_{theory}}}$ is found from Figure 29. It accounts for flap and for thickness ratio and it is expressed in radians.
- $\left(\frac{(\alpha_\delta)_{C_L}}{(\alpha_\delta)_{c_l}}\right)$ is the ratio of the three-dimensional flap effectiveness parameter to the two-dimensional flap-effectiveness parameter as found in Figure 30.
- S_V is the effective vertical tail area as defined in Figure 21.

The yawing-moment-due-to-rudder derivative, $C_{N_{\delta_r}}$ (also called *rudder control power*), may be estimated from:

$$C_{N_{\delta_r}} = -C_{Y_{\delta_r}}\left(\frac{l_V \cos\alpha + z_V \sin\alpha}{b}\right) \qquad (2.4)$$

where

- l_V and z_V are defined in Figure 31.
- $C_{Y_{\delta_r}}$ is given by equation (2.1).

Observing the expression of $C_{Y_{\delta_r}}$, which also appears in the expression of the rudder control power $C_{N_{\delta_r}}$, it is possible to find an expression for the parameter of interest, i.e. the effectiveness τ_V, given by

$$\tau_V = \left(\frac{1}{C_{l_{\alpha_V}}}\right)(k'\,K_b)\left(\frac{C_{l_\delta}}{C_{l_{\delta_{theory}}}}C_{l_{\delta_{theory}}}\right)\left(\frac{(\alpha_\delta)_{C_L}}{(\alpha_\delta)_{c_l}}\right) \qquad (2.5)$$

where the terms included are the same described in the previous pages. The effectiveness found by this method, observing the subsequent figures (from Figure 21 to Figure 31), takes into account the chords ratio, the rudder deflection and also important geometrical parameters such as the percentage thickness, the rudder extension along the span and the taper ratio. It is therefore easy to understand why it is considered one of the most accurate semi-empirical methods.

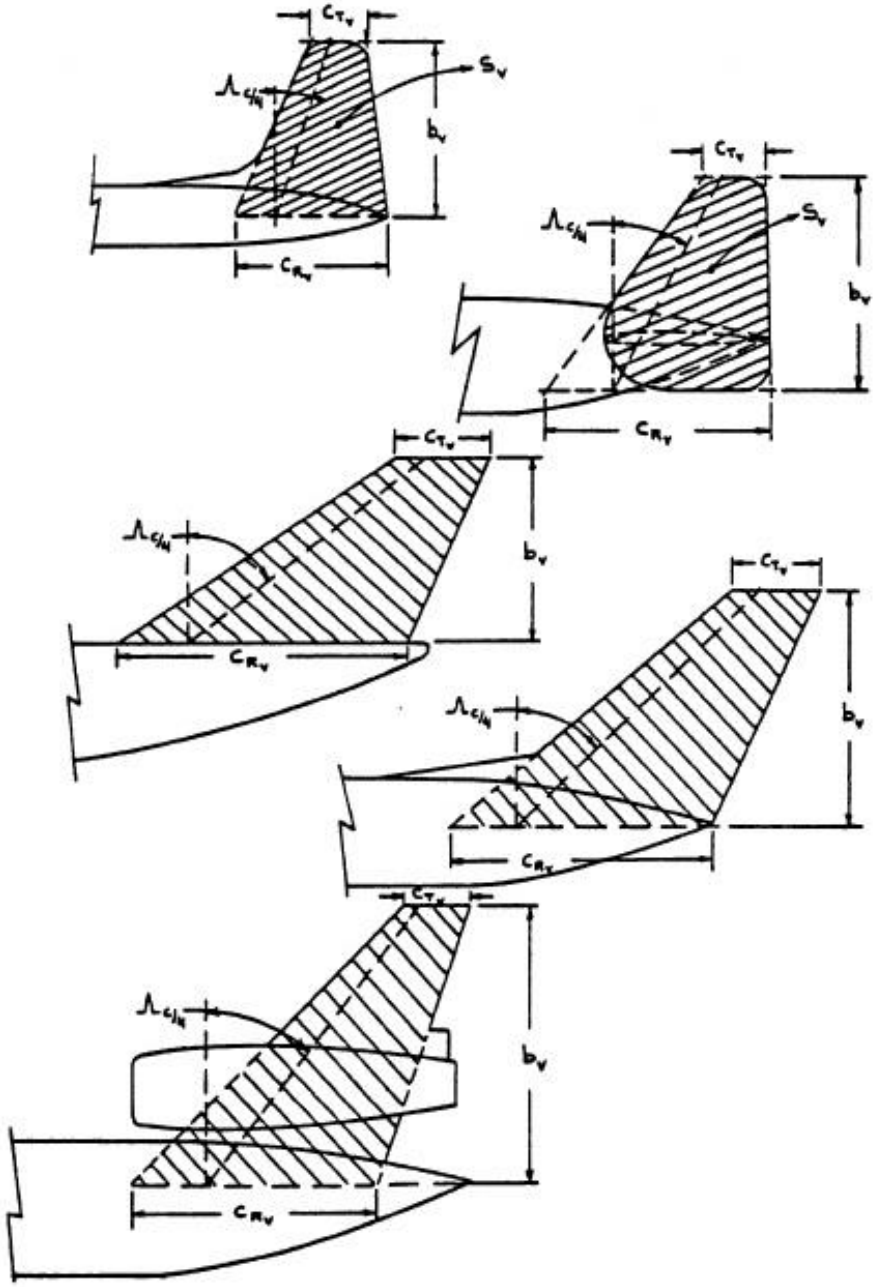

Figure 21: Examples of Effective Vertical Tail Geometries.

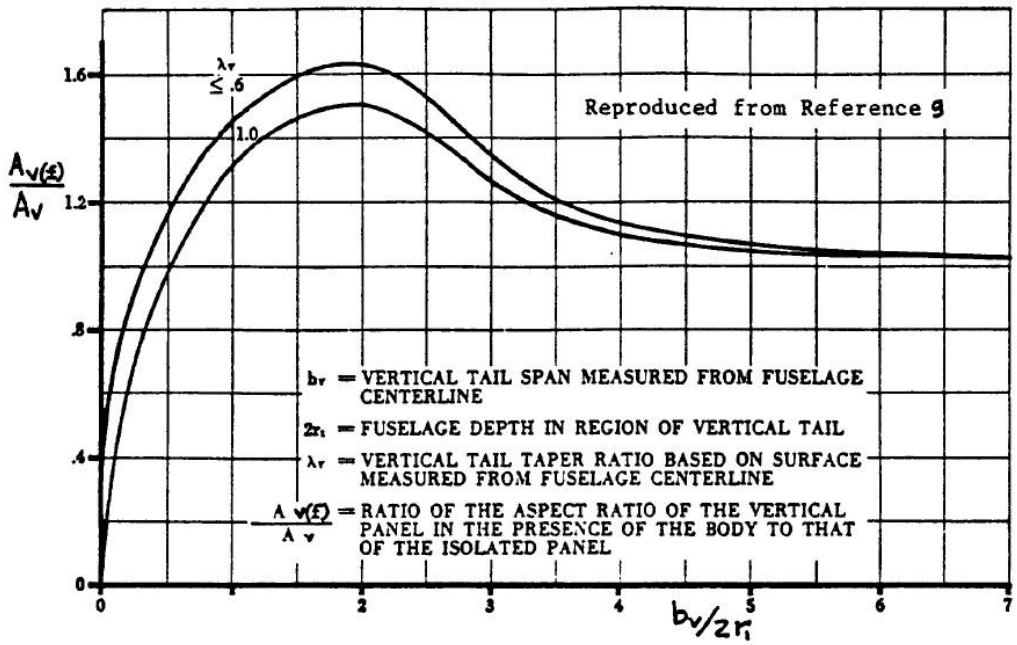

Figure 22: Ratio of vertical tail aspect ratio in presence of fuselage to that of isolated tail, found from [11].

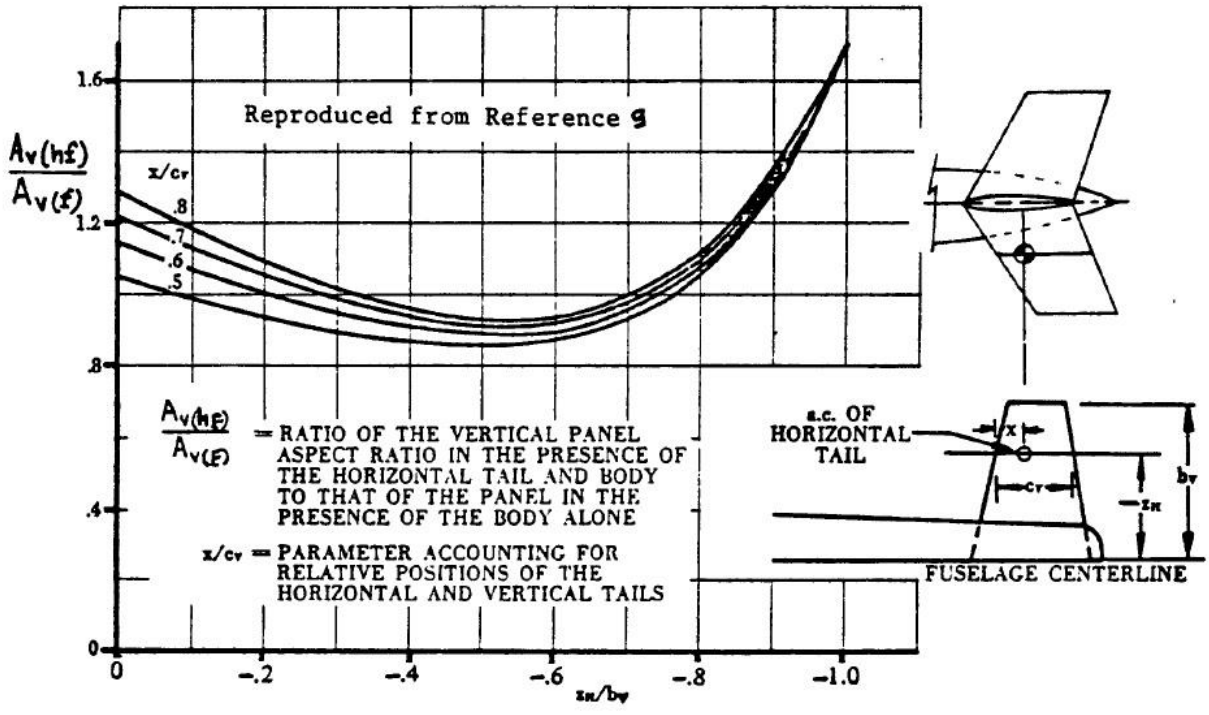

Figure 23: Ratio of vertical tail aspect ratio in presence of fuselage and horizontal tail to that in presence of fuselage alone, found from [11].

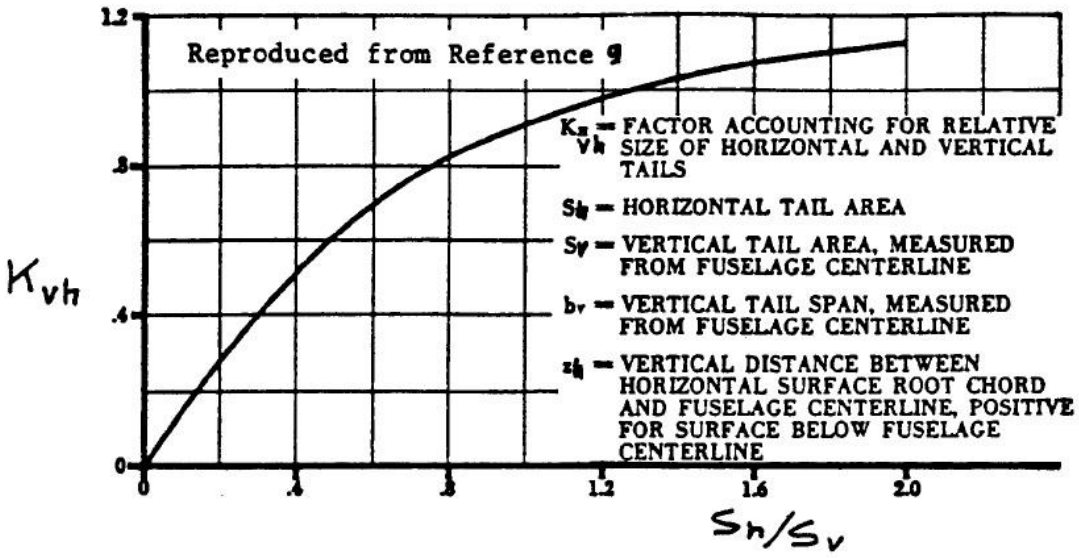

Figure 24: Factor which accounts for relative size of horizontal and vertical tail, found from [11].

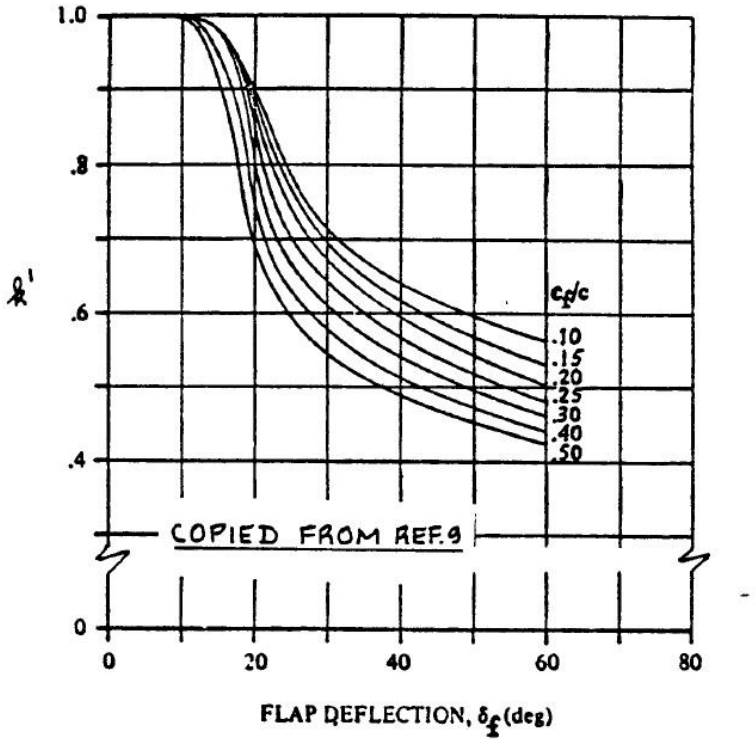

Figure 25: Correction factor for nonlinear lift behavior of plain flaps, found from [11].

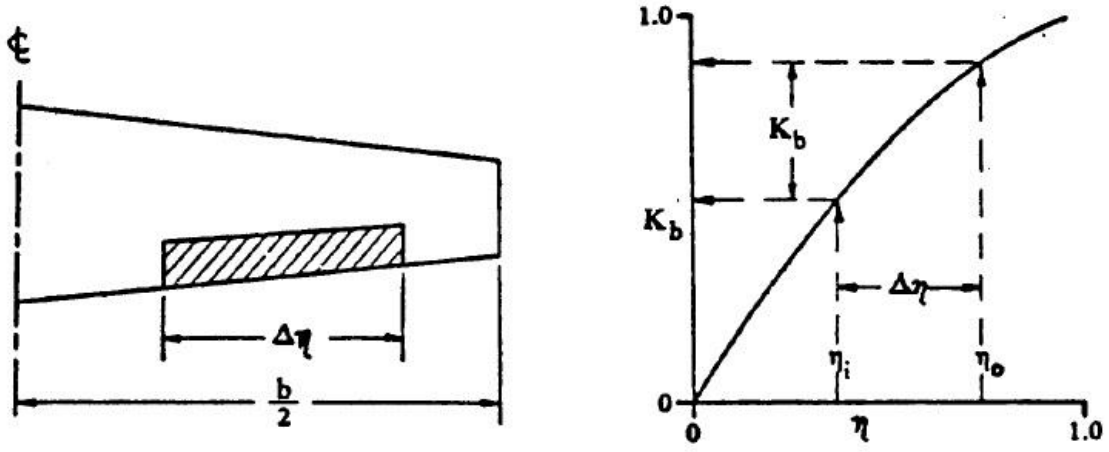

Figure 26: Procedure for estimating K_b.

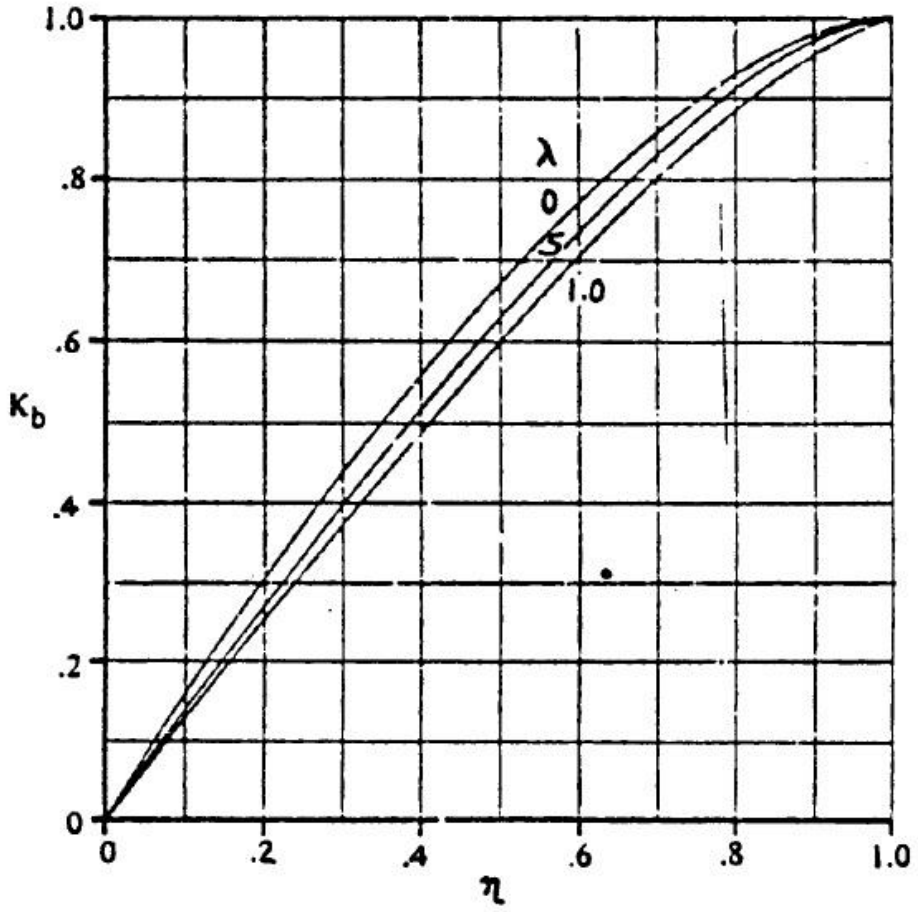

Figure 27: Effect of taper ratio and flap span on K_b.

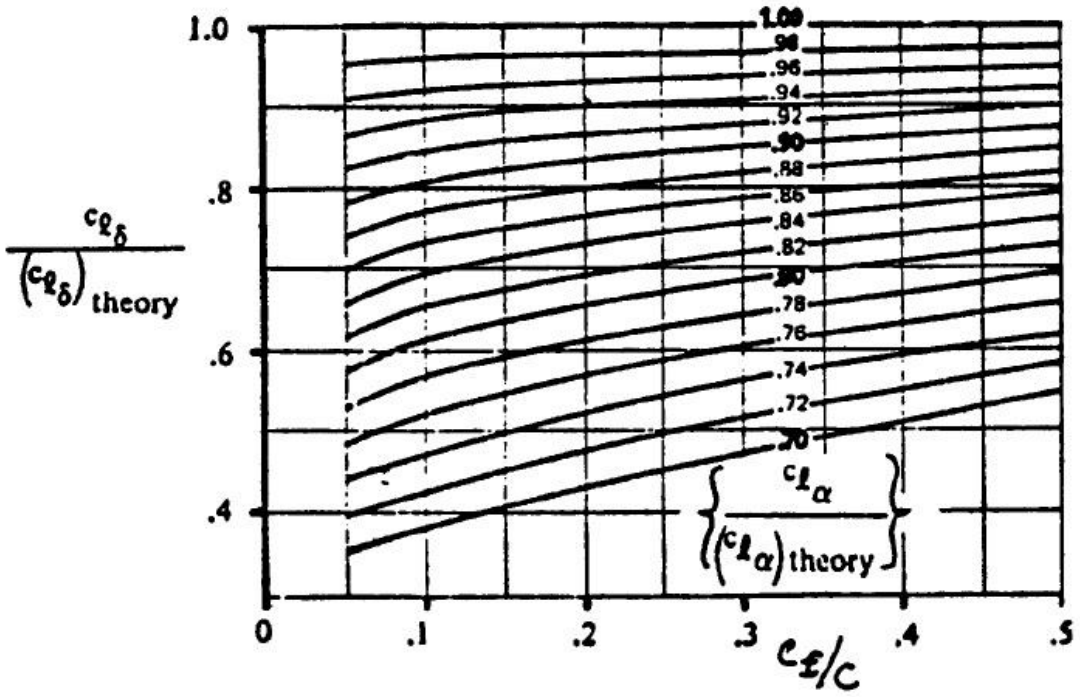

Figure 28: Correction factor for plain flap lift.

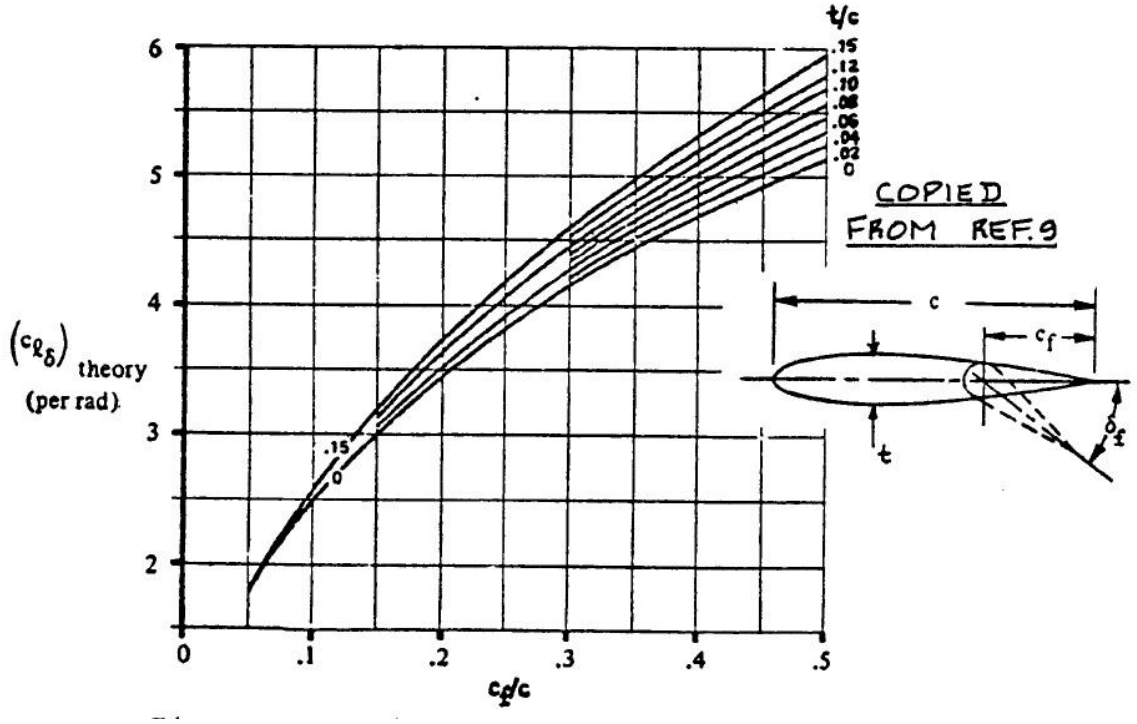

Figure 29: Lift effectiveness of a plain flap, found from [11].

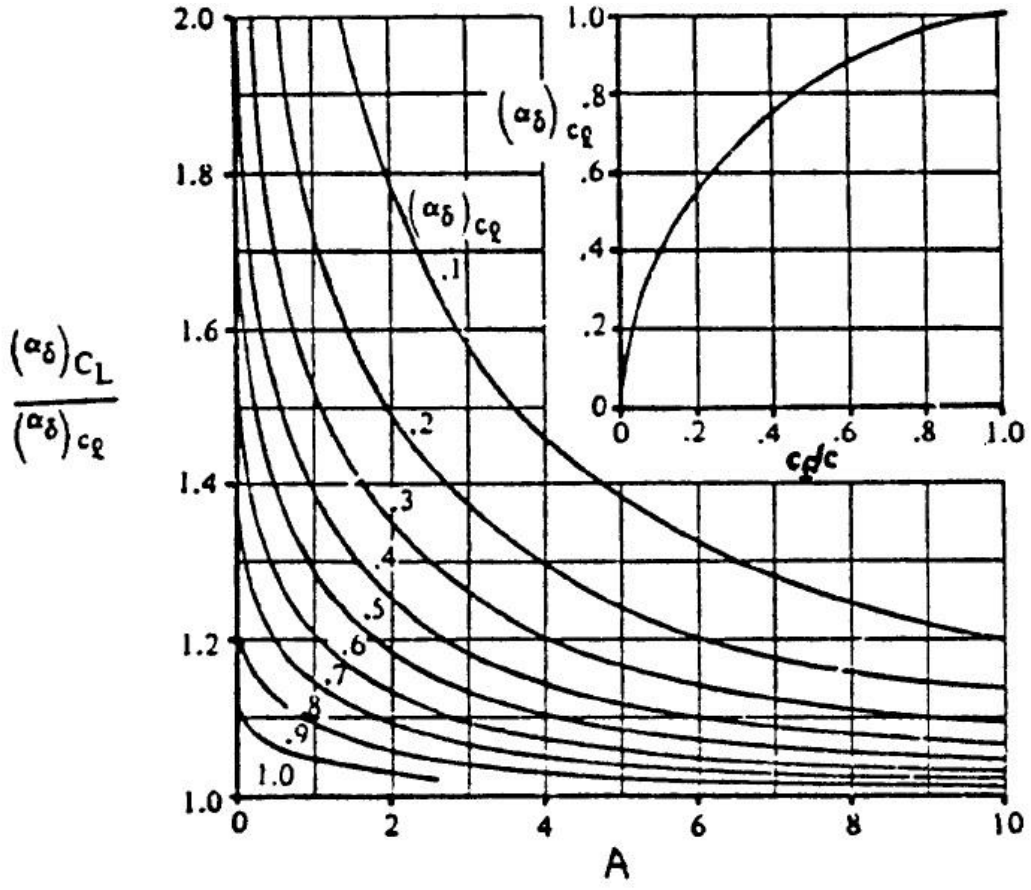

Figure 30: Effectiveness of aspect ratio (A) and flap chord ratio on the three-dimensional flap effectiveness.

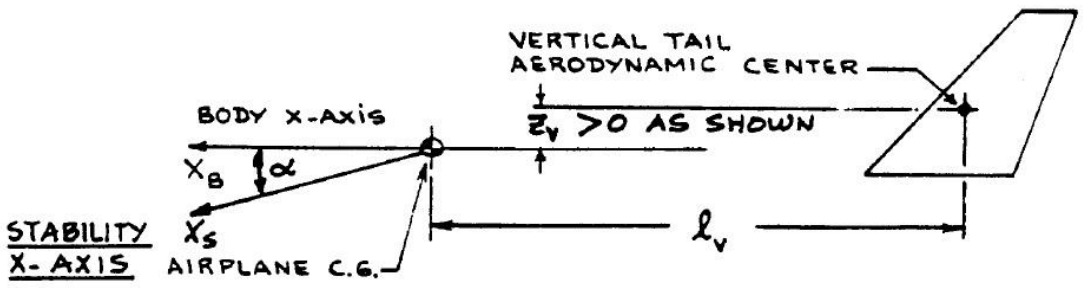

Figure 31: Geometry for Locating vertical tail(s).

2.2 Torenbeek Method

Methods proposed on Torenbeek text are a collection of generalized data for estimating the lift curve and drag polar in the configuration for low-speed flight. Passive trailing-edge and leading-edge high-lift devices are considered. Glauert's linear theory for thin airfoils with deflected flaps

forms the basis for most prediction methods; correction factors are given far taking nonlinearity and flow separation into account.

Recalling that the method proposed by Torenbeek takes into account generic control surfaces (generically called, from now on, "flaps"), it is necessary to remember that such considerations can be easily applied to all types of mobile surfaces, including the rudder of the vertical tail plane, which is the main subject of this thesis.

The effectiveness factor represents the ratio of experimental to theoretical lift increment. The traditional approach to the calculation of wing lift is based on the assumption that the lift generated by a two-dimensional wing (airfoil section) can be considered as a starting point. A suitable conversion to the three-dimensional wing is made by means of semi-empirical corrections for part span, fuselage effects, etc. This procedure is acceptable when spanwise flows and interference effects are or of minor importance or completely absent. It is therefore frequently used in the preliminary design stage of aircraft categories that are in present use in civil aviation, in the realization that during the configuration development an adequate aerodynamic development program will be initiated in order to optimize the wing and flap system.

Theoretical methods of calculating the aerodynamic characteristics of flapped sections have recently come to a stage of development where lift and pitching moment can be predicted with reasonable accuracy. A survey of the state of the art is given in [18]. Particularly for the most effective flap systems (multiple element flaps, slats), the flow is very sensitive to the details of the configuration: the flap and slat shape, their relative position, shroud shape, etc. This would require an optimization program which is a complex subject in itself. Instead of this, it is presented in this section a generalized semi-empirical method based on thin airfoil theory and experimental data.

The basic effect of trailing-edge flap deflection on the lift curve of an airfoil section is depicted in Figure 32.

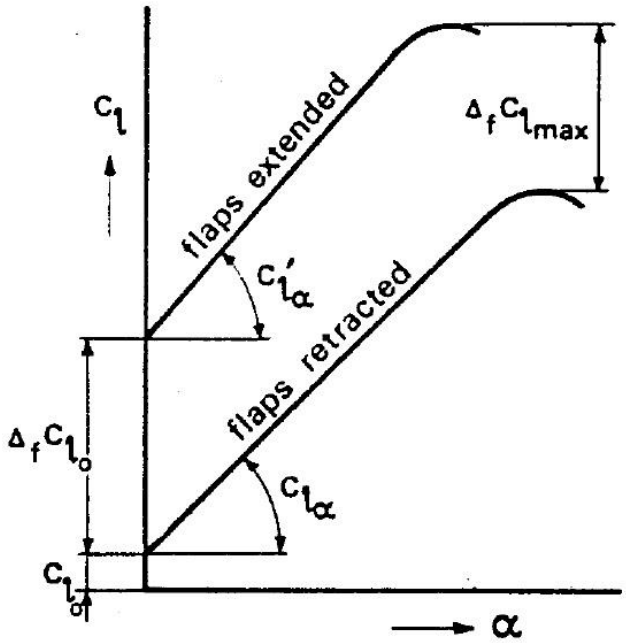

Figure 32: Effect of trailing-edge flap deflection on section lift.

It will be assumed that for conventional wing shapes the lift curves are linear for moderate angles of attack. It can be observed that even if the lift curve of the basic section is fairly nonlinear due to trailing edge stall, the flapped section exhibits a more linear behavior when the flow near the trailing edge is cleaned up by the flap.

The determination of the lift curve is subdivided into prediction of the increment in lift at zero angle of attack, from which an expression for effectiveness will be found, and the (increment in) maximum lift coefficient and the lift-curve slope at small angles of attack.

For small flap deflections, the rate of change of lift with flap deflection at constant angle of attack is frequently used as a measure of flap effectiveness

$$C_{l_\delta} = \left(\frac{\partial C_l}{\partial \delta_f}\right)_{\alpha=cost.} \qquad (2.6)$$

Another convention used is the rate of change of zero-lift angle of attack with flap deflection

$$\frac{\partial \alpha}{\partial \delta_f} = \alpha_\delta = \frac{(C_{l_\delta})_{\alpha=cost.}}{(C_{l_\alpha})_{\delta=cost.}} \qquad (2.7)$$

The basis for several estimation methods is formed by Glauert's linearized theory for thin airfoils with flaps [19]. A result obtained from this theory for the lift due to flap deflection is as follows

$$\alpha_\delta = 1 - \frac{\theta_f - \sin\theta_f}{\pi} \qquad (2.8)$$

where

$$\theta_f = \cos^{-1}\left(2\frac{c_f}{c} - 1\right) \qquad (2.9)$$

Figure 33 gives a plot of α_δ as a function of the chords ratio (relative flap chord) $\frac{c_f}{c}$, in which c_f is the flap chord and c is the fixed surface chord. From these simple formulas and charts, it is then possible to quickly find the effectiveness value of the mobile part, which depends only on the chords ratio and (when non-linear effects will be introduced) the deflection of the movable part, providing a less accurate estimation of the method proposed by Roskam [15] that was previously discussed.

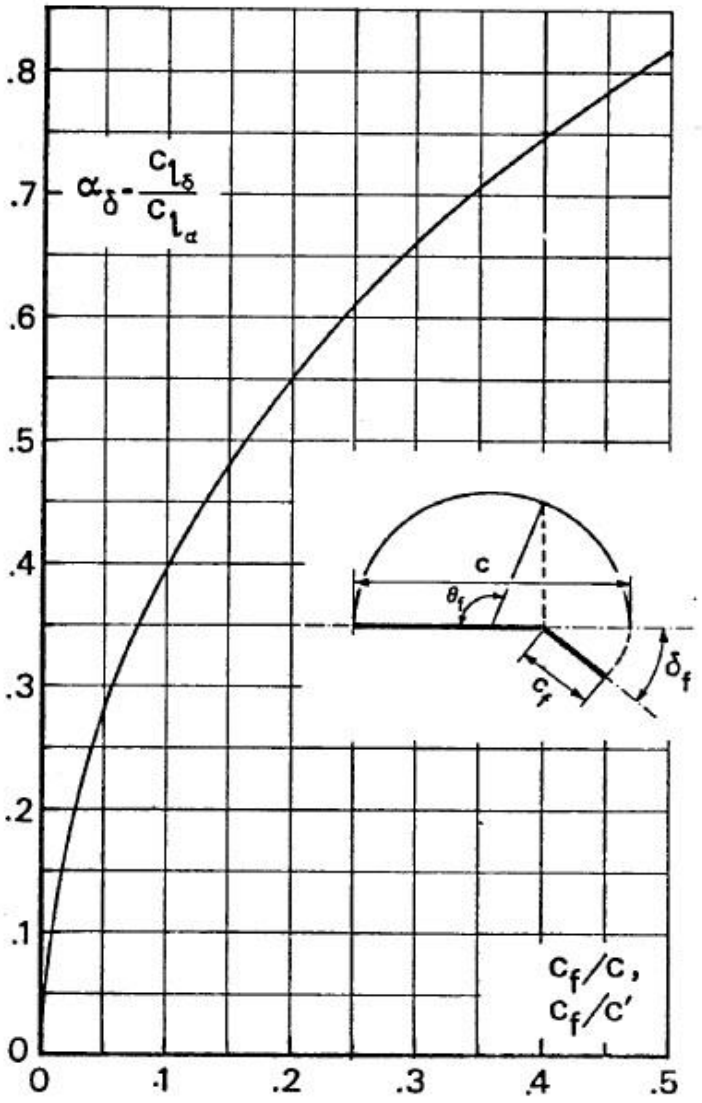

Figure 33: Theoretical flap lift factor.

The theoretical increment in lift at zero angle of attack, $\Delta_f C_{l_0}$, is thus

$$\Delta_f C_{l_0} = \alpha_\delta C_{l_\alpha} \delta_f \qquad (2.10)$$

It is found that the theoretical lift effectiveness cannot be realized in practice. For small flap deflections, it is possible to obtain approximately 70% to 85% of the theoretical value, depending upon the type of flap system, while for large flap angles, e.g. those used in the landing configuration, the lift effectiveness may go down to approximately 50% of the theoretical value given by the equation (2.8). The following reasons may be quoted:

- for large flap deflections, linear theory is in error when compared with the exact theory given by [20];
- the viscosity of the flow is responsible for separation at large flap angles. For plain flaps, such as the rudder studied for the present thesis work, separation starts to occur at 10 to 15 degrees of flap deflection.

The departure from the theoretical value is taken into account by means of a flap effectiveness factor, η_δ

$$\Delta_f C_{l_0} = \alpha_\delta C_{l_\alpha} \delta_f \eta_\delta \qquad (2.11)$$

Diagram for estimating η_δ for a plain flap is presented in Figure 34, from which it is possible to note that the flap effectiveness is sensitive to the condition of the boundary layer at the knuckle and therefore the flap chord ratio has been used as a correlation parameter. The effect of sealing the gap appears to be considerable for a plain flap, but for control surfaces an unsealed gap may be acceptable.

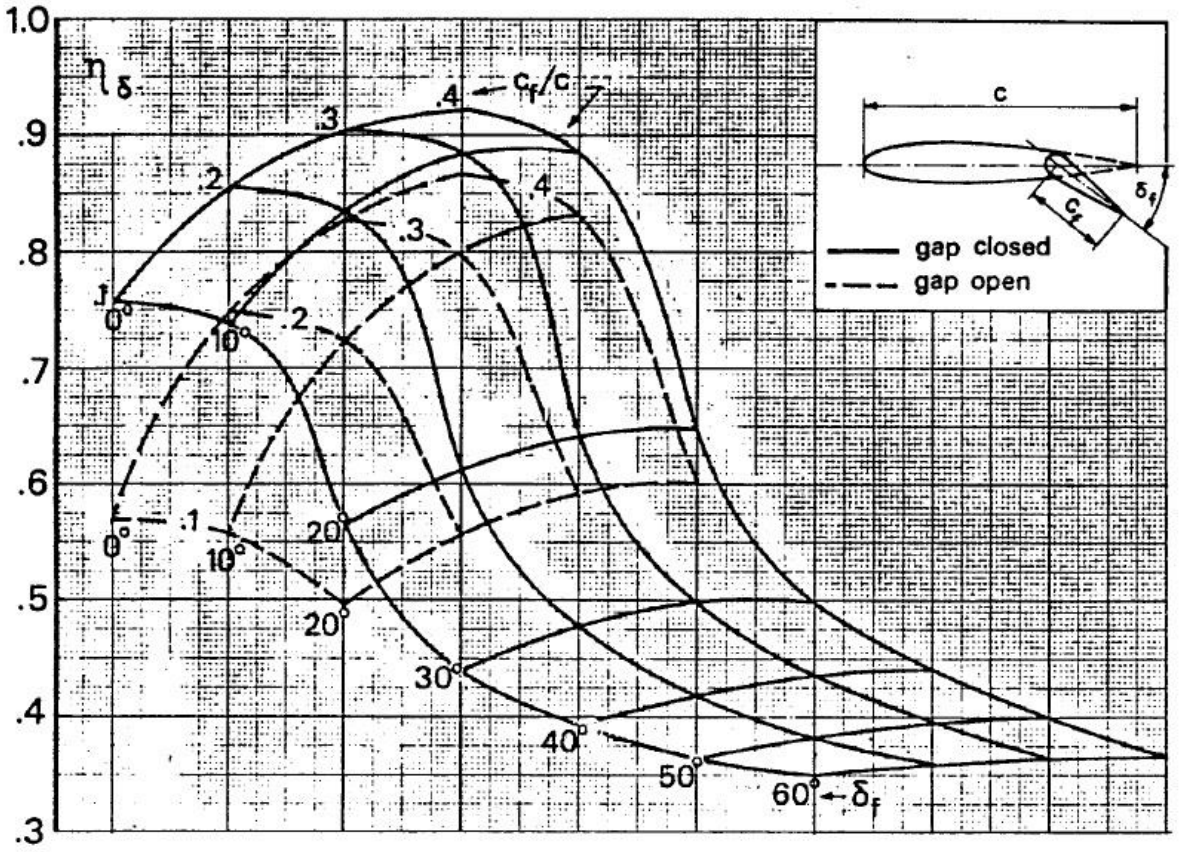

Figure 34: Lift effectiveness factor for plain flaps (derived from experimental data proposed in [21])

From the above considerations, it is therefore possible to finally find an easy expression for the effectiveness of the mobile part, inclusive of non-linear effects

$$\tau_{(V)} = \alpha_\delta \eta_\delta \qquad (2.12)$$

which it is the expression that will be used later to make comparisons between semi-empirical methods and numerical results.

2.3 McCormick Method

The method proposed in the McCormick's text [16] takes into account the same geometrical parameters of the one proposed in Torenbeek's text [6], but with a different formulation, although starting from the same basic assumptions.

The starting point is the fact that frequently an estimation of the increment ΔC_l below stall produced by a flap deflection is needed also in analyzing the effectiveness of movable control surfaces, which frequently can be considered as plain flaps.

If an airfoil section has a lift curve slope of C_{l_α} and the flap deflection produces an increment of ΔC_l, the angle of zero lift, α_{0_l}, is increased (in magnitude) by

$$\Delta\alpha_{0_l} = \frac{\Delta C_l}{C_{l_\alpha}} \qquad (2.13)$$

The rate of increase of the magnitude of α_{0_l} per unit increase of the flap angle δ_f is referred as the flap effectiveness factor, τ (which will become τ_V in this thesis work). Thus, for a flapped airfoil, the lift coefficient can be written as

$$C_l = C_{l_\alpha}(\alpha + \tau\delta_f) \qquad (2.14)$$

where α is the angle of attack of the airfoil's zero lift line with the flap retracted. Theoretically τ is a constant for a given flap geometry, but the flap behavior with δ_f is rather non-linear and hence τ must be empirically corrected by a factor η (in the same way done by Torenbeek method) to account for the effects of viscosity. Including η, the previous equation becomes

$$C_l = C_{l_\alpha}(\alpha + \eta\tau\delta_f) \qquad (2.15)$$

The functions τ and η can be obtained from Figure 35 and Figure 36. Figure 36 (note that curves apply for thickness ratios of approximately 12% and flap chord fractions of 40% or less) is empirical and is based on data from References [22], [23], [24] and [25]. Although there is some scatter in the data, as faired, the comparisons between the various types of flaps are consistent. In particular, the plain flap is fairly good out to about 20° and then, apparently the flow separates from

the upper surface and the effectiveness drops rapidly, approaching the curve for split flaps at the higher flap angles.

In the present thesis work the mobile part can be safely assimilated to a plain flap, and then in Figure 36 will be taken into account only the curve relative to this type of moveable surface.

Figure 35 is based on the thin airfoil theory. The effectiveness τ can also be obtained using numerical methods. Weissinger's approximation can be applied to the flapped airfoil using only two point vortices to represent the airfoil. Placing one vortex on the quarter chord of the flap and the other on the quarter chord of the remainder of the airfoil (point at three-quarter of the chord) leads to

$$\tau = \frac{3\,(3 - 2c_f)c_f}{4\,(1 - c_f)c_f + 3} \qquad (2.16)$$

where c_f is the fraction of chord that is flapped. The last equation gives a value of effectiveness which is approximately 10% lower than the value obtained from Figure 35, for $\frac{c_f}{c}$ values of around 0.25. However, in the same way as done in the previous section, during the comparisons between numerical and semi-empirical methods, the following expression will be used for evaluating the vertical tail plane (rudder) effectiveness

$$\tau_V = \tau\,\eta \qquad (2.17)$$

In which τ is found from Figure 35 and η is found from Figure 36. In conclusion, also this method considers only two geometric parameters, and therefore results less accurate than the first method presented in this chapter (the one proposed on the text written by Roskam).

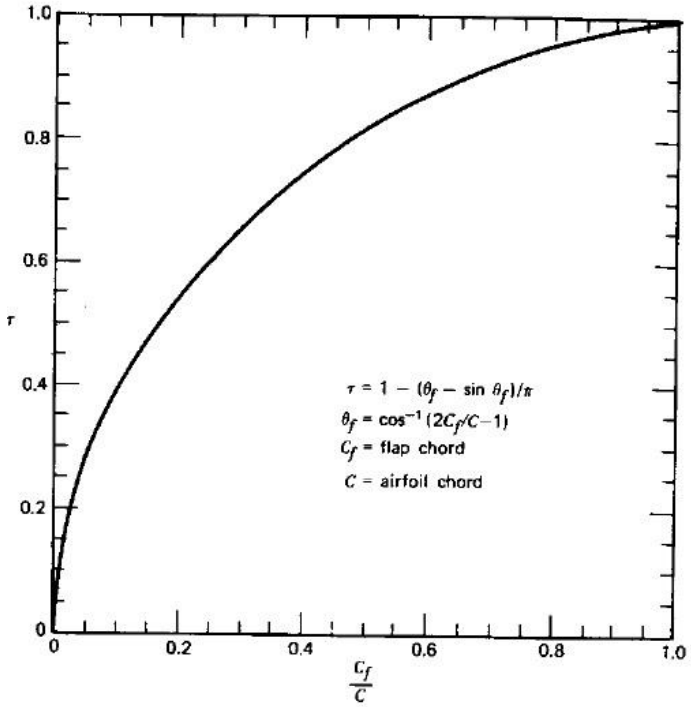

Figure 35: Flap effectiveness factor.

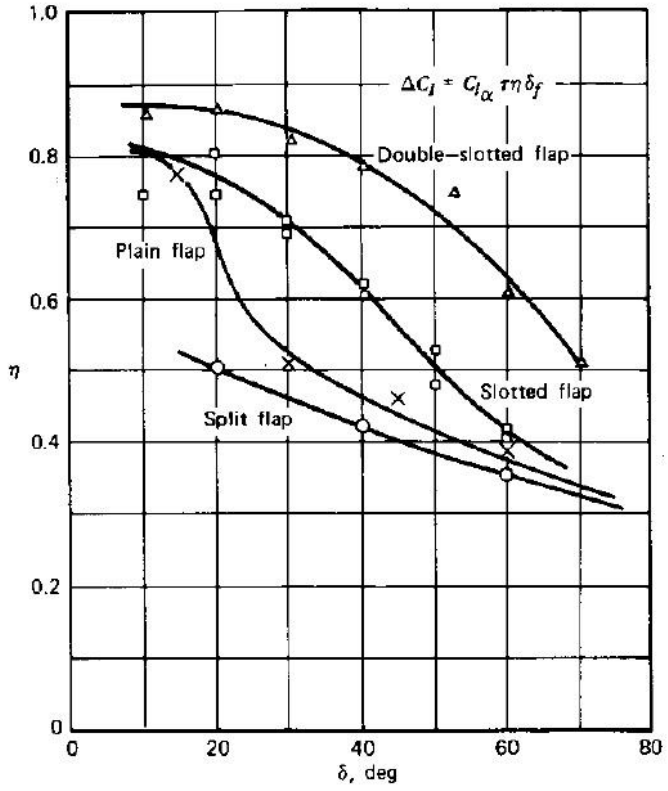

Figure 36: Correction factor to flap effectiveness factor τ.

2.4 A Comparison between semi-empirical methods and WT tests

Applications of semi-empirical methods and comparisons with numerical results have already been performed by the DAF research group[2], Dept. of Industrial Engineering of the University of Naples "Federico II". Recent activities (like P2012 wind-tunnel tests [26] and CFD analyses, VEDSC rudder analyses [33] and Dorsal fin analyses [58]) about aircraft control surface effectiveness estimation had in fact highlighted the necessity to investigate the phenomenology both qualitative and quantitative, at several angles of attitude and deflections of control surface, to better predict the control surface effectiveness (especially at high deflection angles).

In particular, part of the work in Ref. [26] was focused on the evaluation of control surface effectiveness on several geometries of horizontal tail and vertical tail (with and without dorsal fin). Figure 37 show the P2012 vertical tail planform (note the high chords ratio, especially at tip). Figure 38 shows the yawing moment coefficient curves at different sideslip and rudder deflection angles. Figure 39 shows the close agreement between numerical and experimental results for the P2012 vertical tail, while the semi-empirical method underestimates rudder effectiveness.

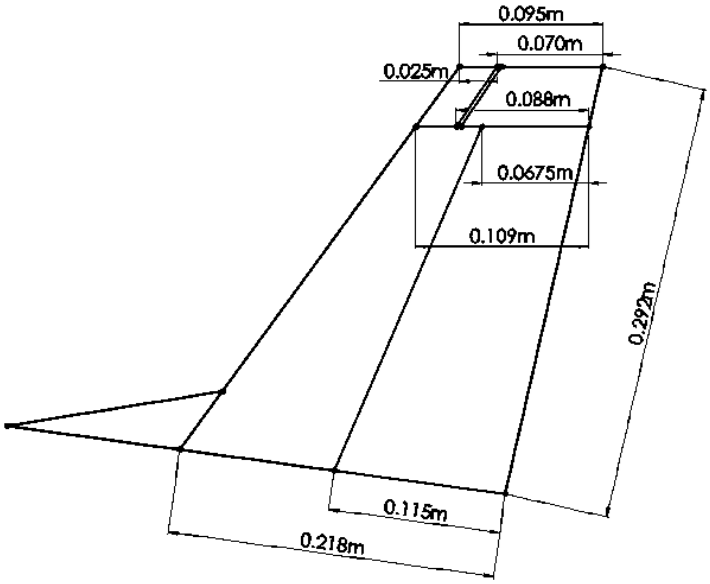

Figure 37: Tecnam P2012 vertical tail plane [26].

[2] Design of Aircraft and Flight technologies http://wpage.unina.it/fabrnico/DAF/

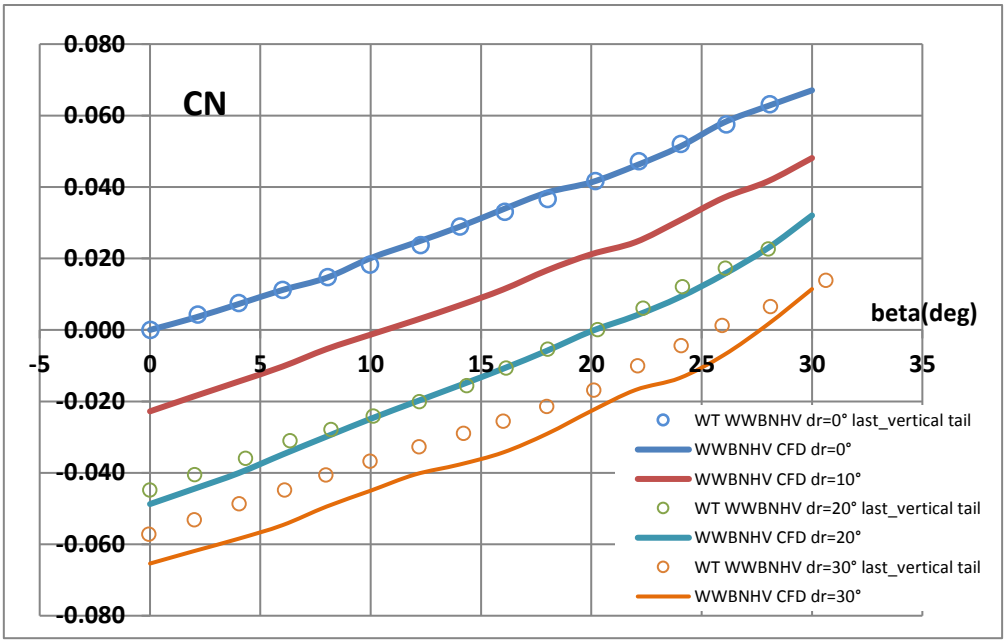

Figure 38: Yawing moment coefficient C_N vs sideslip angle β [26].

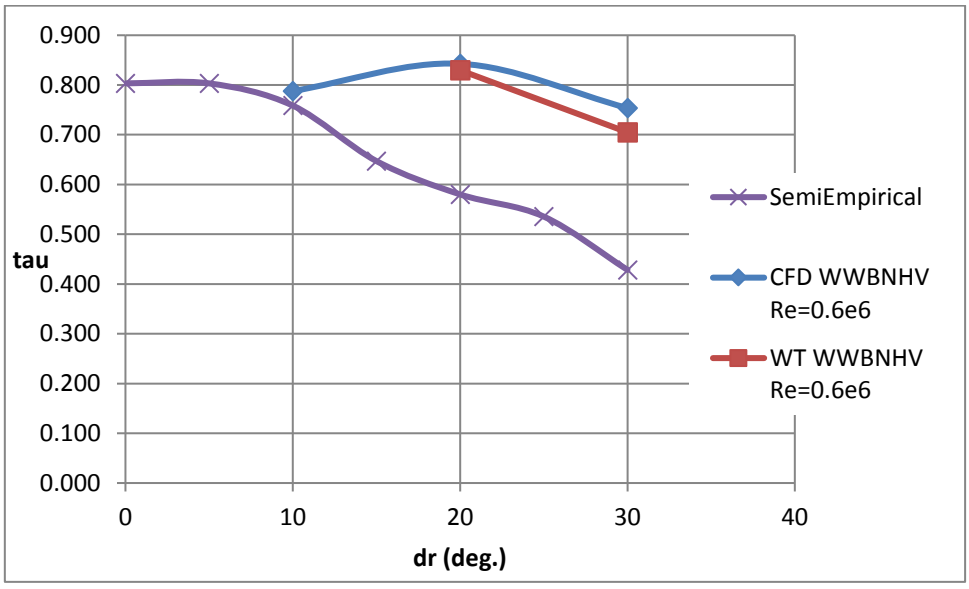

Figure 39: Comparison between numerical, semi-empirical and wind tunnel tests results in terms of rudder effectiveness τ.

The abovementioned analyses have highlighted the following problems on control surface effectiveness estimation:

- discrepancies among different methodologies especially in non-linear range of deflections;
- lack of data for high chord ratios, usually adopted on commuter aircraft vertical tail;

- different phenomenology for horizontal and vertical tail (AR and dorsal fin).

2.5 Conclusive Remarks

The semi-empirical methods presented in sections 2.1, 2.2, and 2.3, although starting from the same basic theory, namely the theory of the thin airfoil by Glauert [19], come to different results in the linear field (small deflections of the rudder) and also in non-linear field (large deflections of the rudder). In particular, the most accurate and responsive to the reality method seems to be the one proposed in Section 2.1, i.e. that found in the text written by Roskam, while appear to be slightly less accurate the methods proposed in Torenbeek (section 2.2) and McCormick (section 2.3) texts, which instead are easier to use, given the reduced number of data to take into account.

In particular, the big difference among the methods, as previously highlighted, lies in the number of geometric parameters taken into account. Anyway, it can be stated that there is no right method, since all of these are based on empirical data obtained in the past, although the one proposed in section 2.1 seems to be the most accurate.

The analyses mentioned in section 2.4 have highlighted some problems on control surface effectiveness estimation, and this was the factor that stimulated the actual work: there is no method specifically developed for this issue, although it occupies a relevant position in the preliminary design of a vertical tail plane. This new method, described in Chapter 4, is realized with the help of the CFD (the tools used are described in Chapter 3).

3 The Numerical Approach

The present thesis work had the main objective to create a new approach for the estimation of directional control surface effectiveness. The idea was to create a new database through CFD Navier-Stokes aerodynamic analyses to estimate the parameter of interest, the rudder effectiveness τ. The parametric analyses have been performed on the isolated vertical tail geometry. The analysis matrix for the isolated vertical tail here used will be presented in Chapter 4.

3.1 The CFD Approach for Stability and control characteristics

Technological progress in the aerodynamics design phase is a possible use of the CFD. This chapter is a description of the main tool that was used to fulfill the objective of this work, the commercial CFD software STAR-CCM+. This tool requires the definition of a physical model responsive to the actual phenomena to be analyzed. The more accurate the physics models involved, the more realistic will be the results. Most of the Section 3.1, unless otherwise stated, comes from [27]. Section 3.1.7 will describe the SCoPE computational grid, necessary to deal with many simulations of millions of cells.

The classic conceptual and semi-empirical methods used in aircraft design, with their capabilities and limits, have been deeply assessed in the previous chapters. Here, a new approach by CFD is discussed. The numerical tools used are described. Test cases have been performed and here presented.

3.1.1 Application of CFD in Aircraft Design

The use of computational fluid dynamics for industrial aircraft design started in the ’60s and, since then, it has grown from a tool used to support wind tunnel or flight experiments to an identifiable new technology standing on its own, making important contributions to all stages of the design of a flight vehicle [34].

At that time, only wind tunnel tests could provide useful info about directional stability [35], especially for the high subsonic and supersonic flow regimes, because of vorticity and shock waves [36]. The wind tunnel is traditionally the primary tool to provide aerodynamic inputs for simulation databases. However, some issues in wind tunnel testing methods can lead to serious errors in the predicted stability and control characteristics [37]. For instance, the operation at a lower than free flight Reynolds number causes large discrepancies on boundary layer separation in certain configurations. Moreover, wind tunnel tests require both the construction of a model and an adequate test facility. Additionally, the lag time between the paper design and the wind tunnel results can be considerable. Finally, any configuration change requires a change of the test model. This greatly increases the cost of the product and its time to market.

In the ’70s first computer programs began to appear on the scene, with the application of linear, potential, subsonic flow theory: panel methods. These are numerical schemes for solving the Prandtl-Glauert equation for linear, inviscid, irrotational flow about aircraft flying at subsonic or supersonic speeds. Initially the quasi vortex-lattice method was applied and modified to account for wing-body effect in sideslip, then more and more sophisticated panel methods, developed for rapid accurate estimates of the aerodynamic characteristics of aircraft and missile configurations at supersonic speeds, provided solution (in potential flow) for almost any geometry. There are fundamental analytic solutions to the Prandtl-Glauert equation known as source, doublet, and vorticity singularities. Panel methods are based on the principle of superimposing surface distributions of these singularities over small quadrilateral portions, called panels, of the (approximate) aircraft surface. The resulting distribution of superimposed singularities automatically satisfies the Prandtl-Glauert equation. To make the solution correspond to the desired geometry, boundary conditions are imposed at discrete points (named control points) of the panels [38]. The unknowns of the equations are located only on the panels, that is only on the aircraft

surface, hence reducing the order of the problem by one and permitting the handling of complex geometries with a relative small number of unknowns [39].

In their simplest form, panel codes do not account for viscosity. Viscosity is responsible of momentum loss in boundary layer because of skin-friction and pressure drag, increasing boundary layer thickness, decreasing lift gradient, and flow separation [40]. Neglecting viscosity gives a good approximation only in attached flow regimes. This limit can be overcome by modern CFD [13]. Panel codes can be coupled with boundary layer codes to estimate the friction drag (panel methods are restricted to inviscid, irrotational and linear flow): a displacement thickness, due to the loss of momentum in the boundary layer, is calculated on the body walls by the viscous code; this displacement thickness is added to the previous geometry, providing the new input surface of the panel code; the process is repeated until convergence is reached [38].

However, a fundamental limitation remains: panel methods solve only linear differential equations [38], i.e. they can simulate only attached flows. As the panel methods do not compute the pressure in the separated flow regime, prediction of pressure drag is not possible [41]. Finally, by their own nature, panel codes can hardly provide wake-body interference, since the shape of the vortex sheet is unknown *a priori* [39]. It is possible to determine the pressure acting on bodies in the region of wing-body interference in subsonic flow by a hybrid panel method [42], but viscosity is still neglected.

A quasi-vortex-lattice method has been applied and modified to account for wing-body effect in sideslip [43]. Sophisticated panel methods provided rapid accurate estimates of the aerodynamic characteristics of aircraft and missile configurations at supersonic speeds [36]. Examples of panel codes used to evaluate airplane directional stability and control can also be found in Park et al. [44]. The complexity and costs of wind tunnel tests and the increasing viscosity effects at high angles of incidence led to more and more complex numerical tools, as panel methods that account for friction drag and Navier-Stokes solvers [37], [40], [45]. Navier-Stokes codes represent, in principle, the true

simulation of the physics of the viscous flow [41]. Compared to the panel codes, they require a much longer solving time, also due to the generation of an adequate computational grid (mesh), and the problem of turbulence modeling is still open. However, adequate turbulence models do exist for aeronautical applications and the possibility to simulate and visualize a viscous flow pay back these disadvantages, as will be shown next.

Thus, the limits of wind-tunnel investigation and panel codes can be overcome by modern CFD. The powerful Navier-Stokes tools nowadays avail-able offer significant benefits as companions to the experimental methods to predict aerodynamic parameters. Since 1985 the bigger computational power and the development of new solution techniques and turbulence modeling have permitted an extensive application of CFD in aircraft aerodynamic analysis and design [34], [46], [47]. In the last 30 years, CFD methods made use of finite differences [48], finite elements [49], and finite volume methods [46]. CFD helps designers to investigate the aerodynamics of the aircraft in the early phase of its design, in opportune conditions (viscous, compressible, transonic flow). The progress of numerical analysis techniques involved also the low subsonic flow field [44], [49]. An example of application about fuselage aerodynamics is found in the report by Embraer [50]. Moreover, CFD may provide a great aid in accounting non-linear effects in aircraft design, as shown in [33].

In the last 15 years, the American Institute of Aeronautics and Astronautics (AIAA) has promoted the Drag Prediction Workshop (DPW) and the High Lift Prediction Workshop (HiLiftPW) Series to assess the state of the art of modern computational fluid dynamics methods using geometries and conditions relevant to commercial aircraft. In the last workshops, the experimental investigations focused on the NASA Common Research Model (CRM) wing-body configuration [51], [52]. The idea is to setup a public domain database of geometries, numerical, and experimental results to evaluate the effectiveness of current Navier-Stokes solvers and modeling techniques, to promote open discussion on areas needing additional research and development, to share knowledge and reduce the variability of CFD results [53], [54] .

High lift prediction, in particular, is both difficult and fascinating. The numerical aerodynamic analysis of high lift configuration of commercial aircraft is a crucial item to reduce the number of wind tunnel tests and give a well-suited instrument for the industrial design of the high lift systems. The numerical simulation of these configurations is very complex, due to difficulties to simulate separations phenomena, unsteadiness, confluent boundary layers, transition, and so on. The summary of the first HiLiftPW by Rumsey et al. [53] states that the Spalart-Allmaras (SA) turbulence model [55] gives results in closer agreement with experiments than other – and more complex – models. This situation is even better with refined grids. In [33] is performed a test case of the second HiLiftPW, applying the SA model on user-defined unstructured grids with different refinement levels, obtaining encouraging results: the stall and post-stall behavior have been predicted quite accurately, the angle of stall has been correctly evaluated, and the maximum lift coefficient has been underestimated by less than 5% [56].

In the design process [8], [9], [34] CFD occupies the aerodynamics group with an increasing importance as computer speed, grid generation, and solving techniques progress with time. A CFD package ideally provides in an integrated environment:

1. pre-processing (geometry modeling, CAD repair);

2. grid generation;

3. solving;

4. post-processing (visualization and analysis of the results).

The solver provides physical and numerical modeling, the implementation of these models in the computer, and the execution of the code. This process involves both hardware and software [34]. Typical CFD design applications are the following:

- design and analysis of aircraft and component shape;

- performance, i.e. force and moment data to determine lift, drag, and moments;
- integration of components, e.g. wing-fuselage intersection or wing-pylon-nacelle group;
- evaluation of stability and control, by aerodynamic coefficients, force, and moment data;
- loads, for structural design;
- aero-servo-elasticity.

3.1.2 Simulation Workflow

The most general workflow is represented in Figure 40 and briefly described here.

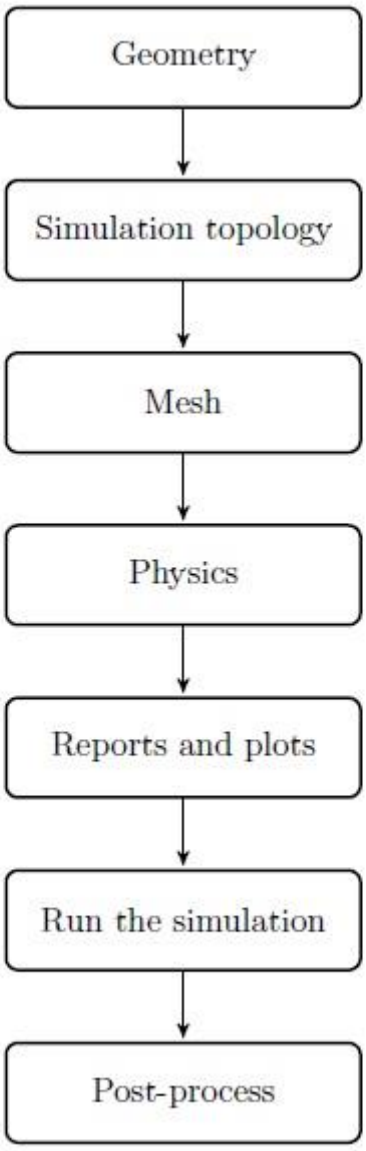

Figure 40: General sequence of operations in a STAR-CCM+ analysis.

- **Geometry** can be imported from other CAD software or created directly in Star-CCM+, though in version 6 (used in this work) the CAD environment can handle only very simple shapes. What-ever the method, geometry is a collection of surfaces and curves.
- **Simulation Topology**: Is the computational model defined as regions and boundaries to which physics can be applied. For external aerodynamics, a volume (e. g. a block shape) representing the fluid domain to be simulated must contain the entire geometry inside.
- **Mesh**: Is the numerical domain. STAR-CCM+ can easily and automatically generate surface and volume mesh, once defined several parameters, including size and refinement quality.
- **Physics Models**: Can be easily enabled. STAR-CCM+ can handle single and multi-phase fluid flow, heat transfer, turbulence, solid stress, dynamic fluid-body interaction, aeroacoustics and related phenomena.
- **Reports, Monitors and Plots**: Should be defined and activated to check for convergence, since STAR-CCM+ uses an iterative procedure to reach the solution to the transport equations that satisfies the boundary conditions for a chosen scenario.
- **Run the simulation**: Will automatically initialize the solution and launch the solver. For an interactive session, residuals will be plotted in the client workspace and reported in the output window. For batch sessions, residuals will be echoed to the command console. The simulation can be stopped and resumed anytime.
- **Results**: Can be visualized with scenes as contours, vectors and streamlines. It is possible to create animated scenes. Scatter plots are also possible. In an interactive session, graphical results can be visualized as the simulation run, step by step.

3.1.3 Mesh generation

The starting point for generating a mesh is a surface description. These surfaces usually come from CAD or similar packages. Mesh in STAR-CCM+ can be imported from an external source or generated within the software CAD environment.

The core volume mesh can contain either trimmed, polyhedral or tetrahedral type cells. Prismatic cell layers can be included next to wall boundaries to account for boundary layers. Volumetric controls using shapes as rectangles (bricks) and spheres can also be included to increase or decrease the mesh density of both the core mesh and/or prism layer mesh. Alternatively, the thin mesher can be used to produce either a tetrahedral or polyhedral volume mesh for thin geometries. The mesh is automatically built on the regions and boundaries defined earlier by the user (see Figure 40), once defined (at least) a mesh continuum and its parameters. A mesh continuum is the collection of meshing models that are used to generate the surface and volume mesh for the input geometry representing the individual regions to be used for the simulation.

Basically, the mesh size can be defined in two ways: relative and absolute. The relative size consists in choosing the base size of the mesh, that is the reference length of the problem to study, and all other sizes will be a percentage of this base size. On the contrary, an absolute size will be fixed and unrelated to the reference value. Of course, it is possible to have a part defined with relative sizes and another part defined in an absolute way. Volume mesh is always created on a surface mesh. That is volume mesh size propagates from the surface mesh size. Three different parameters are used to control the surface size, namely:

- target size;
- minimum size;
- maximum size.

The target size is the desired edge cell length on the surface while the minimum and maximum sizes control the lower and upper bounds of the cell edge lengths (when refinements from curvature and/or proximity effects are included). Three combinations of the target, minimum and maximum surface sizes are allowed:

- minimum and target size;

- minimum and maximum sizes;
- only minimum size.

3.1.4 Defining the physics

The mechanism is the same of the mesh generation: one or more physics continua models must be enabled.

In general, STAR-CCM+ models and solvers rely on the following areas:

- space, time and motion;
- materials;
- flow and energy;
- species;
- turbulence and transition;
- radiation;
- aeroacoustics;
- combustion;
- multiphase flow;
- solid stress;
- electromagnetism.

The analysis carried on for this work required only a steady state solver and an incompressible viscous flow model. It is known [7] that a viscous flow can be laminar or turbulent and that viscosity can be accounted only in a small region of the fluid adjacent to the body surface – the boundary layer. The flow regime imposed in the simulation files of this work was turbulent, since a laminar flow around an airplane is unrealistic.

The turbulence model chosen was Spalart-Allmaras. The original Spalart-Allmaras model was developed primarily for the aerospace industry and has the advantage of being readily implemented

in an unstructured CFD solver, unlike more traditional aerospace models. It solves a single transport equation that determines the turbulent viscosity. This is in contrast to many of the early one-equation models that solve an equation for the transport of turbulent kinetic energy and required an algebraic prescription of a length scale [27]. It gives good results with attached boundary layers and flows with mild separation. In short, it's simple, fast, suitable for the scope of this work [56] and reliable for external aerodynamics, even at high angles of attack and high lift configurations for certain geometries, provided that the mesh is fine enough.

3.1.5 Convergence

The stopping criterion chosen was a prescribed number of iterative steps order of magnitude as thousand. Convergence is judged by looking at the residual plot and the wall y+. The residual in each cell represents the degree to which the discretized equation is not completely satisfied. In a perfectly converged solution, the residual for each cell would be equal to machine roundoff. Thus, the residual is the error generated by the approximate solution when it is substituted into the linear system. This is the concept of the residual and it is always valid, no matter how complicated its mathematical expression.

3.1.6 The SCoPE grid infrastructure

At time of writing, no desktop computer could handle CFD 3D simulations of millions of cells in a reasonable amount of time, so the solver of this CFD package has been widely used on the grid computing infrastructure provided by the University of Naples "Federico II" to simulate lots of configurations in a short amount of time. *Sistema Cooperativo per Elaborazioni Scientifiche Multidisciplinari* (SCoPE) is a scientific data center, based on a grid computing infrastructure (Figure 41), and it is a collaborative system for scientific applications in many areas of research. It is a project started in 2006 by the University of Naples "Federico II", in continuous evolution [57]. The scientific applications are of the areas of Astrophysics, Chemistry, Mathematics, Medicine, Engineering and Physics. The data center is located in the Monte S. Angelo Campus, which already

hosts the Faculty of Sciences and it is close to the Faculty of Engineering, with kilometers of preexisting optical fibers. The network infrastructure is shown in Figure 42.

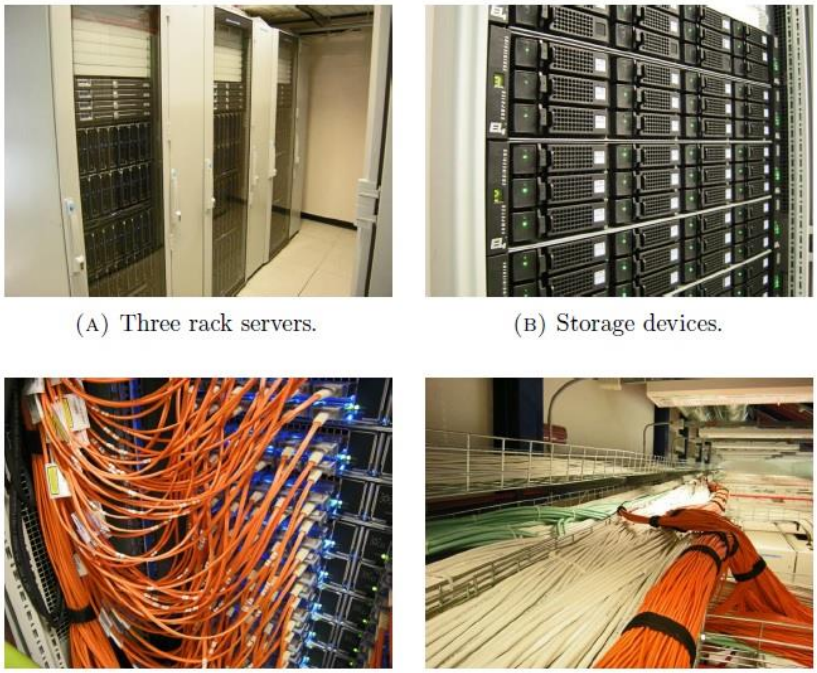

(A) Three rack servers. (B) Storage devices.

(C) Fiber optic connections. (D) Cables above the racks.

Figure 41: Some images of the SCoPE data center [57].

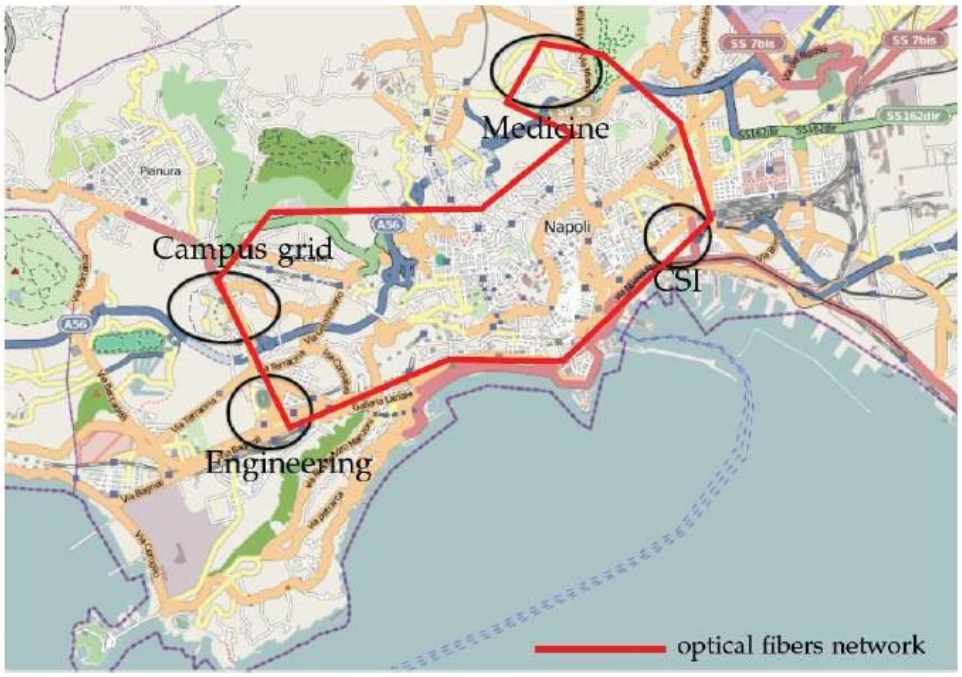

Figure 42: Optical fibers network link for the Grid ScoPE [13].

A number of 160 licenses (one per CPU) were available for these investigations. The software manual [27] recommends to employ a CPU every 250 000 cells, hence several simulations have been performed in parallel at the same time, e.g. 2 or 3 runs with 32 CPUs each. The computational time is a non-linear decreasing function with CPUs number, on a linear plot. On a logarithmic plot it is a linear function instead. Figure 43 represents the time necessary to get a converged solution versus CPUs number, in the two different scales, with data obtained by running a body-vertical configuration with 1800000 cells for 2000 iterations on SCoPE. Runs with 16, 32 or 64 CPUs per simulation were commons to get results within a couple of days.

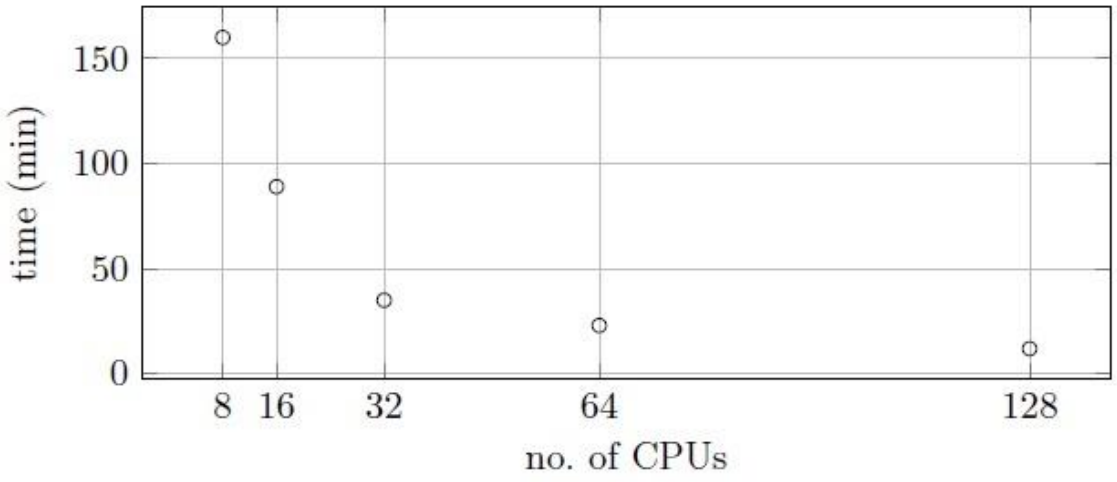

(A) Linear plot.

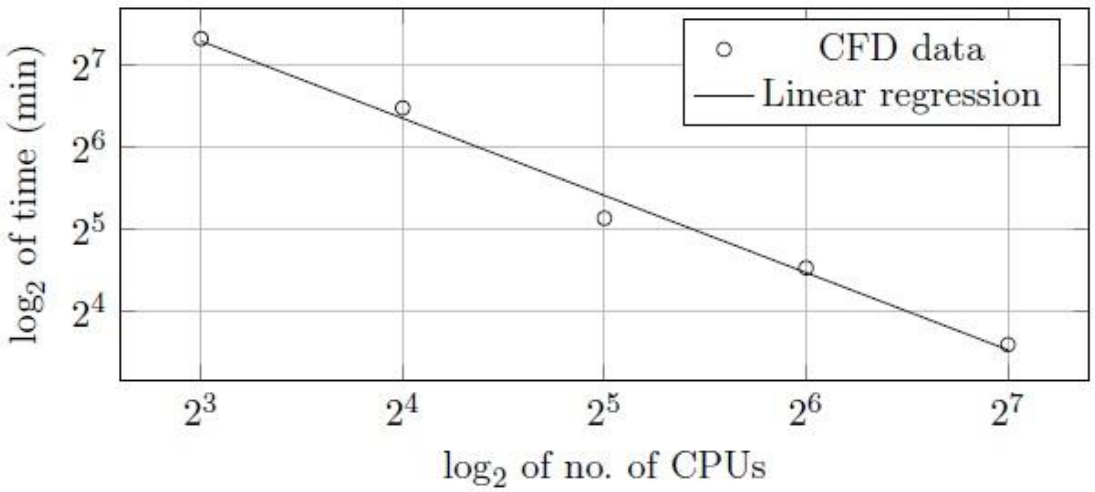

(B) Logarithmic plot.

Figure 43: CPU time for 2000 steps on 1800000 polyhedral cells.

Here follows other interesting data:

- localization in a building of about $150m^2$.
- power plant capable of delivering 1MW of electric power in a continuous mode;
- efficient cooling system, capable of dissipating 2000W/m^3 and 30 000W per rack;
- standard (Gigabit Ethernet) networking infrastructure, with a high capacity switching fabric;
- low latency (Infiniband) networking infrastructure, with a single switching fabric for each group of 256 servers;
- large storage capacity, both NAS (Network Attached Storage) working with the ISCSI protocol, and SAN (Storage Area Network), working with a Fibre Channel Infrastructure;
- open source (Scientific Linux) for the operating system;
- integrated monitoring system for all the devices of the data center, able to monitor the most relevant parameters of server, storage, networking, as well as all the environmental parameters (as temperature, humidity and power consumption).

For more information about the SCoPE project it is possible to visit the website in [57].

3.2 Longitudinal Test-Case

Test cases are necessary to assess the compliance of the CFD results to the available experimental data, before attempting to investigate anything else. Main reference for this section is [29].

In summary, in this section a rectangular wing has been analyzed at various angles of attack, in symmetric flow, and the numerical results has been compared with experimental results obtained from wind tunnel tests conducted by NACA in 1944. No discussion is made on the results since the primary interest of this section is the check of the previously stated compliance.

3.2.1 NACA report WRL 186

In the work carried out by NACA (National Advisory Committee for Aeronautics) in October 1944, force-test measurements were made in the Langley 4-by 6-foot vertical tunnel to determine the aerodynamic characteristics of an NACA 0009 semi-span tail surface of rectangular plan form, equipped with flaps of various nose shapes and overhangs. The flap chord was 30 percent of the airfoil chord. A few tests were made also to determine the effectiveness of a balancing tab on various flap arrangements.

The NACA in that historical period was conducting an extensive investigation of the aerodynamic characteristics of control surfaces in two-dimensional and three-dimensional flow, in order to provide design data and to determine flap arrangements suitable for use as control surfaces. A series of tests were made to determine the effects of overhang, nose shape, and gap on the aerodynamic characteristics of the above-mentioned NACA 0009 airfoil in two-dimensional flow; the results of these investigations are presented in [30].

The investigation to which is related the present test case consisted of tests in three-dimensional flow about a rectangular semi-span tail surface. The purpose of this investigation was to help establish a correlation between aerodynamic characteristics in two-dimensional and three-dimensional flow. Using a surface having constant airfoil, flap, and balance chords, only relatively simple planform corrections were required when approximate corrections were used.

The tests were made in the Langley 4- by 6-foot vertical tunnel [31] modified as discussed in [32]. The 2-foot-chord by 3-foot-semispan model was made of laminated mahogany and conformed to the dimensions of Figure 44 and to the NACA 0009 profile, the stations and ordinates of which are given in Table 3. Since the tail surface had a tip of revolution, the tip plan form was the same as the contour of the upper and lower surfaces of' the airfoil. The flap chord was 30 percent of the airfoil chord at each spanwise station. For the complete tail surface represented by the semispan model, the aspect ratio was 3 and the taper ratio 1.

Station	Ordinates	
	Upper	Lower
0	0	0
1.25	1.42	-1.42
2.5	1.96	-1.96
5.0	2.67	-2.67
7.5	3.15	-3.15
10	3.51	-3.51
15	4.01	-4.01
20	4.30	-4.30
25	4.46	-4.46
30	4.50	-4.50
40	4.35	-4.35
50	3.97	-3.97
60	3.42	-3.42
70	2.75	-2.75
80	1.97	-1.97
90	1.09	-1.09
95	.60	-.60
100	(.10)	(-.10)
100	0	0
L.E. radius = 0.89		

Table 3: Ordinates for NACA 0009 Airfoil (All dimensions in percent chord)

$0.50c_f$ overhang	
Station	Ordinate
0	0
.35	.88
.85	1.26
1.85	1.68
2.85	1.96
3.85	2.15
4.85	2.30
5.85	2.42
6.85	2.52
8.85	2.64
10.85	2.70
12.85	2.72
L.E. radius = 1.23	

NATIONAL ADVISORY
COMMITTEE FOR AERONAUTICS

Table 4: Elliptical Nose Flap Profile (All dimensions in percent chord)

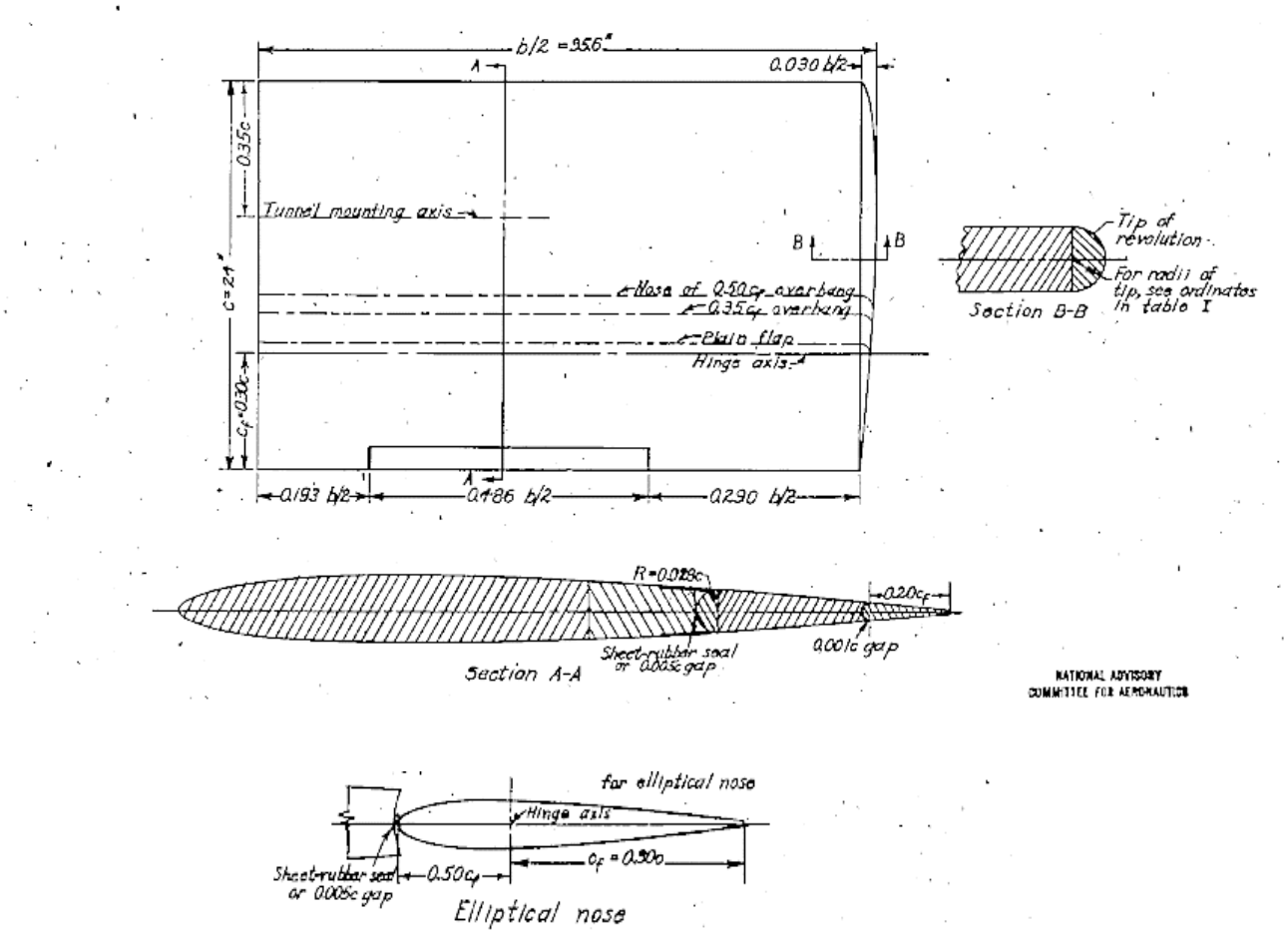

Figure 44: Details of an NACA 0009 Rectangular semi-span tail surface and flap profile. Aspect Ratio = 3.

The plain unbalanced flap and the flap with overhang balance are shown in Figure 44. The $0.50c_f$ overhang was tested with elliptical nose shape (See Table 3 and Table 4). The elliptical nose was a true ellipse faired tangent to the airfoil contour at the hinge axis. The gap was fixed at 0.005c.

The tests were made at a dynamic pressure of 15 pounds per square foot, which corresponds to an air velocity of about 76 miles per hour at standard sea-level conditions. The test Reynolds number was 1,430,000 and the effective Reynolds number of the tests was approximately 2,760,000. (Effective Reynolds number = Test Reynolds number x Turbulence factor. For the Langley 4-by-6 foot vertical tunnel, the turbulence factor was 1.93.)

The CAD model was generated in SolidWorks and then imported in STAR-CCM+ (Figure 45 and Figure 46).

Mesh data are available in Table 5 and shown from Figure 47 to Figure 52 for two different flap deflections (0 and 30 degrees). CFD analyses show good agreement with the result of ref. [29] and [30], except at high flow separation, as expected (see Section 3.1). The pressure coefficient distribution for both cases is shown from Figure 53 to Figure 56, using the same scale in order to make a proper comparison.

Results in terms of aerodynamic lift and hinge moment coefficient (C_L and C_H) are shown in Figure 57 and Figure 58, where a comparison is made between the results achieved through CFD analyses with STAR-CCM+ and those presented in [29] and [30].

From the charts, it is apparent the validity of the mesh and of the physics model involved, as the configurations at small angles of attack and rudder deflections are well simulated by the CFD.

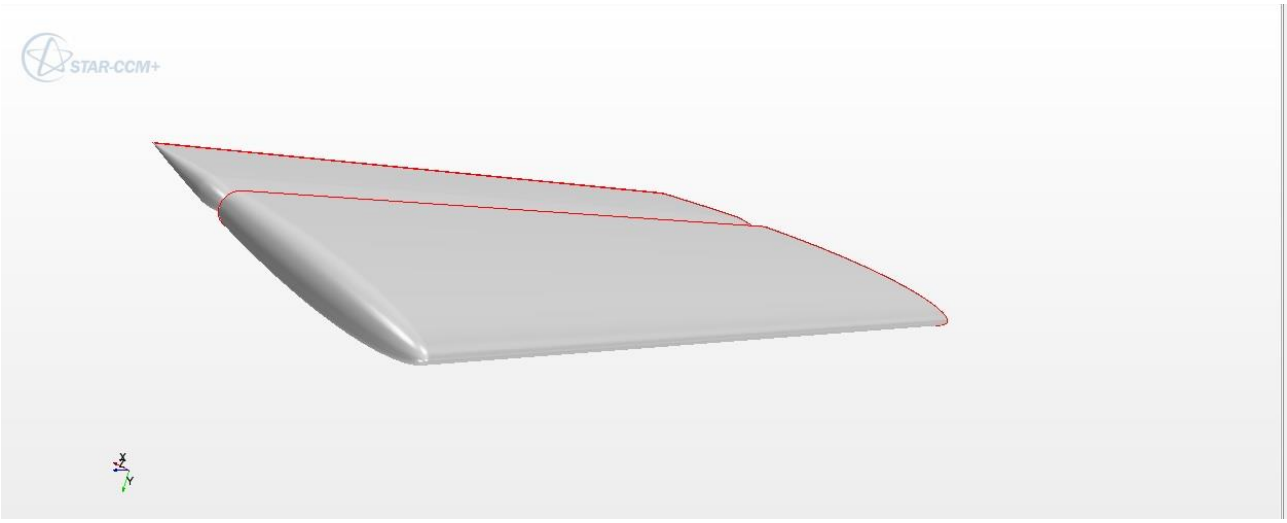

Figure 45: Test case geometry generated in STAR-CCM+.

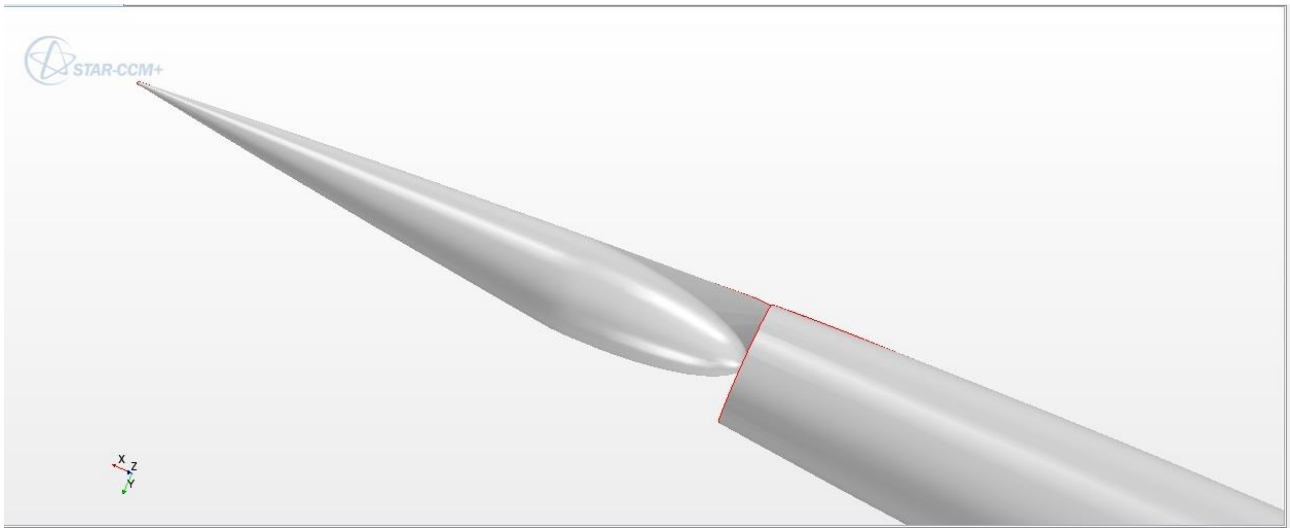

Figure 46: Detail of geometry, flap leading edge, STAR-CCM+.

Mesh type	Polyhedral cells (see Figure 50)
Base size	1.0 m
Number of prism layers	20
Prism Layer Stretching	1.1
Mesh size (in percentage of the base size)	Target (1), Minimum (0.1)
Numbers of cells	≅ 1 000 000

Angle of attack, α	From -20 to 20 degrees
Reynolds Number, Re	1 430 000
Mach number, M	≅ 0.1
Flow regime	Fully turbulent (Spalart-Allmaras model)

Table 5: Mesh and physics data of NACA WRL 186 report.

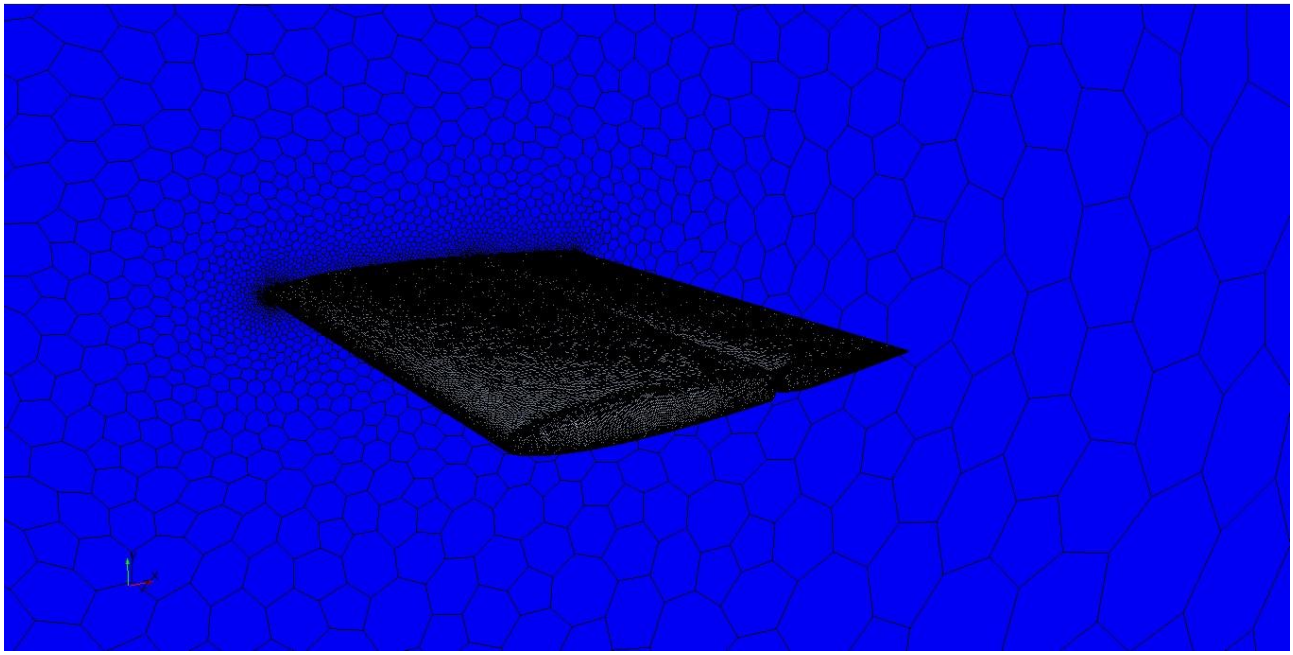

Figure 47: Volume mesh generated in STAR-CCM+, flap deflection equal to 0°.

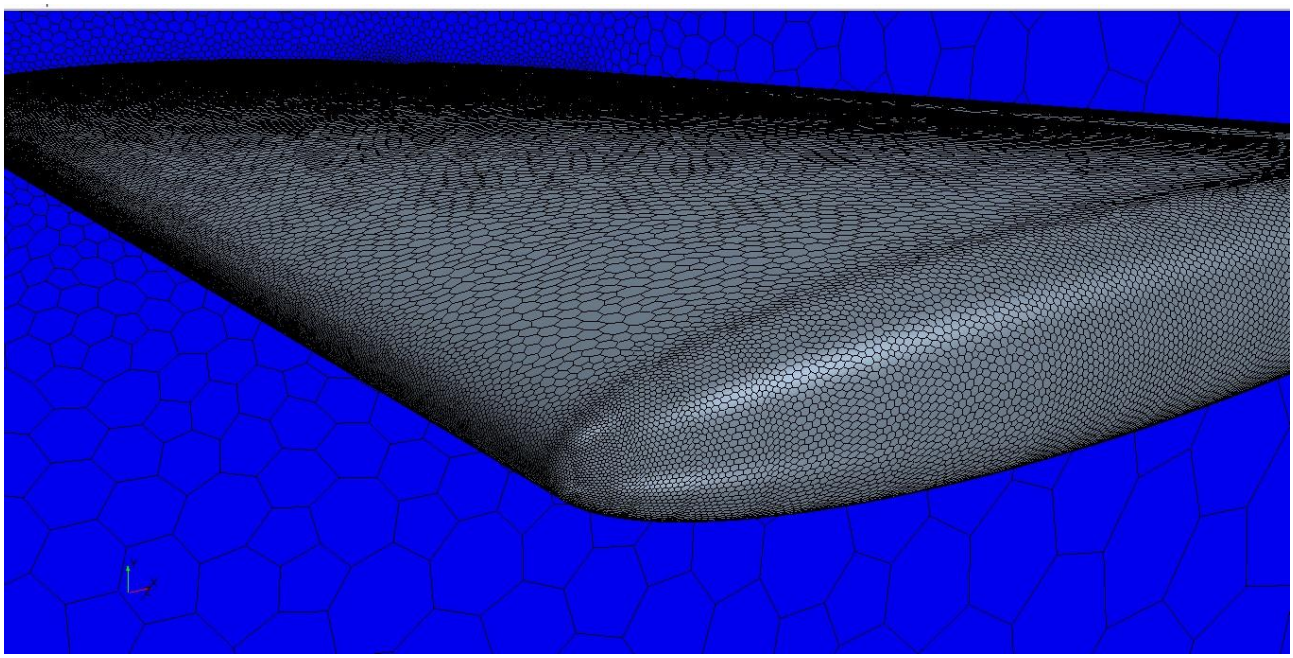

Figure 48: Detail of the volume mesh, fixed surface leading edge, flap deflection equal to 0°.

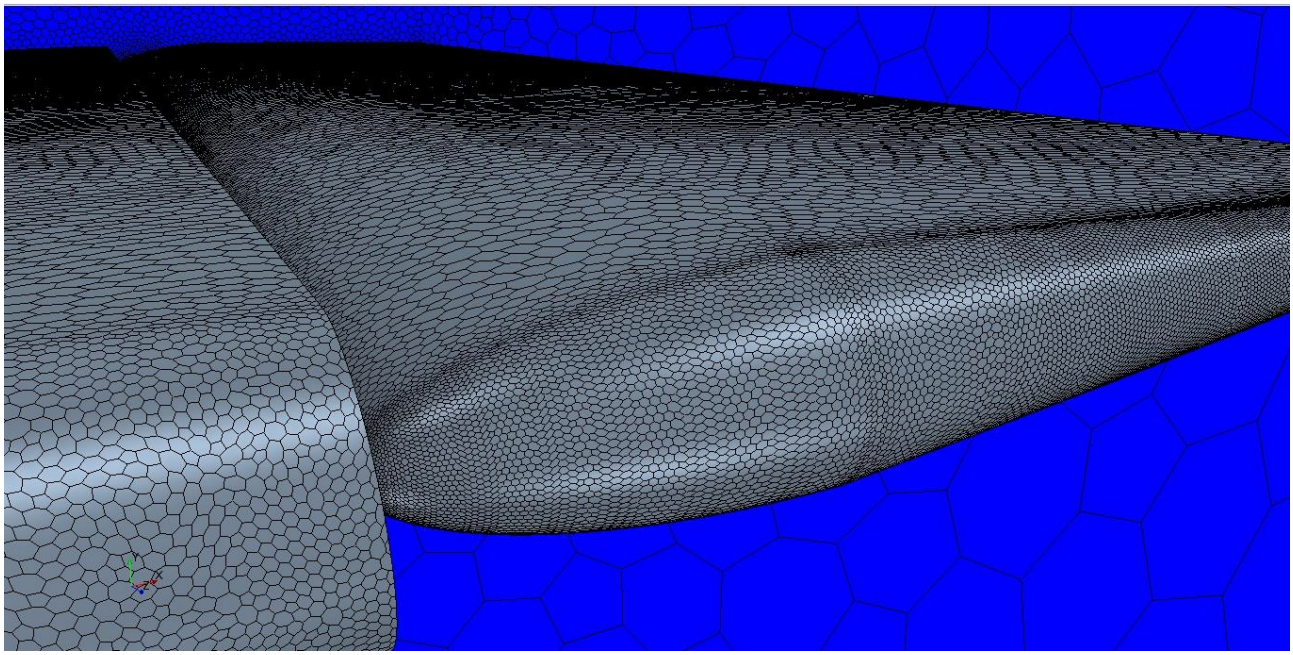

Figure 49: Detail of the volume mesh, flap leading edge, flap deflection equal to 0°.

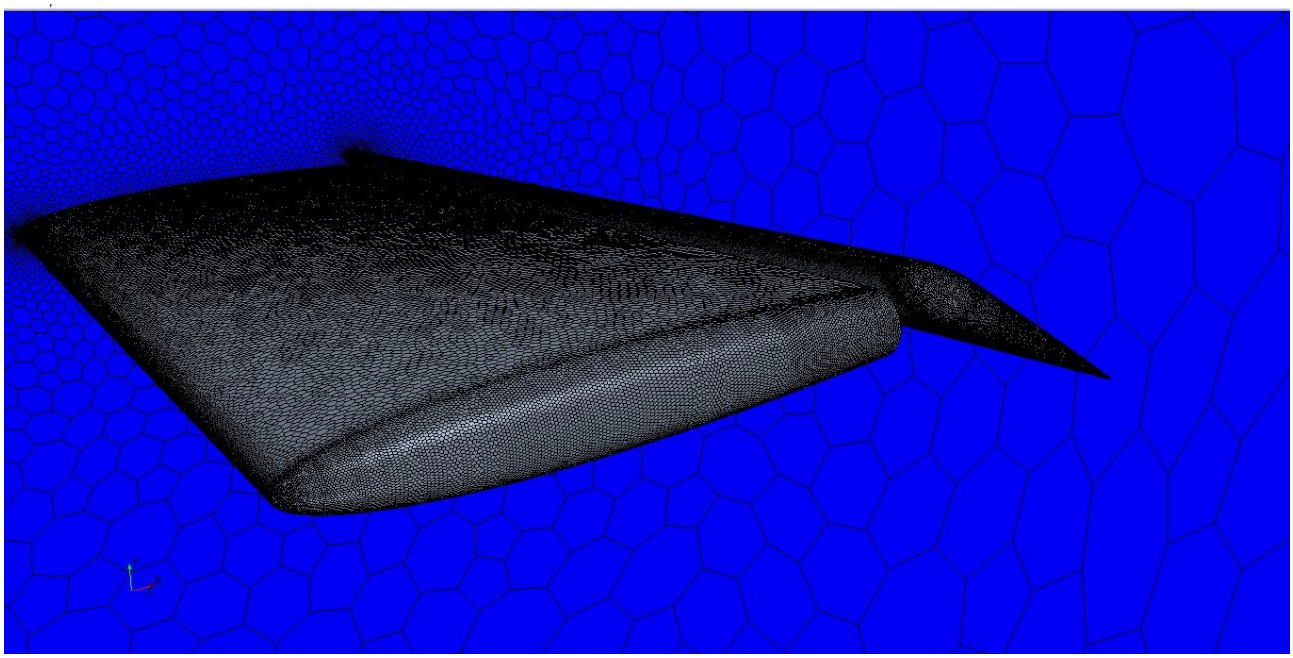

Figure 50: Volume mesh generated in STAR-CCM+, flap deflection equal to 30°.

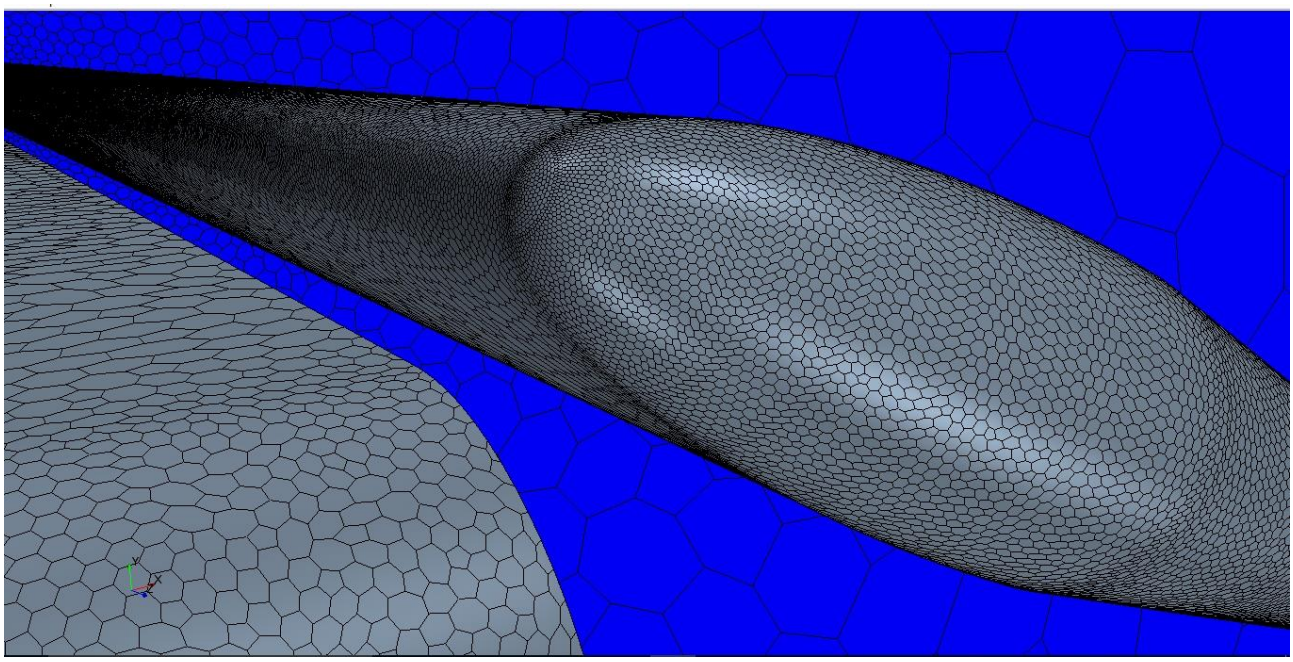

Figure 51: Detail of the volume mesh, flap leading edge, flap deflection equal to 30°.

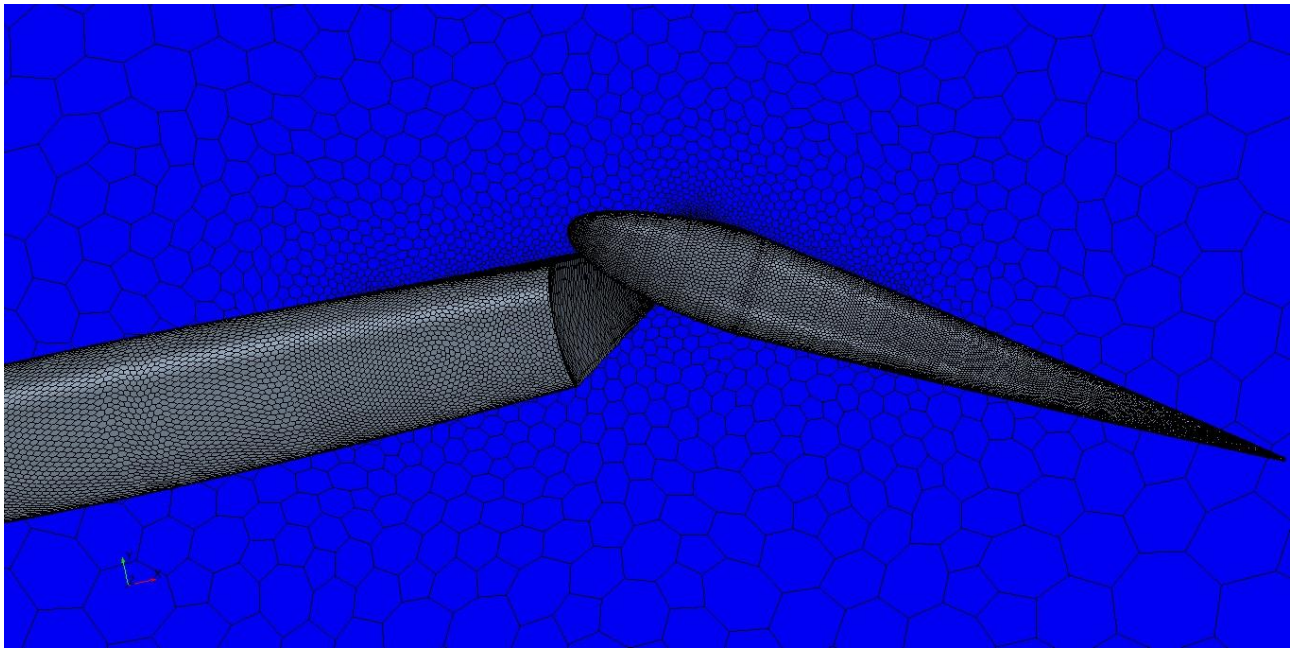

Figure 52: Detail of the volume mesh, flap leading edge, flap deflection equal to 30°.

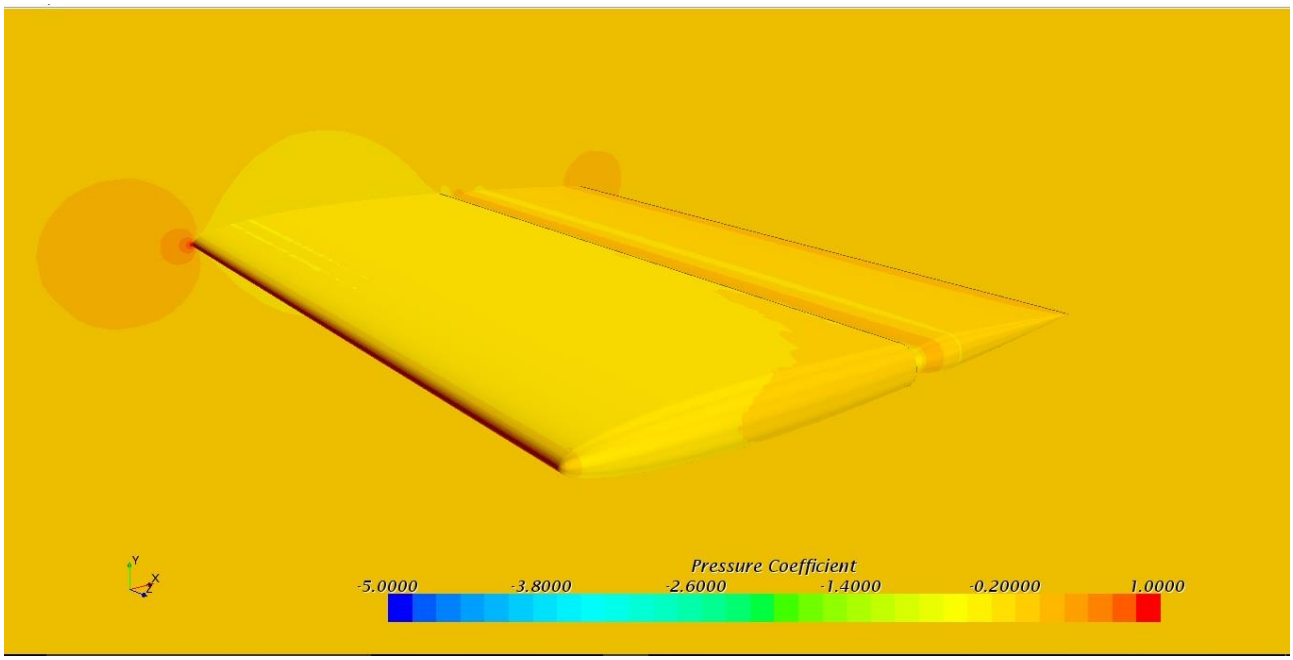

Figure 53: Pressure coefficient distribution, flap deflection equal to 0°.

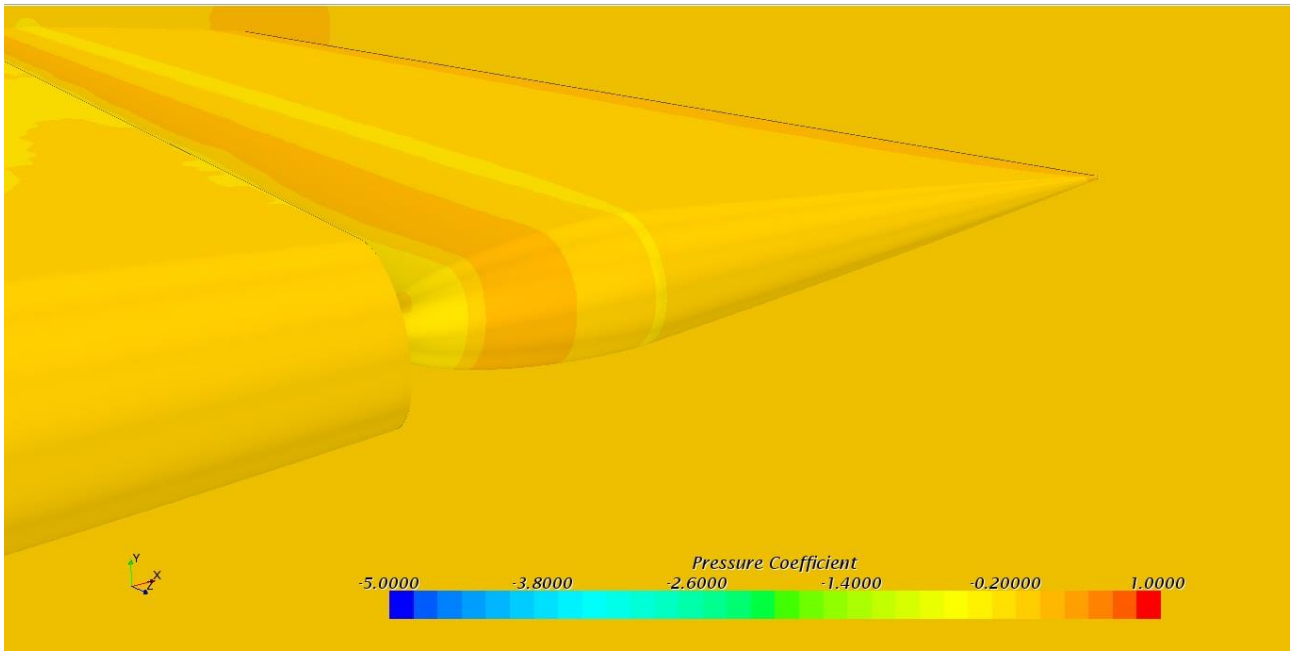

Figure 54: Pressure coefficient distribution on flap leading edge, flap deflection equal to 0°.

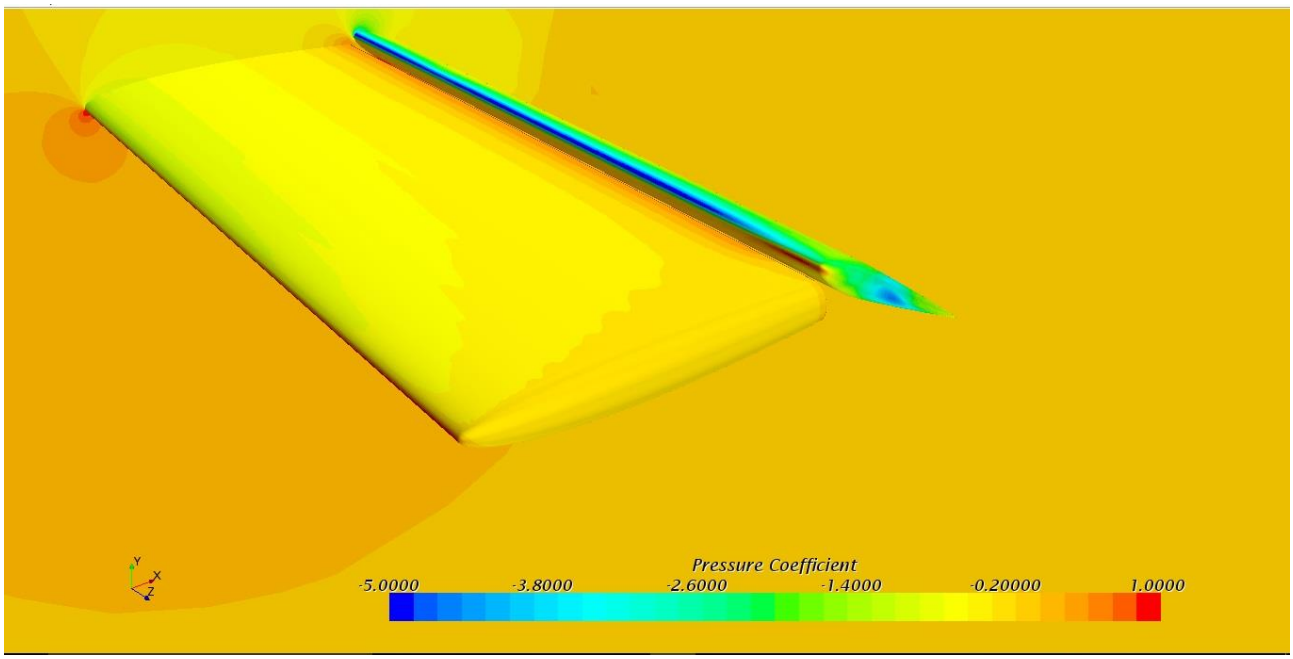

Figure 55: Pressure coefficient distribution, flap deflection equal to 30°.

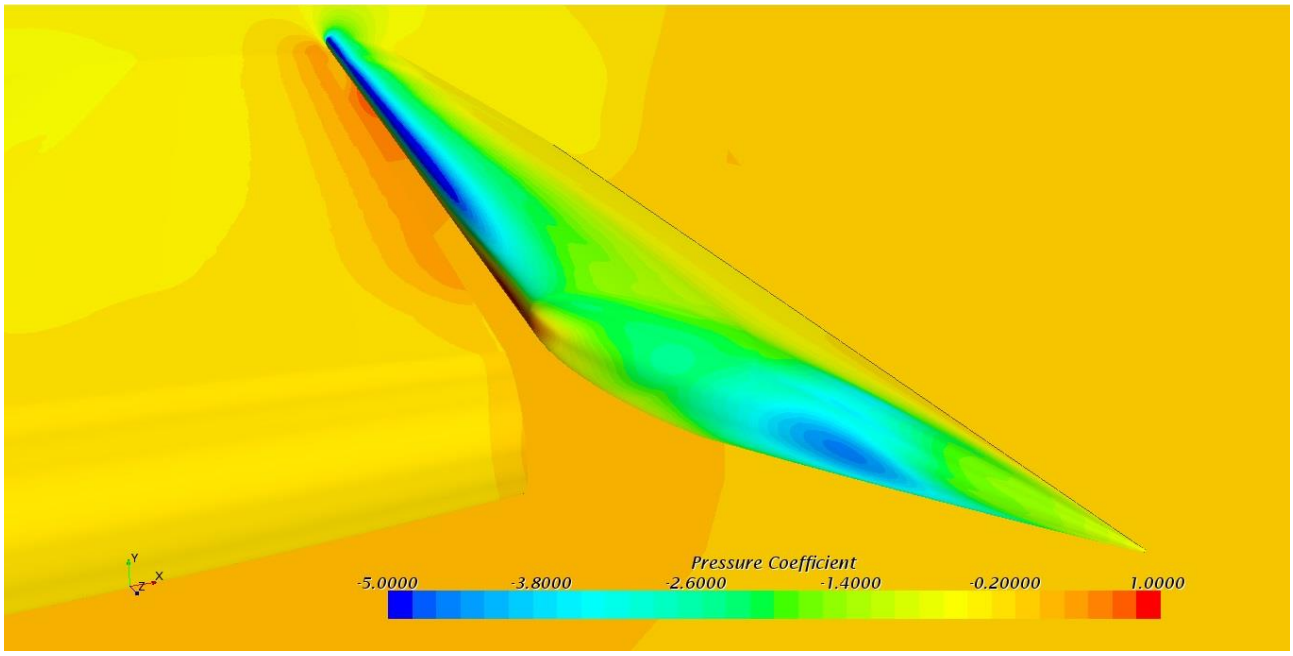

Figure 56: Pressure coefficient distribution on flap leading edge, flap deflection equal to 30°.

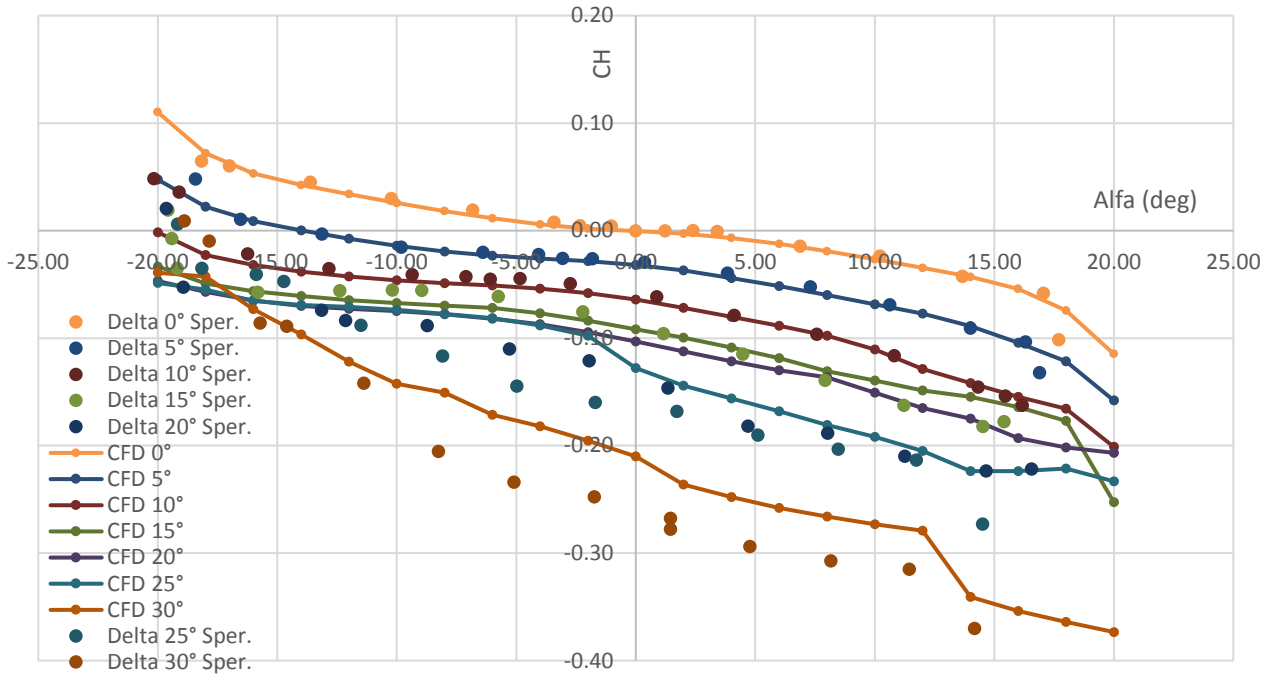

Figure 57: C_H vs α curves comparison between numerical (continuous lines) and experimental data (marked by points).

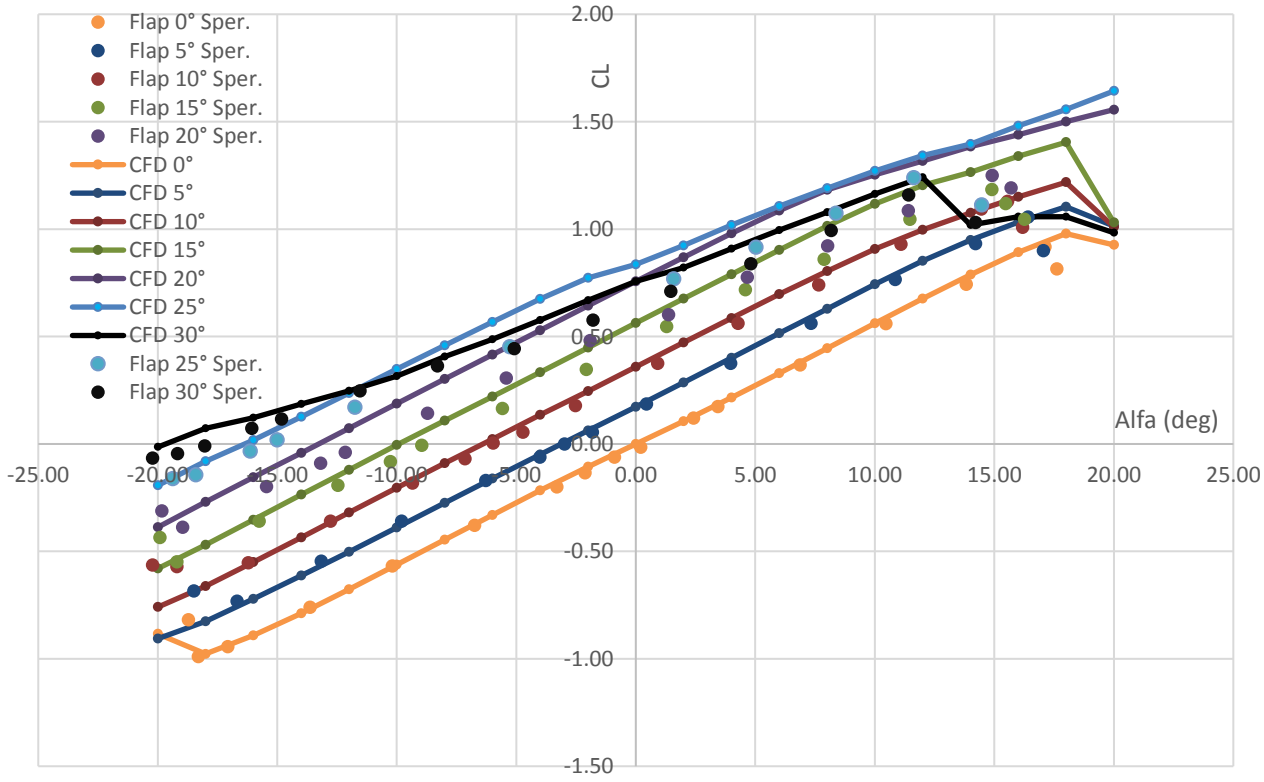

Figure 58: C_L vs α curves comparison between numerical (continuous lines) and experimental data (marked by points).

4 Creation of an Aerodynamic Database

4.1 Objectives and Analysis Matrix

The main objective of this chapter, and, in general, the present thesis work, was to build an aerodynamic database, in order to find a new method for the calculation of the rudder effectiveness τ_V, after numerous CFD analyses performed on different vertical tail planes geometries. The main objective of these analyses was to highlight any functional dependencies of the parameter τ_V by some geometrical characteristics of the vertical tail plane, such as the sweep angle or the taper ratio. In fact, as previously discussed in Chapter 2, these dependencies are not reported by the semi-empirical methods presented in the literature. The analysis matrix is reported in Table 6.

	PROFILO	cf/c	cb/cf	Gap	Nose Shape	Arv	Λv	λv2	bv	Sv	Eta Elevator
Geom.1	NACA 0012	0.3	0.15	0.5	Round	1.5	26.6	0.62	0.24	0.04	Full Span
Geom.2	NACA 0012	0.4	0.15	0.5	Round	1.5	26.6	0.62	0.24	0.04	Full Span
Geom.3	NACA 0012	0.4	0.15	0.5	Round	1.5	26.6	0.7	0.24	0.04	Full Span
Geom.4	NACA 0012	0.4	0.15	0.5	Round	1.5	26.6	0.9	0.24	0.04	Full Span
Geom.5	NACA 0012	0.3	0.15	0.5	Round	1.5	26.6	0.7	0.24	0.04	Full Span
Geom.6	NACA 0012	0.3	0.15	0.5	Round	1.5	26.6	0.9	0.24	0.04	Full Span
Geom.7	NACA 0012	0.5	0.15	0.5	Elliptical	1.5	26.6	0.62	0.24	0.04	Full Span
Geom.8	NACA 0012	0.5	0.15	0.5	Elliptical	1.5	26.6	0.7	0.24	0.04	Full Span
Geom.9	NACA 0012	0.5	0.15	0.5	Elliptical	1.5	26.6	0.9	0.24	0.04	Full Span
Geom.10	NACA 0012	0.3	0.15	0.5	Round	1.5	20	0.62	0.24	0.04	Full Span
Geom.11	NACA 0012	0.3	0.15	0.5	Round	1.5	20	0.7	0.24	0.04	Full Span
Geom.12	NACA 0012	0.3	0.15	0.5	Round	1.5	20	0.9	0.24	0.04	Full Span
Geom.13	NACA 0012	0.4	0.15	0.5	Round	1.5	20	0.62	0.24	0.04	Full Span
Geom.14	NACA 0012	0.4	0.15	0.5	Round	1.5	20	0.7	0.24	0.04	Full Span
Geom.15	NACA 0012	0.4	0.15	0.5	Round	1.5	20	0.9	0.24	0.04	Full Span
Geom.16	NACA 0012	0.5	0.15	0.5	Elliptical	1.5	20	0.62	0.24	0.04	Full Span
Geom.17	NACA 0012	0.5	0.15	0.5	Elliptical	1.5	20	0.7	0.24	0.04	Full Span
Geom.18	NACA 0012	0.5	0.15	0.5	Elliptical	1.5	20	0.9	0.24	0.04	Full Span
Geom.19	NACA 0012	0.3	0.15	0.5	Round	1.5	26.6	0.62	0.24	0.04	0.9
Geom.20	NACA 0012	0.3	0.15	0.5	Round	1.5	26.6	0.7	0.24	0.04	0.9
Geom.21	NACA 0012	0.3	0.15	0.5	Round	1.5	26.6	0.9	0.24	0.04	0.9
Geom.22	NACA 0012	0.4	0.15	0.5	Round	1.5	26.6	0.62	0.24	0.04	0.9
Geom.23	NACA 0012	0.4	0.15	0.5	Round	1.5	26.6	0.7	0.24	0.04	0.9
Geom.24	NACA 0012	0.4	0.15	0.5	Round	1.5	26.6	0.9	0.24	0.04	0.9
Geom.25	NACA 0012	0.5	0.15	0.5	Elliptical	1.5	26.6	0.62	0.24	0.04	0.9
Geom.26	NACA 0012	0.5	0.15	0.5	Elliptical	1.5	26.6	0.7	0.24	0.04	0.9
Geom.27	NACA 0012	0.5	0.15	0.5	Elliptical	1.5	26.6	0.9	0.24	0.04	0.9
Geom.28	NACA 0012	0.3	0.15	0.5	Round	1.5	20	0.62	0.24	0.04	0.9
Geom.29	NACA 0012	0.3	0.15	0.5	Round	1.5	20	0.7	0.24	0.04	0.9
Geom.30	NACA 0012	0.3	0.15	0.5	Round	1.5	20	0.9	0.24	0.04	0.9
Geom.31	NACA 0012	0.4	0.15	0.5	Round	1.5	20	0.62	0.24	0.04	0.9
Geom.32	NACA 0012	0.4	0.15	0.5	Round	1.5	20	0.7	0.24	0.04	0.9
Geom.33	NACA 0012	0.4	0.15	0.5	Round	1.5	20	0.9	0.24	0.04	0.9
Geom.34	NACA 0012	0.5	0.15	0.5	Elliptical	1.5	20	0.62	0.24	0.04	0.9
Geom.35	NACA 0012	0.5	0.15	0.5	Elliptical	1.5	20	0.7	0.24	0.04	0.9
Geom.36	NACA 0012	0.5	0.15	0.5	Elliptical	1.5	20	0.9	0.24	0.04	0.9
Geom.37	NACA 0012	0.3	0.15	0.5	Elliptical	1.5	26.6	0.62	0.24	0.04	Full Span
Geom.38	NACA 0012	0.3	0.15	0.5	Medium	1.5	26.6	0.62	0.24	0.04	Full Span
Geom.39	NACA 0012	0.3	0.15	0.5	Round	1.5	30	0.62	0.24	0.04	Full Span
Geom.40	NACA 0012	0.3	0.15	0.5	Round	1.5	40	0.62	0.24	0.04	Full Span

Table 6: Analysis Matrix for the effectiveness prediction

In Table 6, $\frac{c_f}{c}$ is the ratio between the mobile surface's chord and that of the fixed surface, Λ_V is the sweep angle to the leading edge, λ_V is the taper ratio, AR_V the aspect ratio, η the extension of the mobile surface along the span, $\frac{c_b}{c_f}$ the overhang, b_V the vertical tail plane's span, S_V the vertical tail plane's surface. The balance ratio has been fixed to $0.15c_f$ and no horn balance has been considered. All simulations were performed using the STAR-CCM+ software and the results in terms of rudder effectiveness are presented in the following sections, along with details about the mesh type, the mesh sizes and the analyzed physical problem.

4.2 Description of the reference geometry

Among all the different analyzed geometries, presented in Table 6, it is possible to consider Geometry 1 as the reference geometry. The 3D CAD drawings have been realized such to be compatible with previous investigations carried out by the DAF research group, aimed to improve the accuracy of the preliminary phase of aircraft design. Precisely for this reason, the size ($c_{root} = 0.2m$, in addition to the data reported in Table 6) and the geometric characteristics of the first geometry (Geometry 1) are the same of the vertical tail plane analyzed in [13], [26] and [33].

Most of the geometries subjected to analysis have been realized with a MATLAB code, which from the input data as chords ratio, overhang, moveable part's hinge position and nose shape, returned the coordinates of all the points belonging to the root profile (both fixed and mobile part) of the desired vertical tail plane. Suitably working these coordinates in Excel, it was then possible to easily import the root and the tip profiles of many geometries into a CAD software, obtaining the desired three-dimensional geometries by means of a loft between two sections.

It is important to note, observing the different geometries analyzed, that, to maintain a constant aspect ratio ($AR = 1.5$) and planform area S_V, a proper scaling has been necessary, reducing the dimensions of the root and tip airfoils with the increasing of the taper ratio, λ_V.

In particular, as regards to Geometry 1, whereas the span b_V was equal to ≅0.243 m, the taper ratio ($\lambda = \frac{c_{tip}}{c_{root}}$) was equal to 0.62, the root chord was equal to 0.2 m and the tip chord, according to the taper ratio, was equal to 0.124 m, and for which the planform was a trapezoid, from the area calculation (sum of the surface of both fixed and movable part) with the following formula

$$S_{V,1} = \frac{\left(c_{tip} + c_{root}\right) \cdot b_V}{2} \qquad (4.1)$$

was found a value of $S_{V,1} \cong 0.04m^2$. The definitions of all the parameters of interest are provided in Figure 59, in which is shown the planform of the reference geometry.

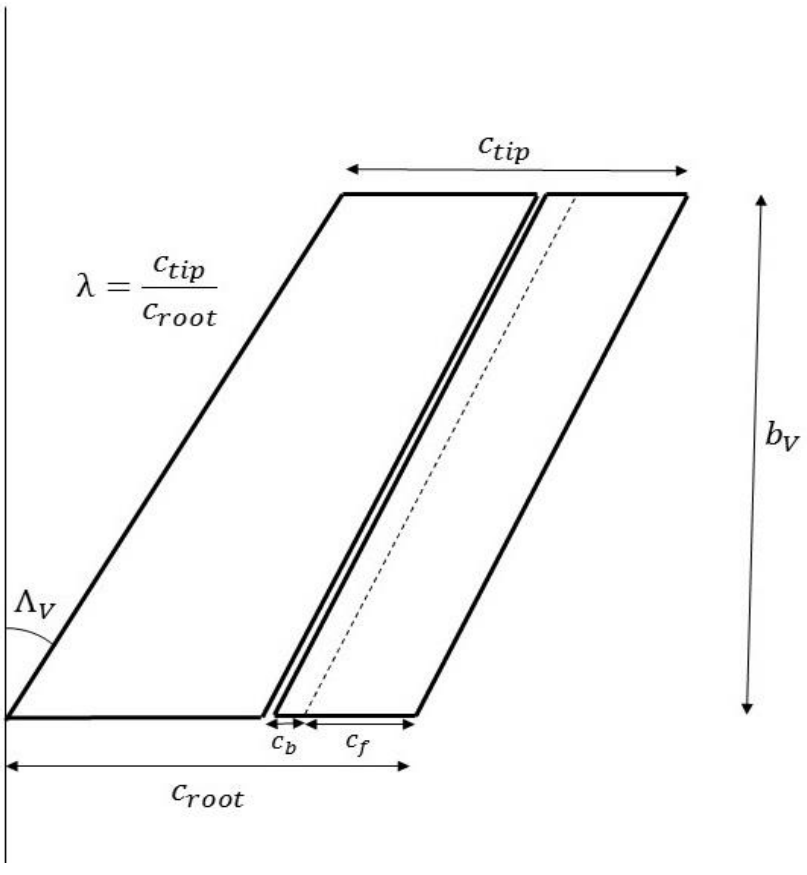

Figure 59: Definition of the most important geometrical parameters.

With the increasing of the taper ratio, the tip profile's chord (c_{tip}) increases in length, and therefore, applying the formula (4.1) to find the total area, the result was necessarily increased (considering

that the span b_V had been set equal to 0.243m, constant for all geometries) due to the increase in c_{tip}. This situation could not therefore lead to maintain a constant aspect ratio for all the geometries with taper ratio greater than 0.62.

It was thus necessary to scale the chords of the root and the tip profiles to a value equal to the surfaces ratio ($\frac{S_{V,1}}{S_{V,2}}$), where $S_{V,2}$ was the total area of the reference geometries with taper ratio equal to 0.7 and 0.9. This ratio was equal to $\frac{S_{V,1}}{S_{V,2}} = 0.9529$ for all the geometries with 0.7 as taper ratio, while, for the geometries with taper ratio equal to 0.9, it was necessary to scale for $\frac{S_{V,1}}{S_{V,2}} = 0.854$. This scaling assured that the planform area and aspect ratio were constant at different taper ratios. It is important to note that there is no influence, on the total area's calculation, of other vertical plane's geometric parameters, such as the sweep angle or chords ratio.

The reference geometry for the calculation of $S_{V,1}$, which is the Geometry 1, is represented in Figure 60, while the reference geometries (Geometry number 5 and 6) for $S_{V,2}$ calculation are represented in Figure 61 and Figure 62.

Lastly, from Figure 63 to Figure 68 are represented all the various geometries that differ by only one geometrical parameter, such as the sweep angle Λ_V (equal to 20 degrees for Geometry 10, represented in Figure 65), the chords ratio $\frac{c_f}{c}$ (equal to 0.4 for Geometry 2, represented in Figure 63, and equal to 0.5 for Geometry 7, represented in Figure 64), the rudder extension along the span η (rudder extended up to 90% of the span for Geometry 19, represented in Figure 66) and the nose shape of the control surface (elliptical nose and medium nose, Figure 67 and Figure 68, related respectively to Geometry 37 and 38).

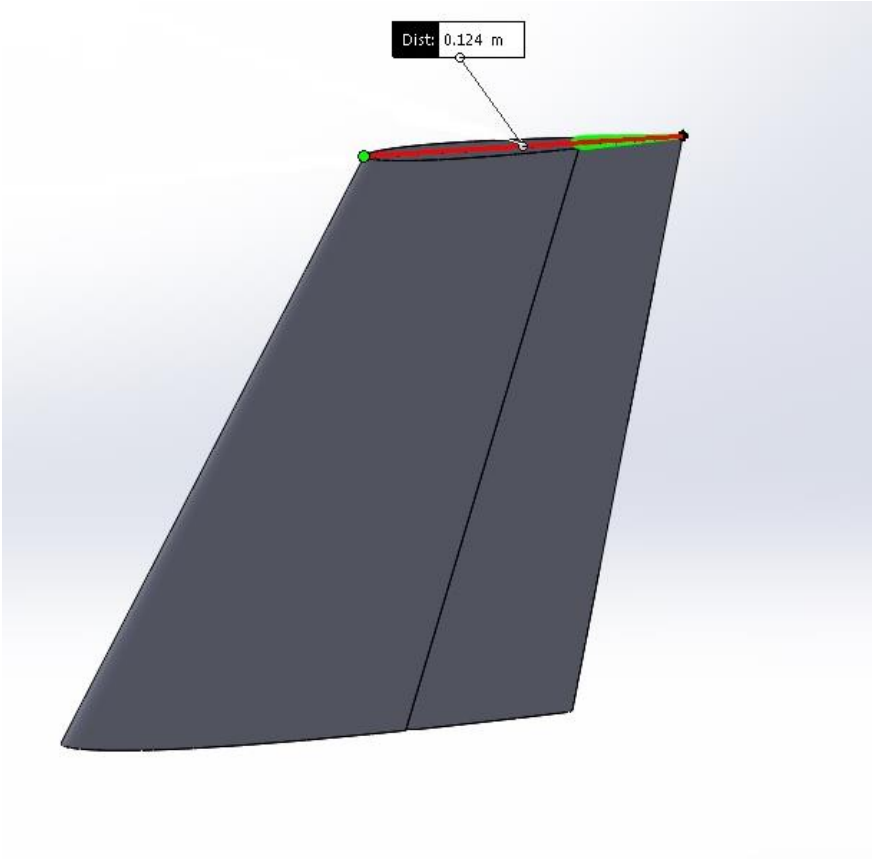

Figure 60: Geometry 1 with tip chord's length.

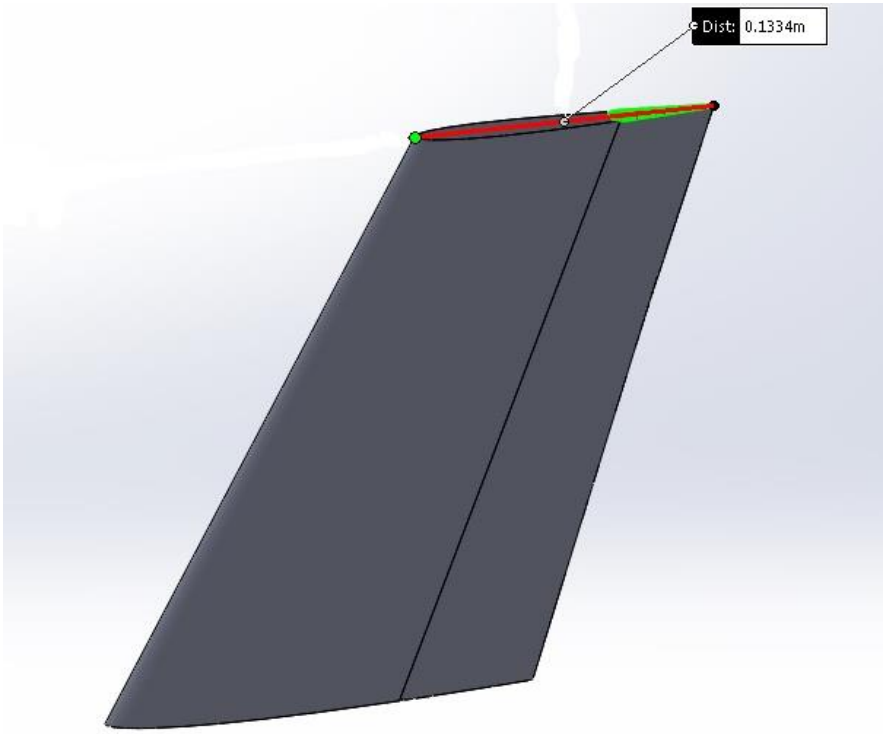

Figure 61: Geometry 5 with tip chord's length.

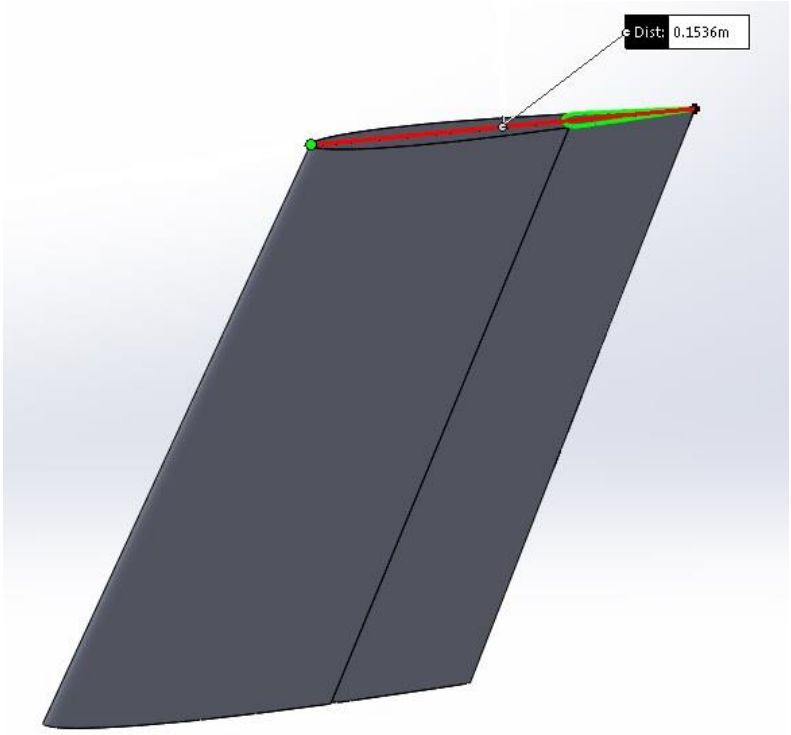

Figure 62: Geometry 6 with tip chord's length.

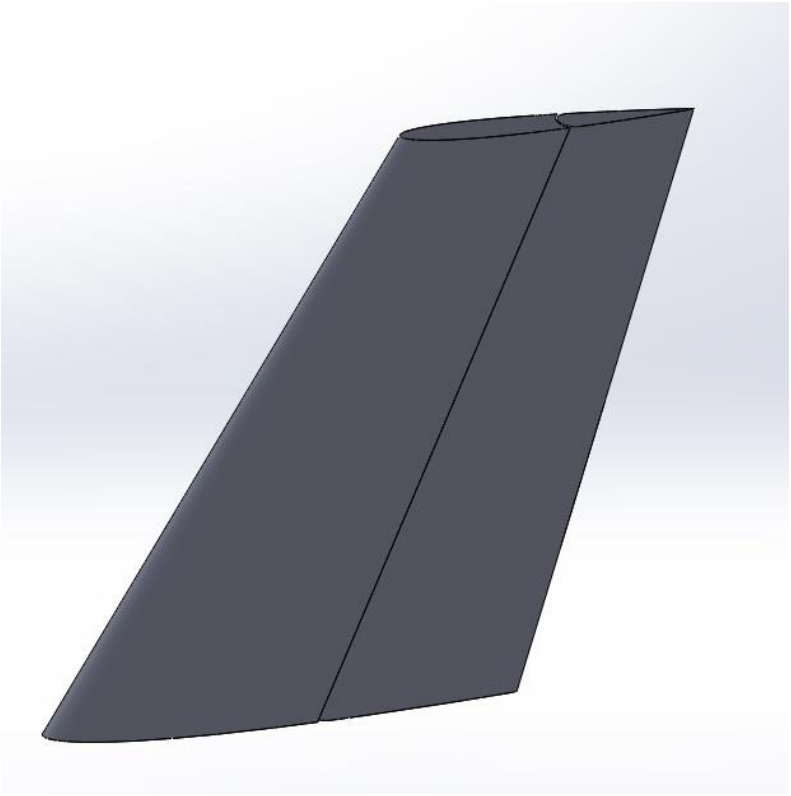

Figure 63: Geometry 2.

Figure 64: Geometry 7.

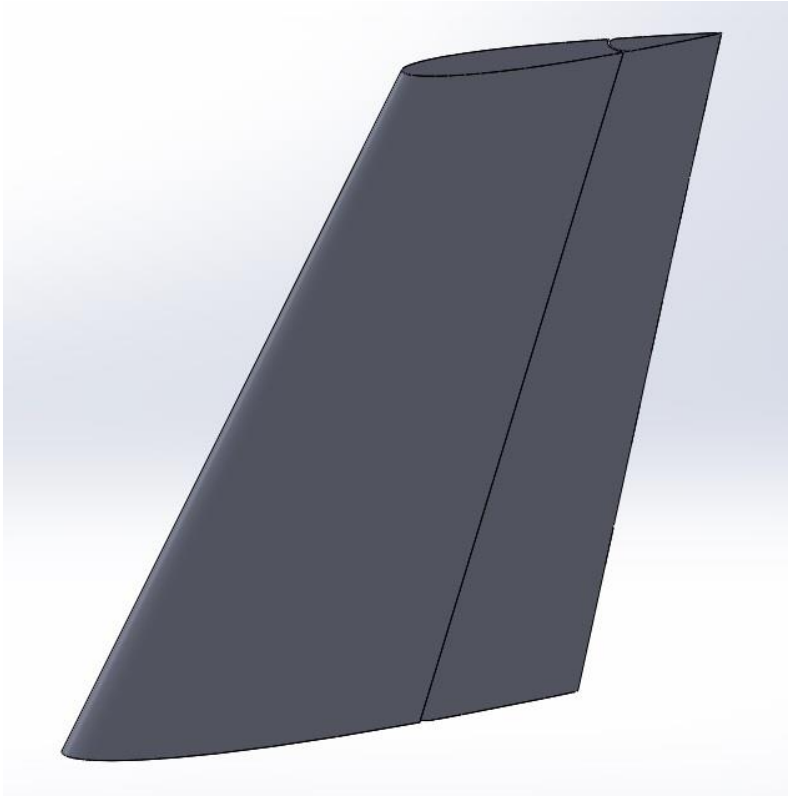

Figure 65: Geometry 10.

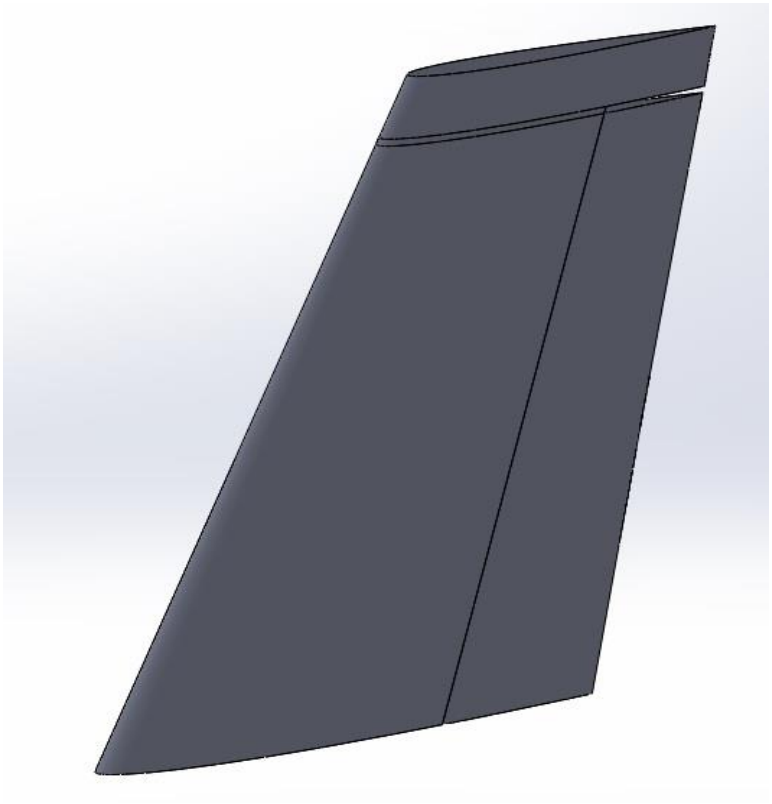

Figure 66: Geometry 19.

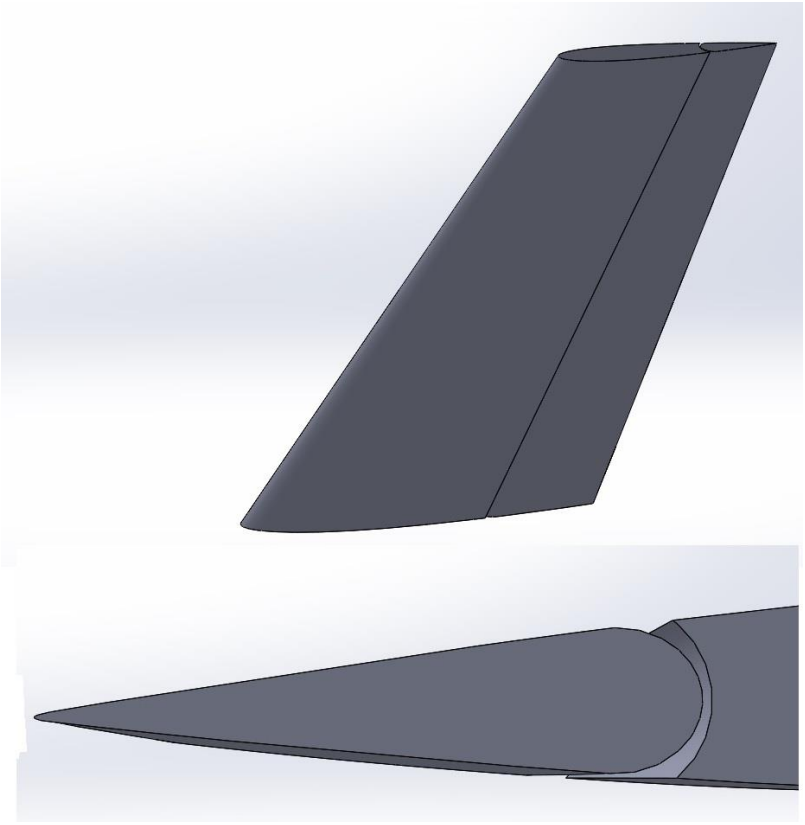

Figure 67: Geometry 37 with zoom on the elliptical nose.

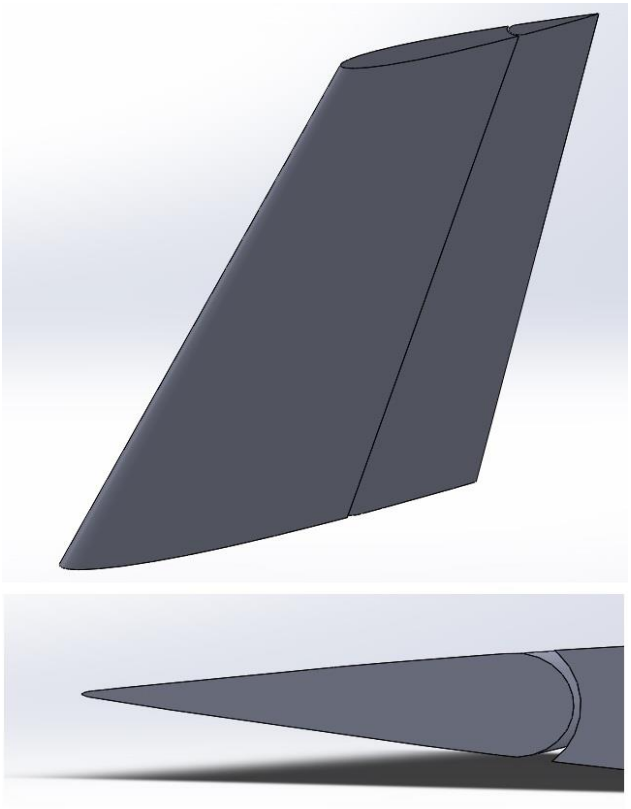

Figure 68: Geometry 38 with zoom on the medium nose.

After generating the CAD models, they were imported in STAR-CCM+ to proceed with the numerical analyses. In addition to the mesh generation, the details of which are presented in the next section, through the use STAR-CCM+ has been possible to rotate the rudder about his hinge axis, getting all the simulation files needed for the analyses, also thanks to the help of an Excel spreadsheet which provided the origin position of the hinge and the direction cosines for each geometry (after giving in input some geometrical parameters, such as the sweep angle to the leading edge and the trailing edge, the chords ratio, the overhang and the chord length of both fixed and mobile part). Some simulation files for the reference geometry (Geometry 1) are shown from Figure 69 to Figure 71.

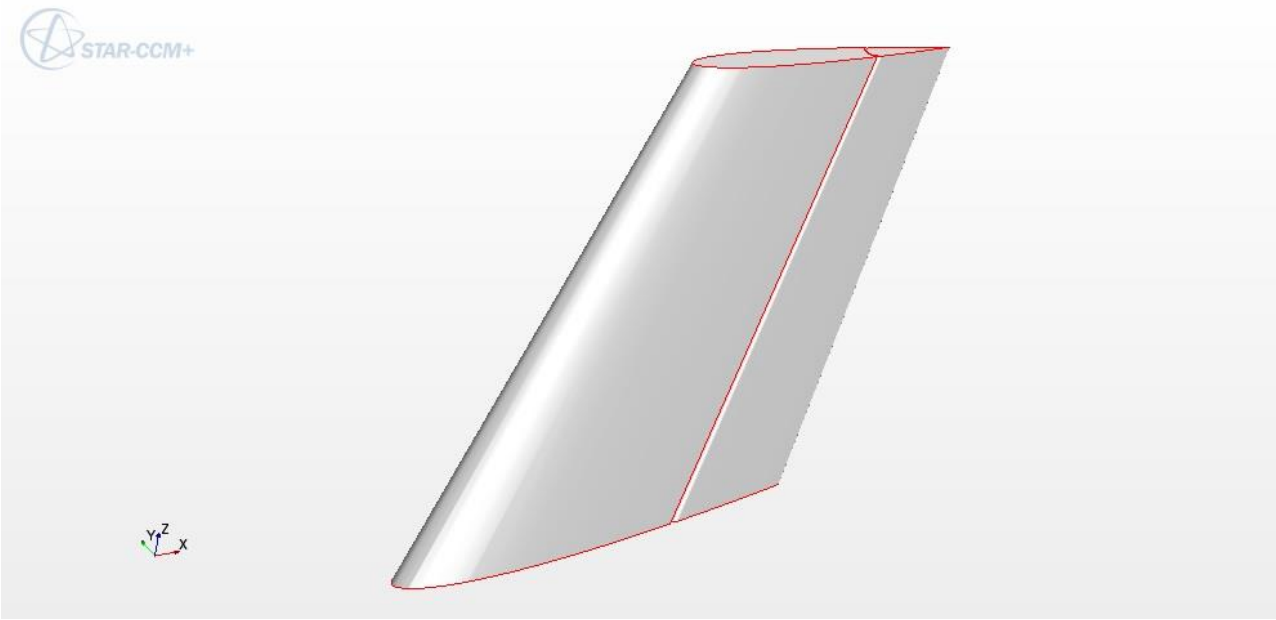

Figure 69: Reference geometry imported in STAR-CCM+, $\delta_r = 0°$.

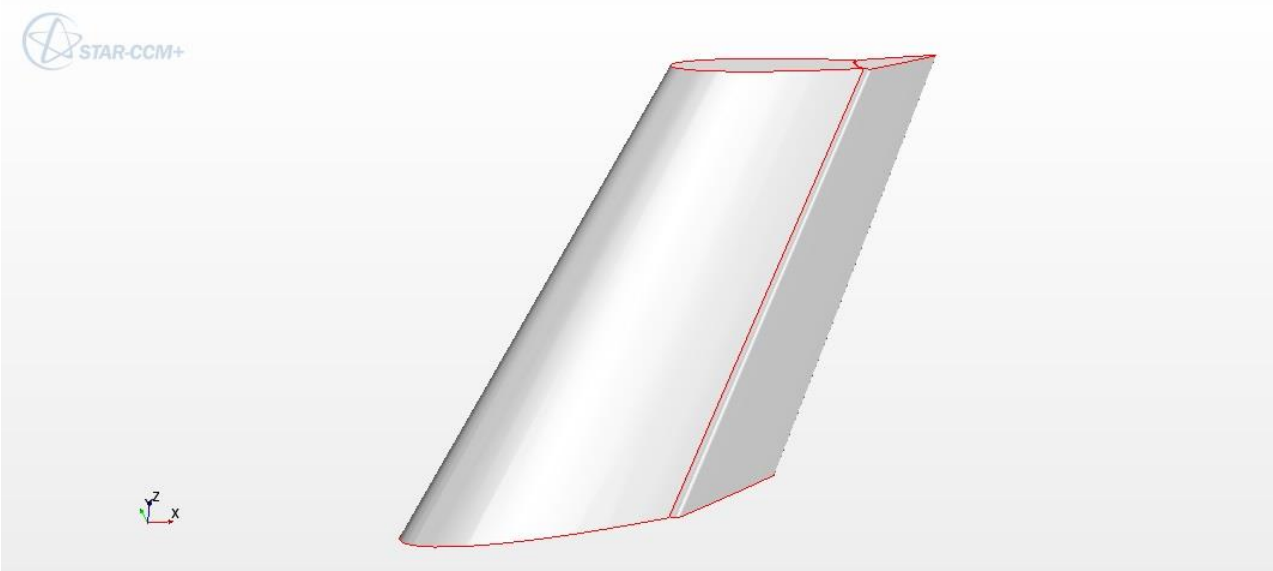

Figure 70: Reference geometry imported in STAR-CCM+, $\delta_r = 15°$.

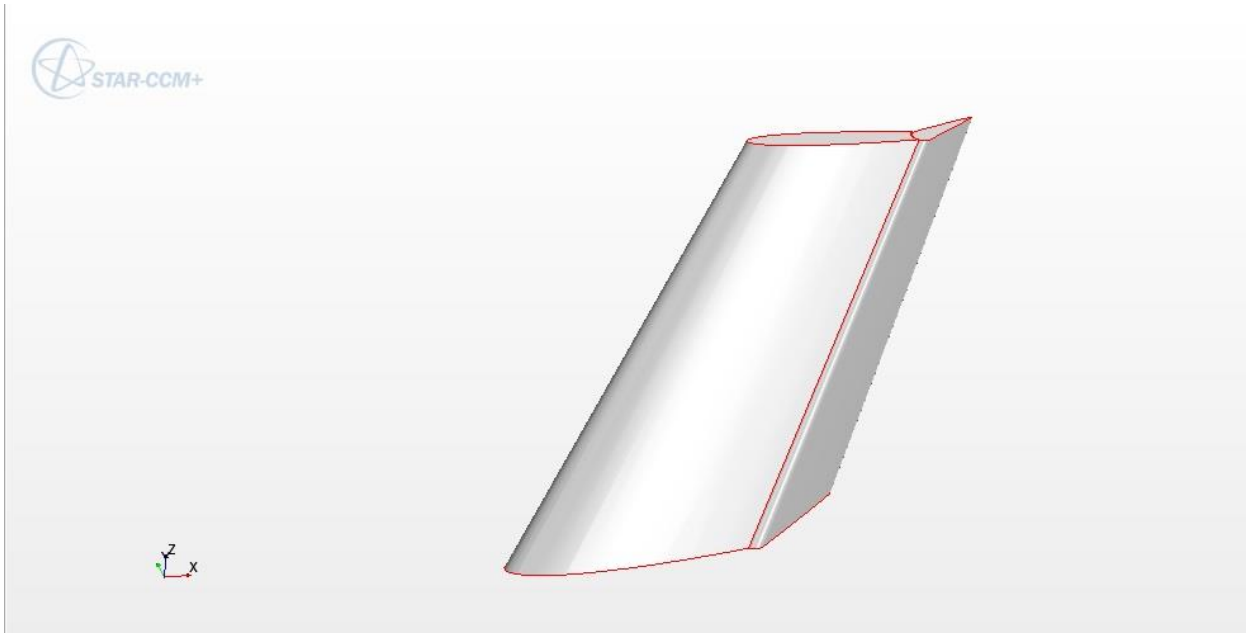

Figure 71: Reference geometry imported in STAR-CCM+, $\delta_r = 30°$.

4.3 Mesh and Physics Details

All the details on the utilized mesh are reported in

Table 7.

Mesh type	Polyhedral cells
Base size	0.5 m
Number of prism layers	20
Prism Layer Stretching	1.1
Mesh size (in percentage of the base size)	Target (1), Minimum (0.1)
Numbers of cells	From ≅ 4 700 000 to ≅ 6 600 000

Angle of sideslip, β	From -20 to 20 degrees
Reynolds Number, Re	1 100 000
Mach number, M	≅ 0.25
Flow regime	Fully turbulent (Spalart-Allmaras model)

Table 7: Details of the mesh used for the analyses.

For all the simulations, it was chosen a polyhedral mesh to better capture the phenomenon of interest, following the instructions given in Chapter 3. The base size has been set equal to 0.5 meters after observing the results, in terms of convergence of aerodynamic coefficients, downstream several simulations performed with different measures of the base size. As it can be seen in Figure 72, the values of the aerodynamic derivatives tended to convergence for a number of cells between 4 and 5 million. A base size of 0.5 m ensured a minimum number of cells equal to 4.7

million, thus justifying the use of this value. To obtain this number of cells, in addition to the base size (with which was substantially discretized the fluid domain around the vertical tail plane), customized controls have also been introduced on the rudder, on the fixed surface (main) and on its backside (main back). In particular, such controls, reported in Table 8, were related to the target size and the minimum size, both expressed as a percentage of the base size. In addition, only for the backside of the main surface, the generation of prism layers was disabled, neglecting the boundary layer in this area.

Prism Layers	Enabled (use parent values)
Mesh size (in percentage of the base size)	Target (0.2), Minimum (0.05)

Rudder and Main surface

Prism Layer Stretching	Disabled
Mesh size (in percentage of the base size)	Target (0.2), Minimum (0.05)

Main Back

Table 8: Custom controls.

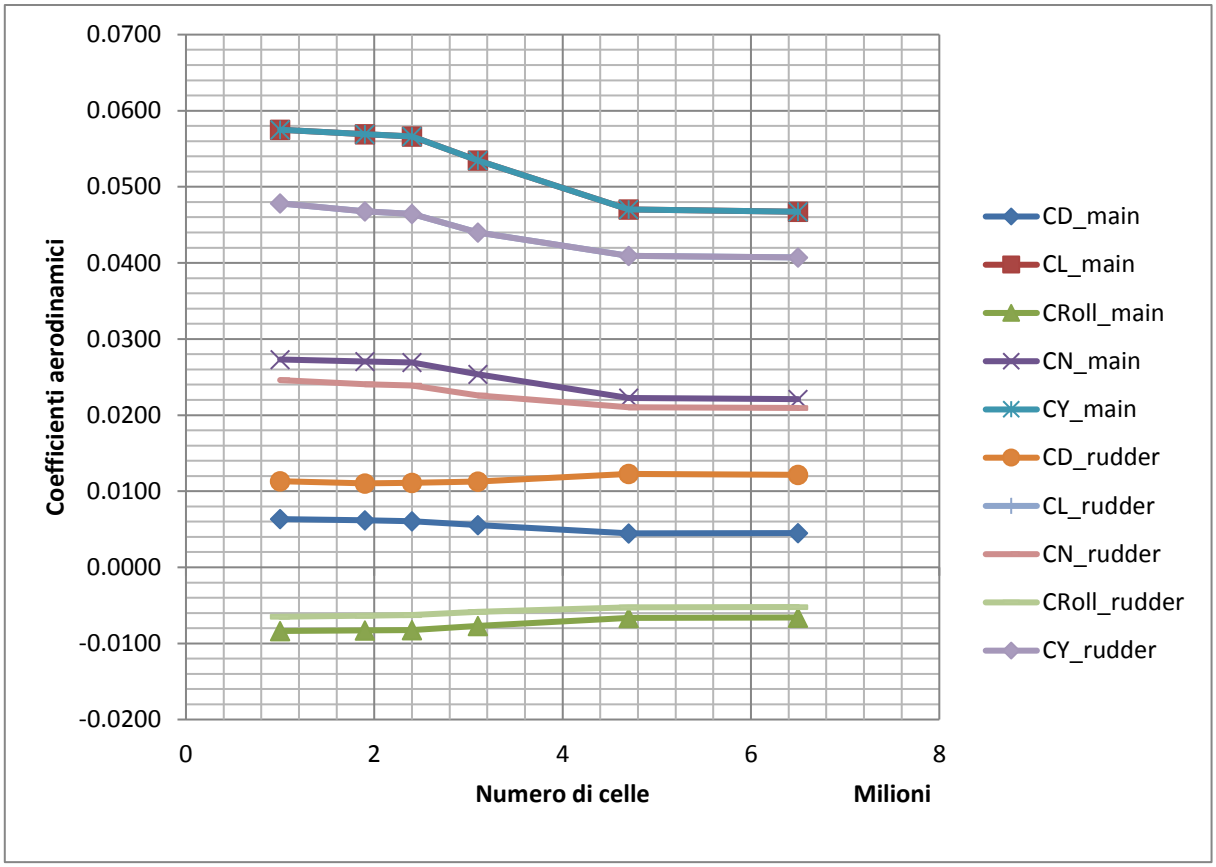

Figure 72: Aerodynamic coefficients trend as a function of the number of cells.

The physical model used, as usual, was the turbulent flow (stationary, three-dimensional, segregated) proposed by Spalart-Allmaras. The density of the gas (air) was constant (incompressible fluid) and set equal to $\rho = 1.225\ kg/m^3$, while the dynamic viscosity was set equal to $1.85 \cdot 10^{-5}\ Pa - s$. As reference pressure was chosen the atmospheric pressure (P_0 = 101325 Pa), while the initial conditions are presented in Table 9.

Pressure	0 Pa
Turbulence Viscosity Ratio	5.0
Velocity (magnitude and direction)	[83.0, 0.0, 0.0] m/s

Table 9: Initial Conditions for all the performed simulations.

The result of all the choices made is shown in the following figures (from Figure 73 to Figure 78), in which it is possible to see the calculation grid for the reference geometry (Geometry 1). The Navier-Stokes equations, averaged by Reynolds (RANS), were then solved for each cell of the fluid domain, for all the different deflections of the rudder (δ_r) and the different sideslip angles (β).

Figure 73: Computational grid for Geometry 1, $\delta_r = 0°$.

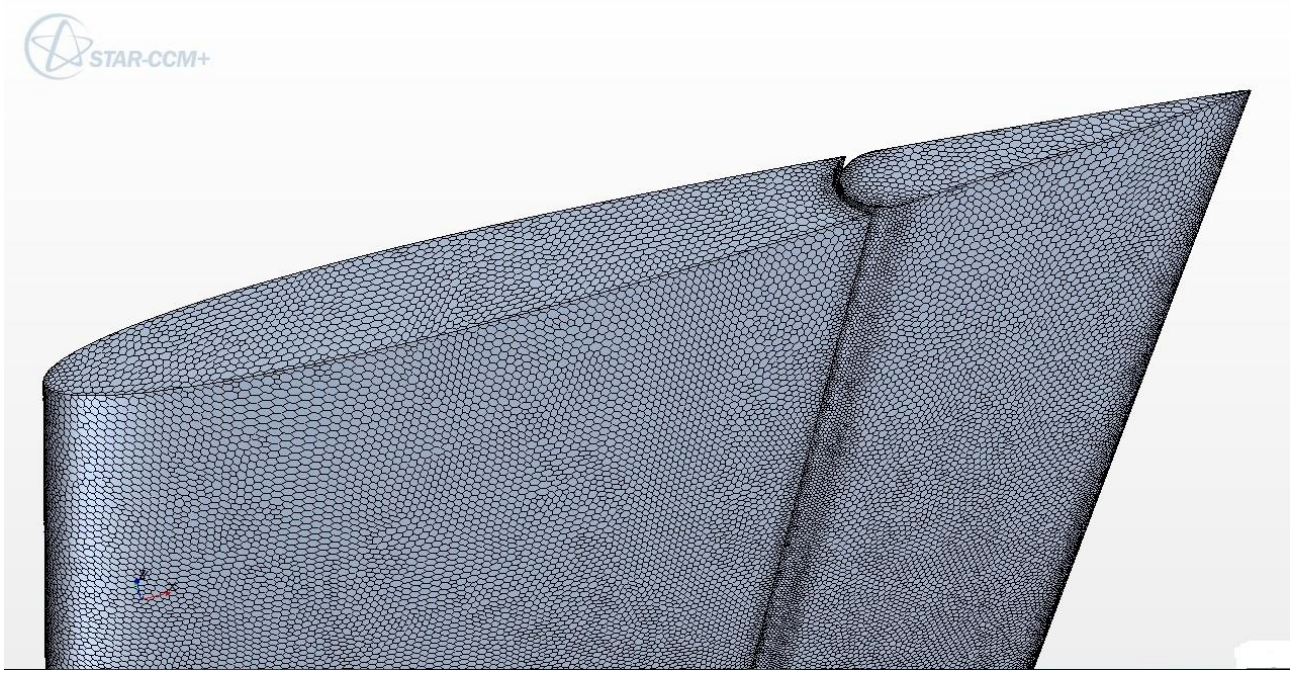

Figure 74: Detail of the computational grid for Geometry 1, $\delta_r = 0°$.

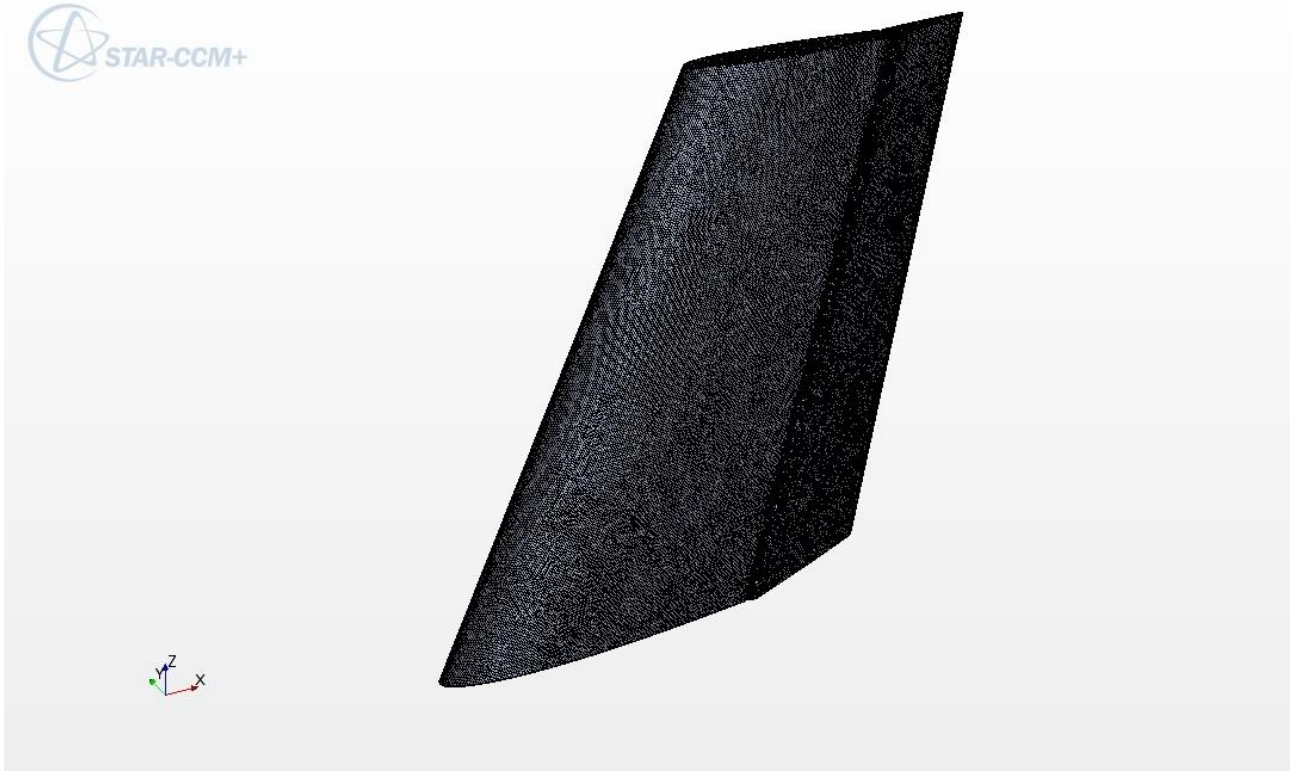

Figure 75: Computational grid for Geometry 1, $\delta_r = 15°$.

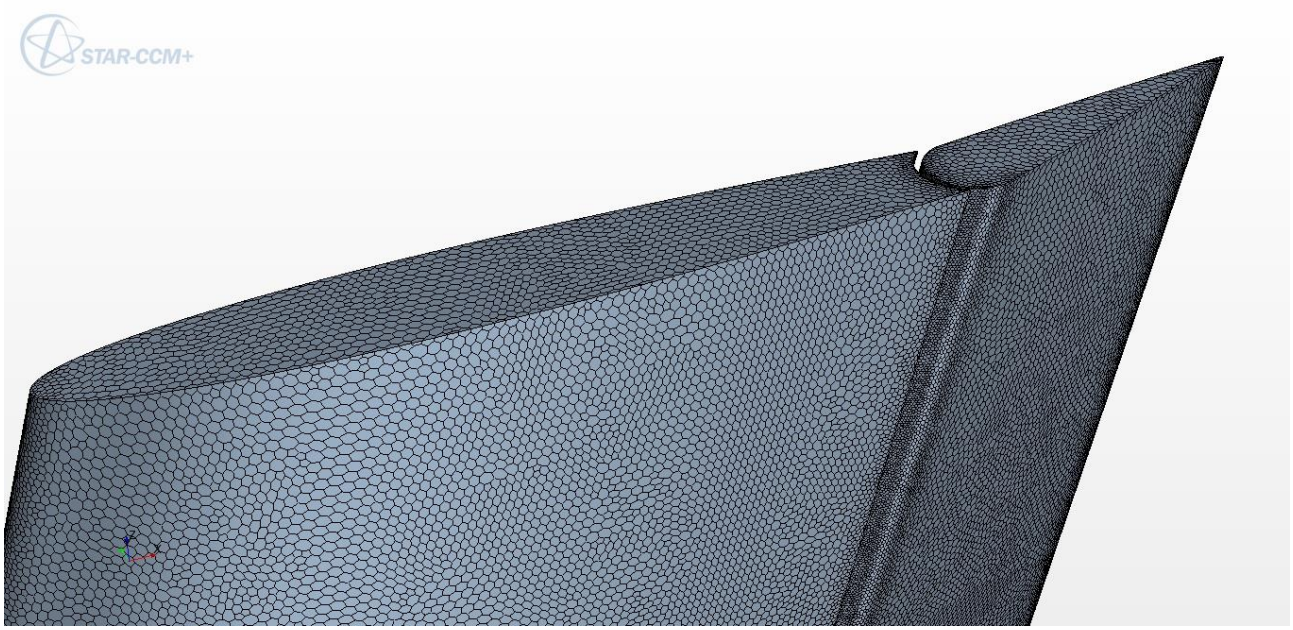

Figure 76: Detail of the computational grid for Geometry 1, $\delta_r = 15°$.

Figure 77: Computational grid for Geometry 1, $\delta_r = 30°$.

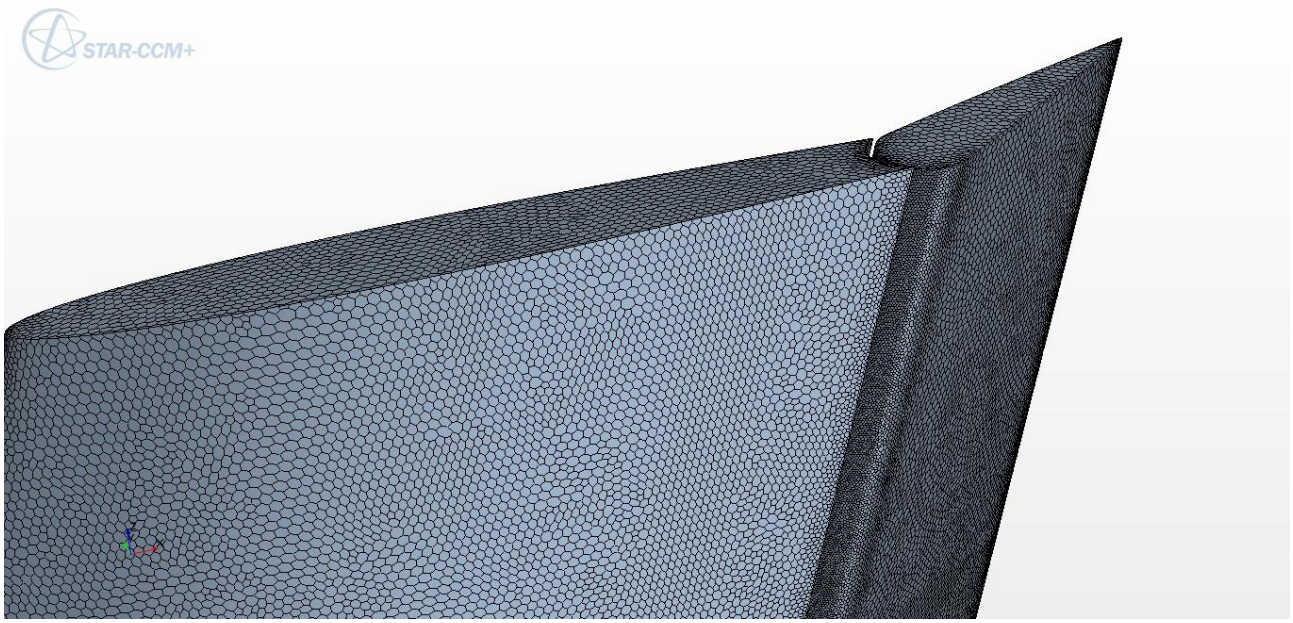

Figure 78: Detail of the computational grid for Geometry 1, $\delta_r = 30°$.

4.4 Analyses results

In this section are shown the most significant results of the analyses. The main purpose of these analyses, as previously stated, was to create an aerodynamic database that would allow to analyze the influence on the effectiveness of some fundamental geometric parameters of the vertical tail plane. For this purpose, it was made a comparison of all the results obtained for identical geometries that differed only in one of the parameters of interest (sweep angle, chords ratio, taper ratio, the nose shape of the mobile part, extension of the control surface). These comparisons are shown in Sections 4.4.1 to 4.4.5, in which is provided also an explanation of the obtained results.

All the reported results show the control surface effectiveness trend as a function of the deflection of the rudder. The effectiveness value for all the different deflections of the rudder, for each investigated geometry, was calculated using the expression shown in Figure 80, in which are shown the formulations of each term in the equilibrium equation about the yaw axis. In particular, the rudder control power $C_{N_{\delta_r}}$, observing the behavior of the yaw moment coefficient in function of the angle of sideslip β with the variation of the deflection of the rudder (see Figure 79 in which the

obtained curves can be considered parallel with the variation of δ_r) it was set equal to the derivative stability C_{N_β}, calculated using the classical definition of derivative between two points, multiplied by a factor equal to the effectiveness τ ($C_{N_{\delta_r}} = C_{N_\beta} \cdot \tau$). In the yaw equilibrium equation, the stability derivative C_{N_β} expression (in which the three multiplicative coefficients appear) is the one found in Ref. [13].

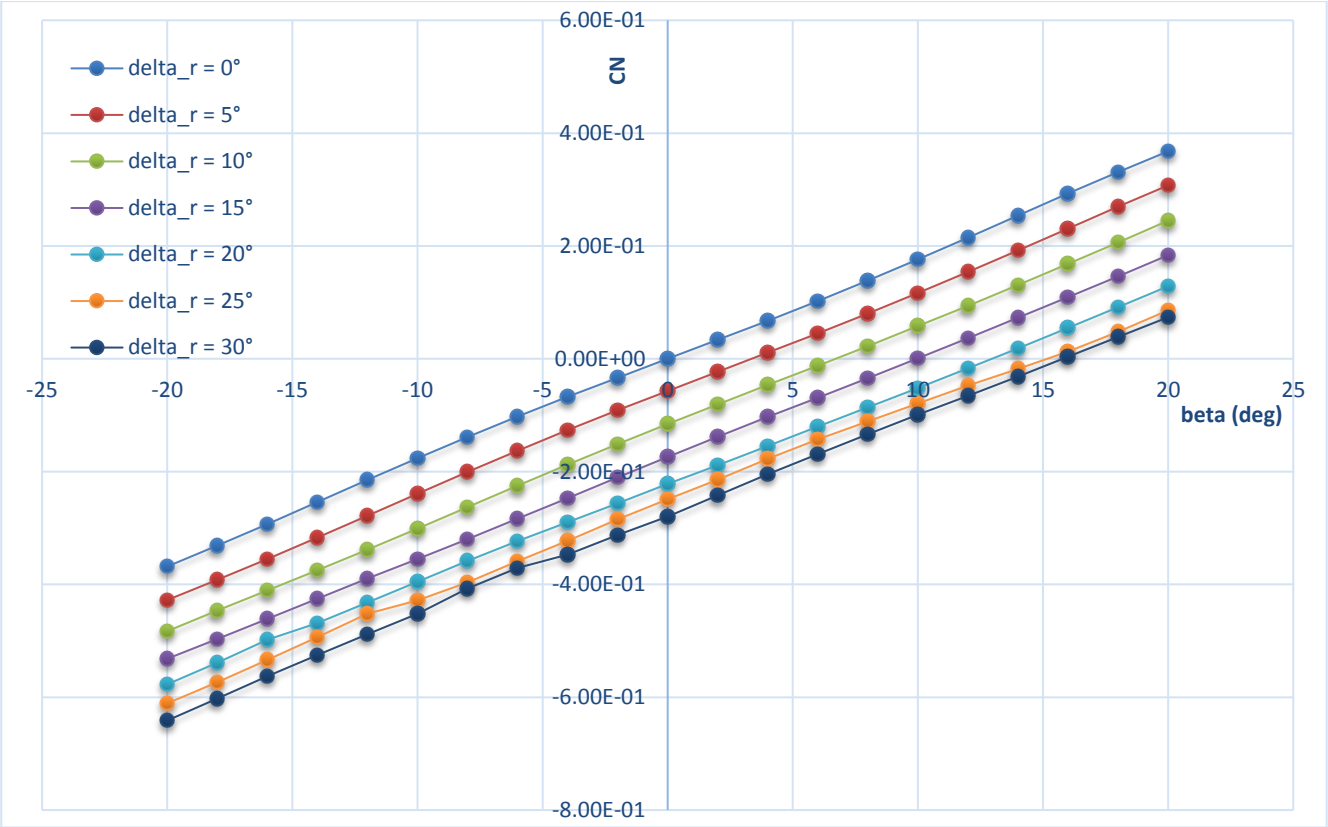

Figure 79: C_N trend as a function of β, found from the CFD analyses for Geometry 13.

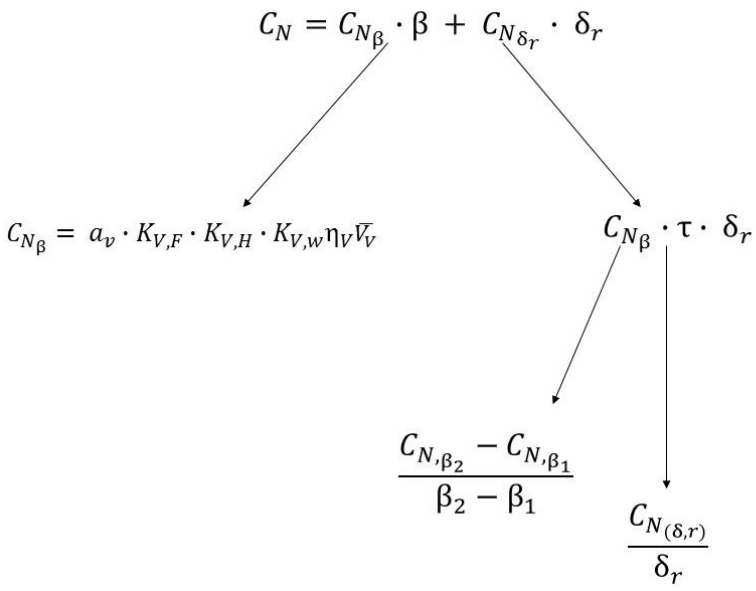

Figure 80: Expressions of all the terms in the equilibrium equation.

The effectiveness trend for some geometries of particular interest is reported in Figure 81 and Figure 82. The geometries chosen are the Geometries 1 and 7, which differ, in addition to the chords ratio, also for the nose shape (round for Geometry 1, elliptical for Geometry 7). A comparison was made between the results obtained from the CFD analyses and the results provided by the semi-empirical methods discussed in Chapter 2. As it can be seen, the different curves appear to provide quite similar results in the linear field of the moving surface deflections (despite appreciable differences, even of the order of 10%, can be encountered for some geometries), while in strongly nonlinear field (deflections greater than 15 degrees) there are big differences in the results, with definitely greater effectiveness values obtained from the numerical analyses. These differences may be explained considering that the semi-empirical methods derive from experimental analyses performed on horizontal tail planes geometries, with aspect ratios (AR) included between 4 and 5. The differences with respect to the analyzed geometries thus appear evident. It is also interesting to note how geometries with elliptical nose and high balance ratios (Figure 82) present an increase in effectiveness with the increasing of the rudder deflection, which is a situation not provided by the semi-empirical methods.

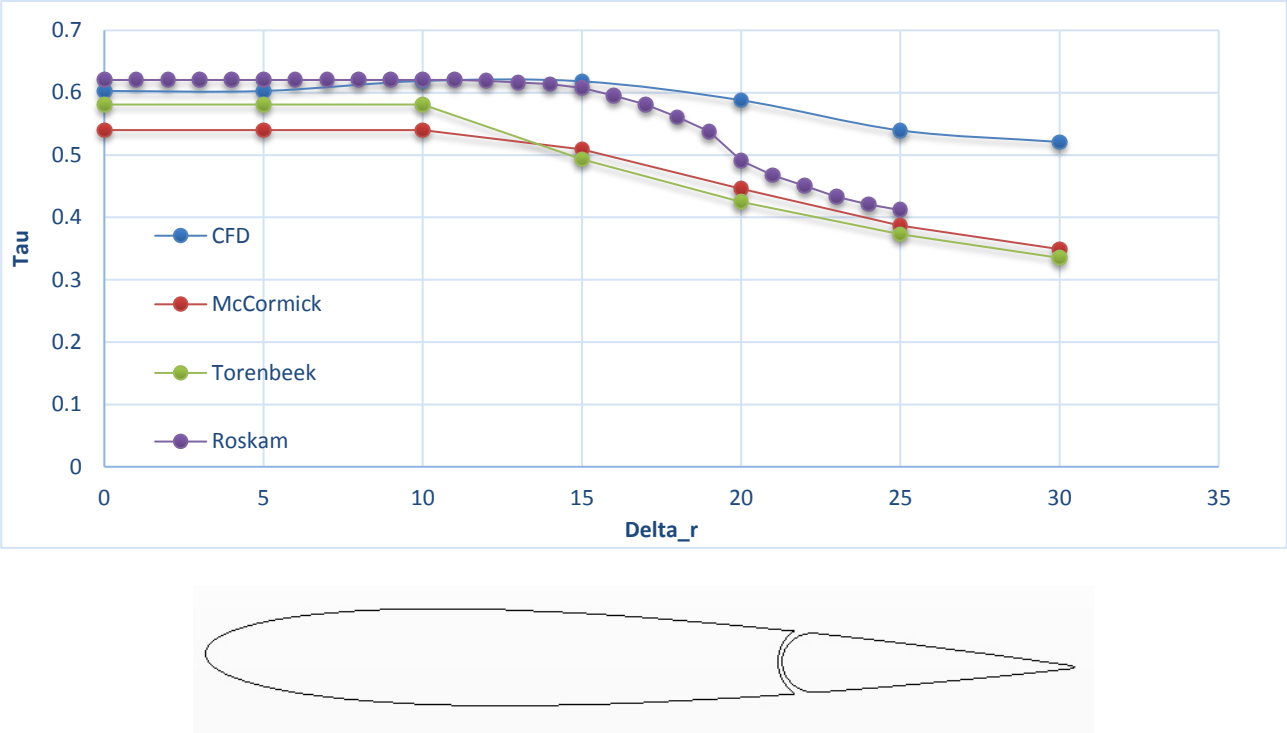

Figure 81: Effectiveness trend as a function of the rudder deflection, Geometry 1, comparison between semi-empirical and numerical results.

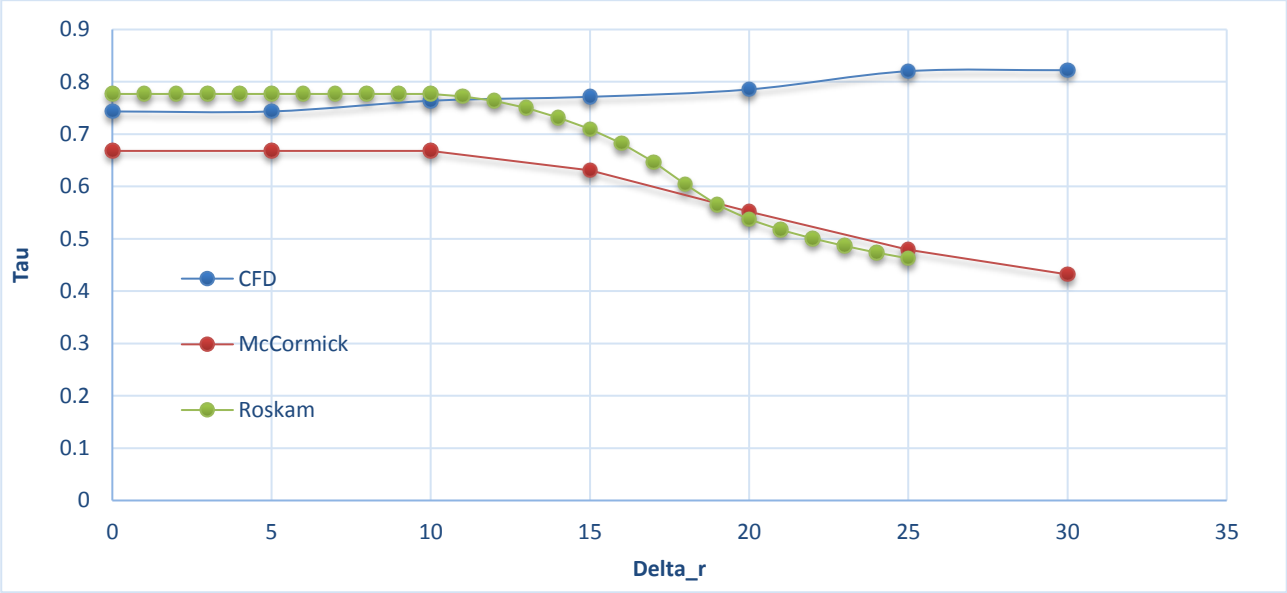

Figure 82: Effectiveness trend as a function of the rudder deflection, Geometry 7, comparison between semi-empirical and numerical results.

This situation leads to very different results, especially at high sideslip angles. This is particularly intense at high chord ratios, where the aerodynamics is such that the rudder effectiveness is constant or increasing. This behavior is due to three-dimensional effects. The effects of aspect ratio, sweep angle, and taper ratio are such to completely change the flow field around the body of interest. For instance, consider the reference geometry at 25° rudder deflection and 0° sideslip angle. Figure 83 shows a comparison between the airfoil at mac section and the corresponding 2D simulation, at the same farfield conditions. Pressure coefficient and velocity distributions are shown. In the 3D simulation, the suction happens at the rudder nose, while in the 2D simulation (wing with infinite span) the rudder deflection has the effect of an increase of the angle of attack. The flow is much more separated in the 2D case than in the section of the 3D simulation. Hence, the effectiveness at high deflection angles of vertical tails is explained.

This effect can be further enhanced with a high balance ratio. From the results of the test case on the horizontal tail plane presented in Section 3.2.1, Figure 84 shows the flow recirculation of a high balance ratio with an elliptical nose, leading to an increase in suction at control surface nose and a reduction of hinge moment. This is the principle of applying the aerodynamic balance.

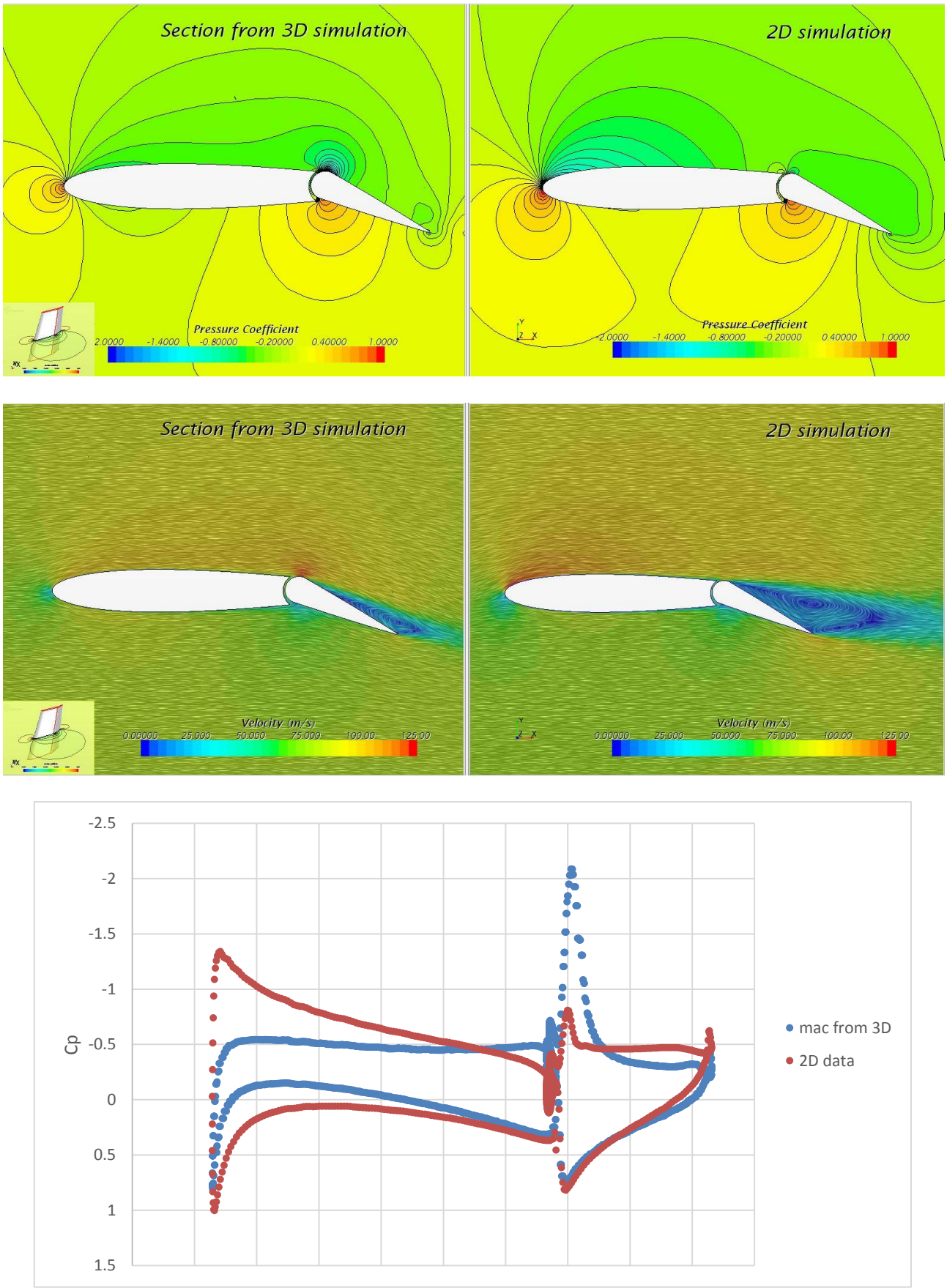

Figure 83: Comparison between 3D and 2D simulations at the same farfield conditions. M = 0, Re = 1.1E6, β = 0.

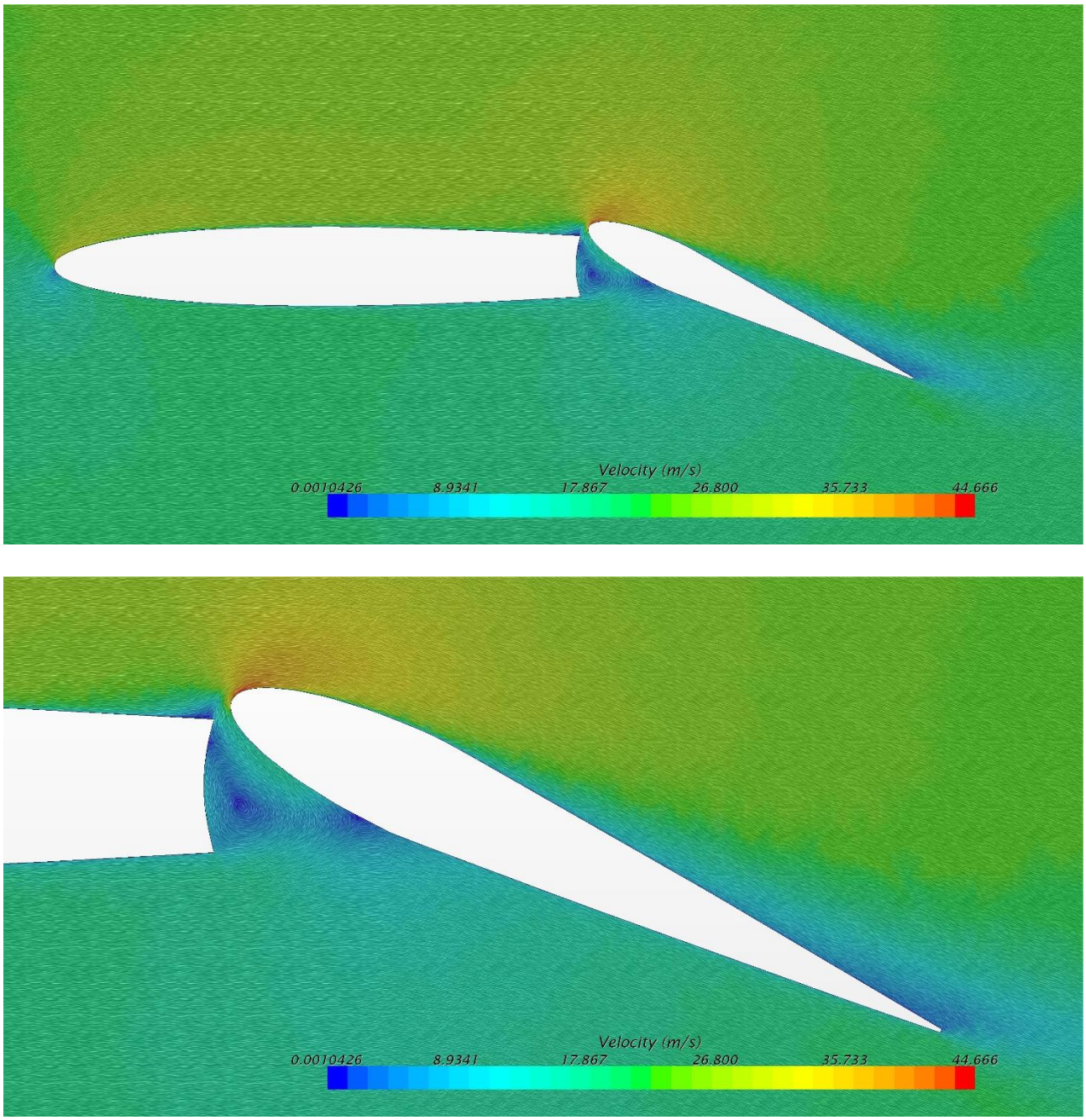

Figure 84: Effects of a high balance ratio with an elliptical nose. M = 0, Re = 1.43E6, β = 0.

4.4.1 Sweep influence on the effectiveness

The influence of the sweep angle to the leading edge on the effectiveness value can be clearly analyzed by observing Figure 85 and Figure 86. Both figures represent the comparison, in terms of effectiveness, between two identical geometries that differ only in the sweep angle value. As can be easily noted, a lower sweep angle to the leading edge allows to have a greater effectiveness value at low deflections of the movable surface, whereas at high deflections the situation is reversed, thus

providing a greater effectiveness value for greater sweep angles. Such behavior can be explained considering the role played in the aerodynamic field by the sweep angle, whose increase decreases the velocity component perpendicular to the vertical tail plane's leading edge, increasing the lower critical Mach number ($M_{\infty_{cr,inf}}$) and then delaying the vertical plane's stall, thus providing the increase in effectiveness found. The geometries considered for these comparisons are the number 19, 28, 2 and 13.

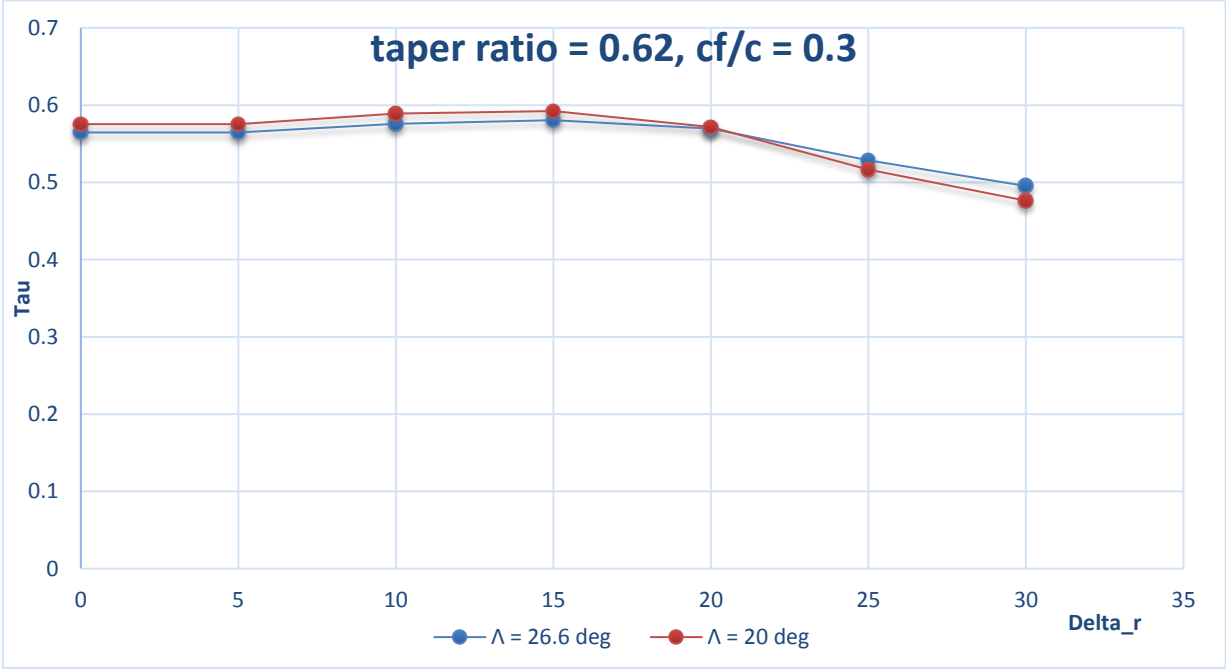

Figure 85: Effectiveness trend comparison for Geometry 19 (blue) and Geometry 28 (red).

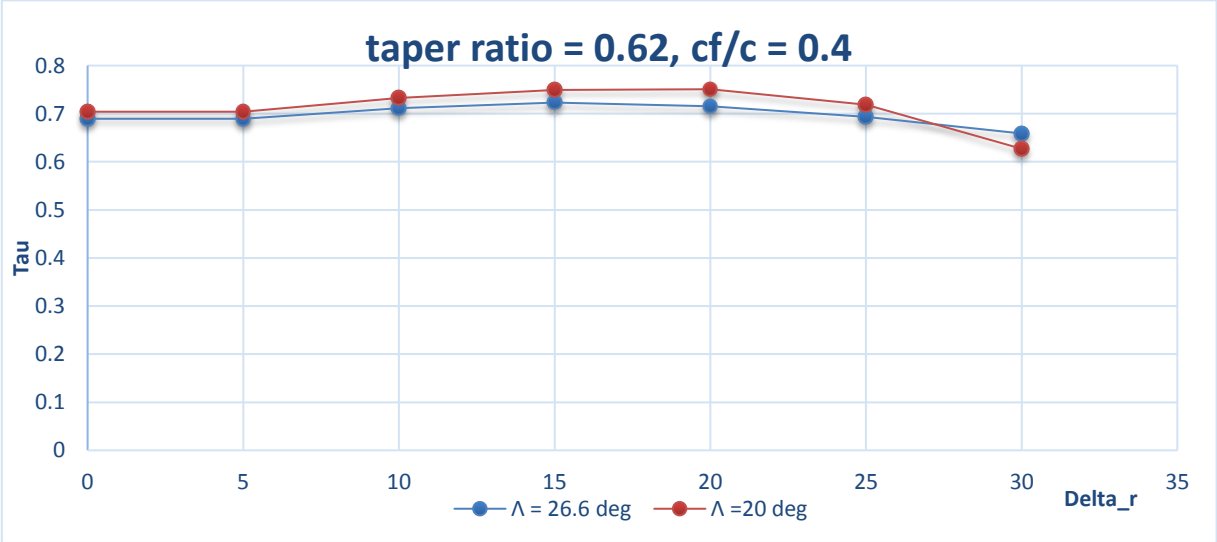

Figure 86: Effectiveness trend comparison for Geometry 2 (blue) and Geometry 13 (red).

4.4.2 Taper Ratio influence on the effectiveness

The influence of the taper ratio λ_V on the effectiveness value can be clearly analyzed by observing Figure 87 and Figure 88. Both figures represent the comparison, in terms of effectiveness, between three identical geometries that differ only in the taper ratio value. As can be easily noted, a lower taper ratio allows to have a greater effectiveness value, while the increase of this ratio decreases the effectiveness. Such behavior may be related to the aerodynamic load shifting with the increasing of the tip profile's chord length. However, further analyses are necessary to explain the genesis of this phenomenon. The geometries involved in the comparisons are the number 1, 5 and 6 in Figure 87, and 13, 14 and 15 in Figure 88.

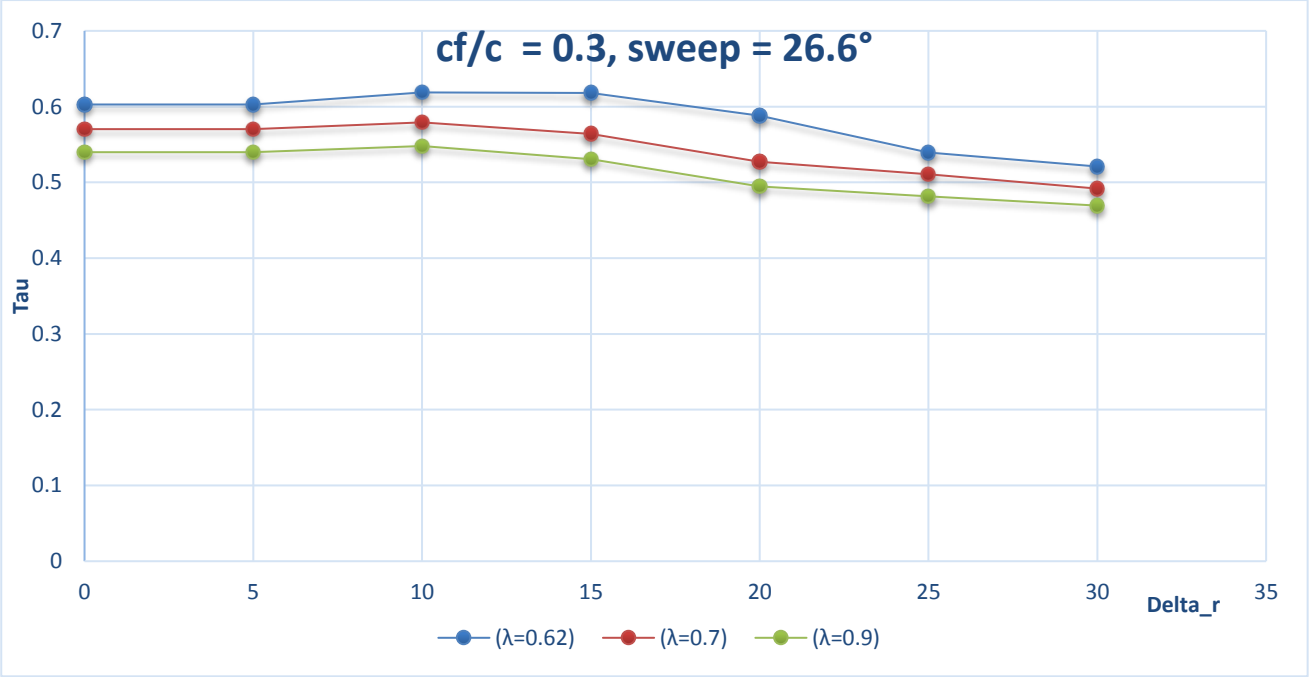

Figure 87: Effectiveness trend comparison for Geometry 1 (blue), Geometry 5 (red) and Geometry 6 (green).

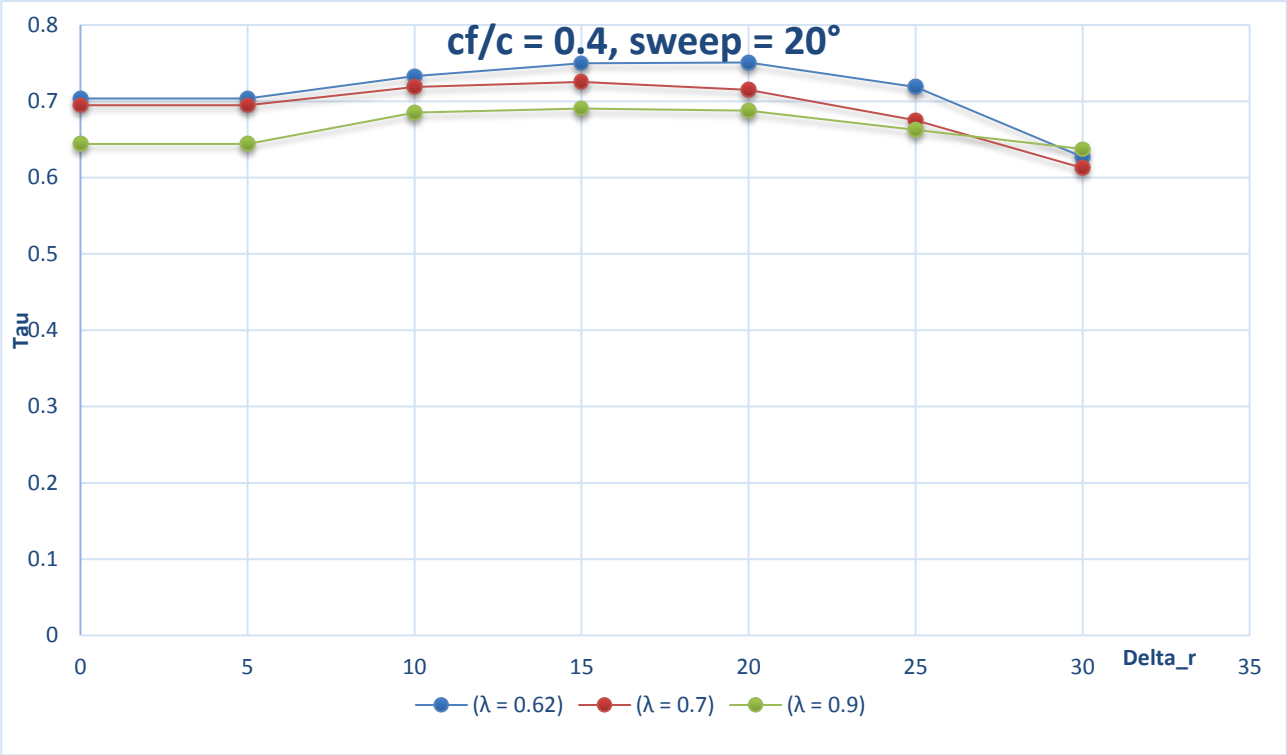

Figure 88: Effectiveness trend comparison for Geometry 13 (blue), Geometry 14 (red) and Geometry 15 (green).

4.4.3 Chord Ratio influence on the effectiveness

The influence of the chord ratio on the effectiveness value can be analyzed by observing Figure 89 and Figure 90. Both figures represent the comparison, in terms of effectiveness, between three identical geometries that differ only in the chord ratio value. As can be easily noted, a higher chord ratio, which increases the length of the flapped part with respect to the fixed part, allows to increase the effectiveness value (because of the greater contribution to the increase in lift coefficient with the increasing deflection of the movable part). Such influence is widely regarded also in the semi-empirical methods considered in Chapter 2. The geometries involved in the comparisons are the number 1, 2 and 7 in Figure 89, and 10, 13 and 16 in Figure 90.

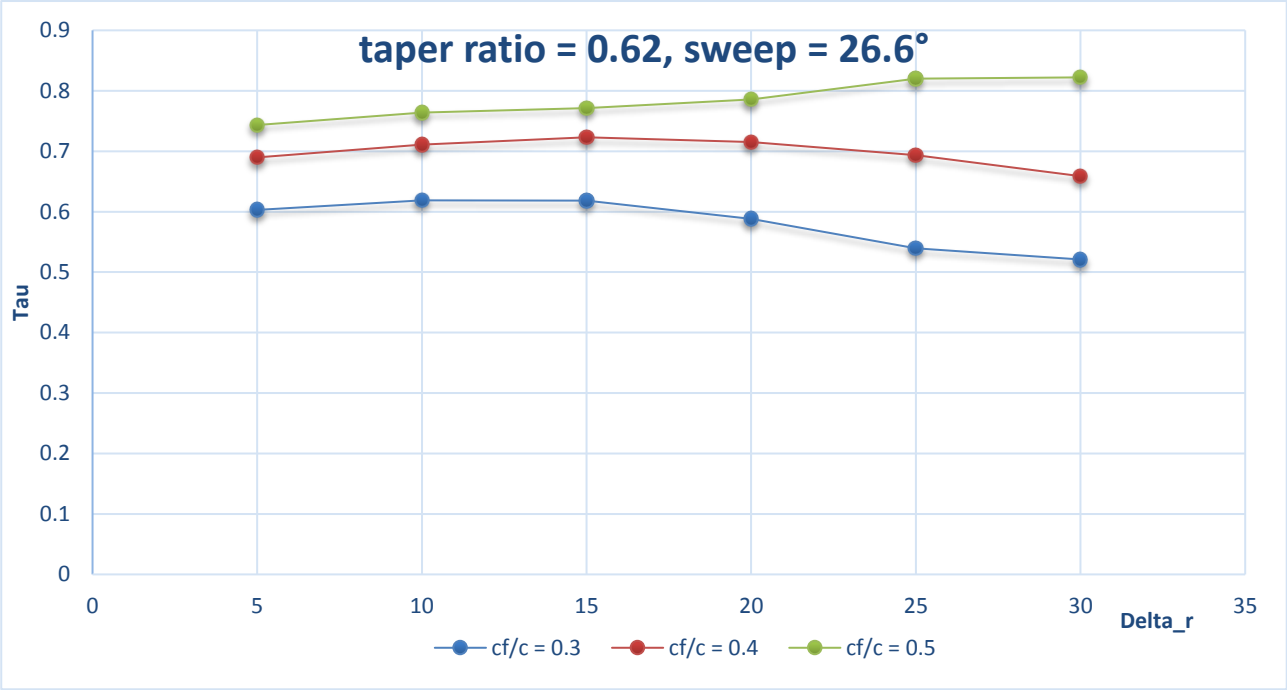

Figure 89: Effectiveness trend comparison for Geometry 1 (blue), Geometry 2 (red) and Geometry 7 (green).

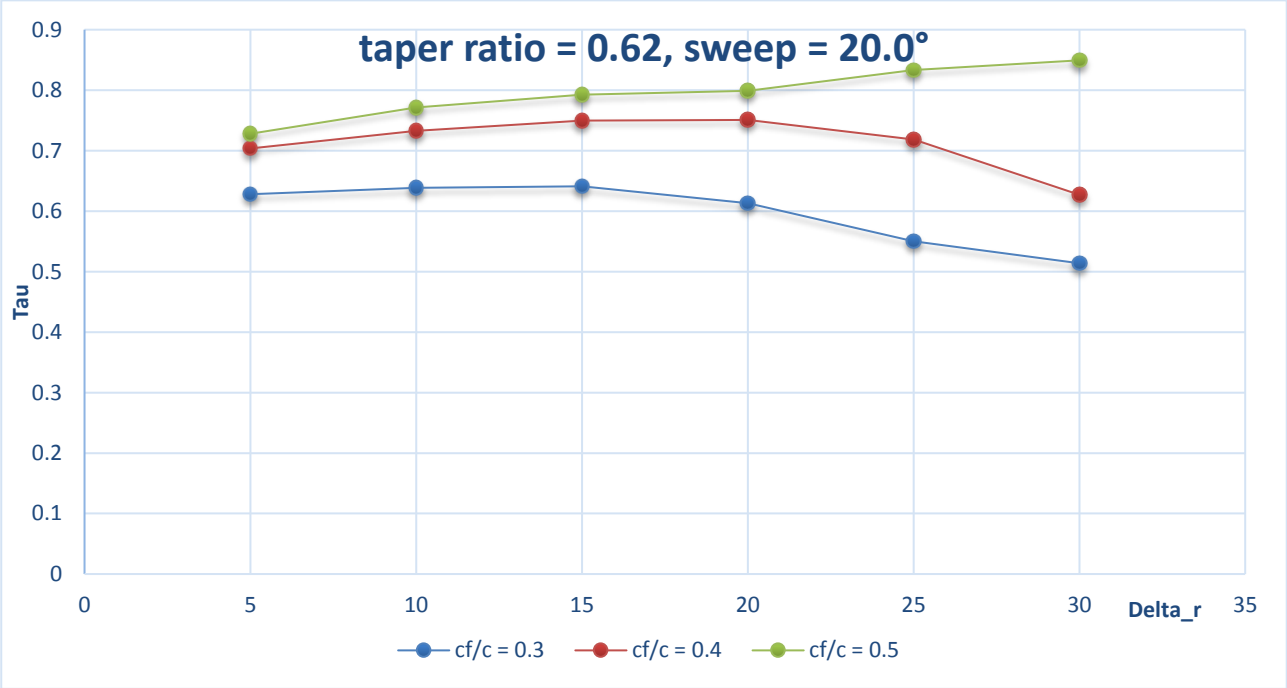

Figure 90: Effectiveness trend comparison for Geometry 10 (blue), Geometry 13 (red) and Geometry 16 (green).

4.4.4 Rudder extension along the span (η) influence on the effectiveness

The influence of the rudder extension along the vertical tail plane's span (η) on the effectiveness value can be analyzed by observing Figure 91 and Figure 92. Both figures represent the comparison, in terms of effectiveness, between two identical geometries that differ only in rudder extension along the span (η = 1 for geometries with rudder extended along all the span, η = 0.9 for geometries with rudder extended up to 90% of the span). As could be expected, geometries with rudder extended until the tip's chord (η = 1) present a higher effectiveness value. The geometries considered in the comparisons are the number 10, 28, 7 and 25.

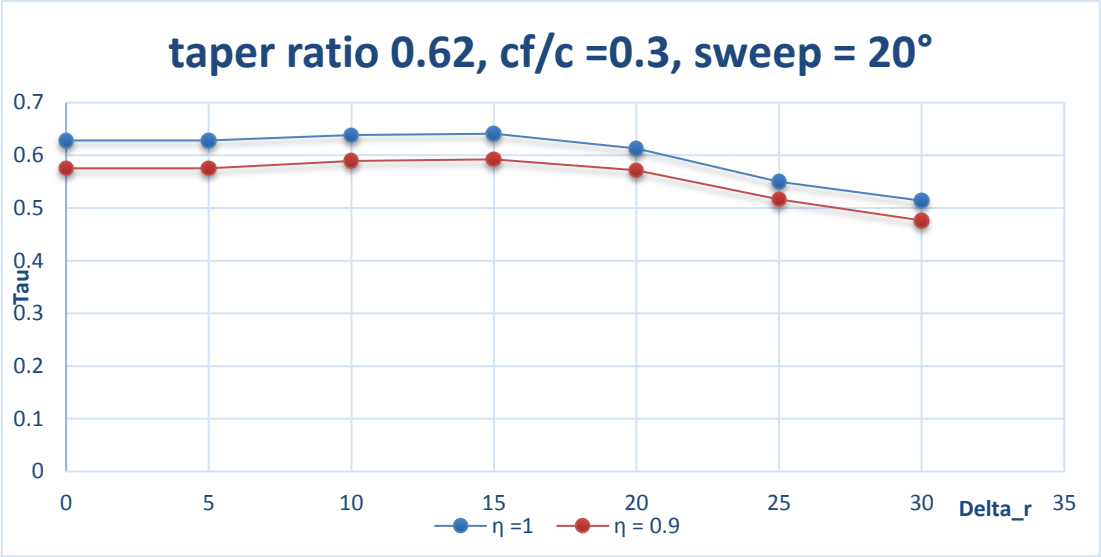

Figure 91: Effectiveness trend comparison for Geometry 10 (blue) and Geometry 28 (red).

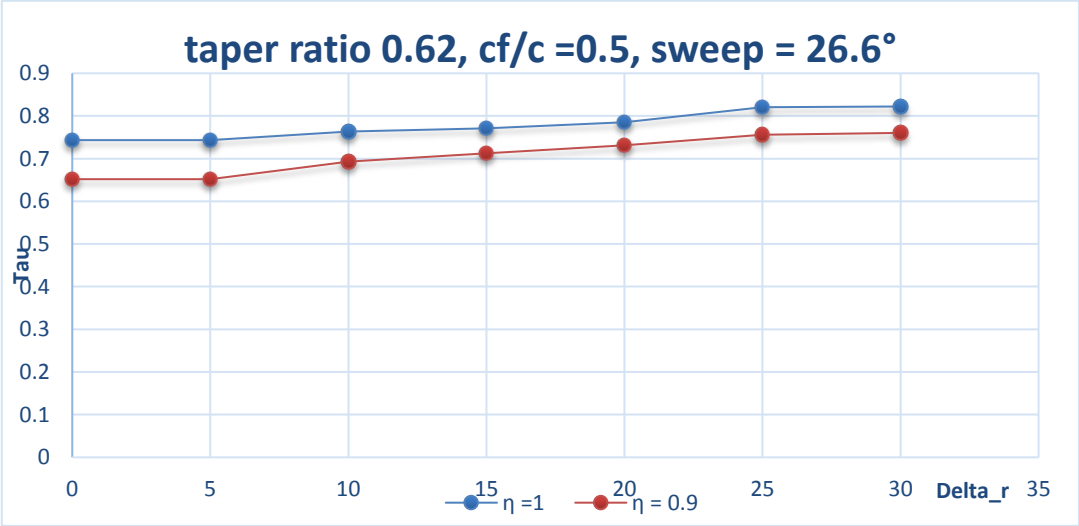

Figure 92: Effectiveness trend comparison for Geometry 7 (blue) and Geometry 25 (red).

4.4.5 Nose shape influence on the effectiveness

The influence of the mobile surface's nose shape on the effectiveness value can be analyzed by observing Figure 93. The following figure represents the comparison, in terms of effectiveness, between three identical geometries that differ only in the mobile part's nose shape. As can be seen, the effect of the nose shape seems to be quite bland, with little differences in terms of effectiveness values for the three analyzed configurations. For this reason, the influence of the nose shape on the effectiveness can be considered negligible and in section 4.5 will not be introduced any corrective coefficient for this parameter. The geometries considered in the comparisons are the number 1, 37 and 38.

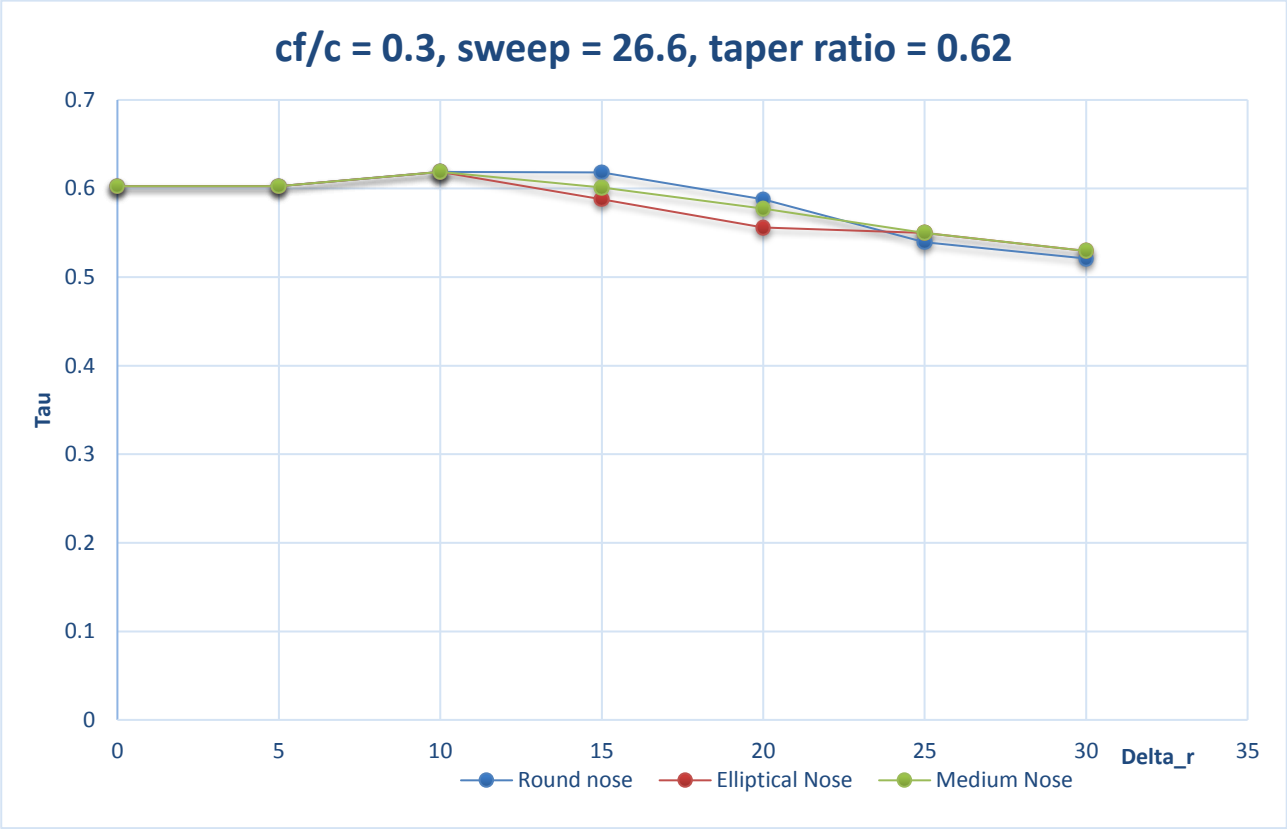

Figure 93: Effectiveness trend comparison for Geometry 1 (blue), Geometry 37 (red) and Geometry 38 (green).

4.5 New method for the calculation of the rudder effectiveness

The new method for the calculation of the rudder's effectiveness allows to obtain this parameter using the following equation

$$\tau_{new} = \tau\left(\delta_r, \frac{c_f}{c}\right) \cdot K_\lambda \cdot K_\eta \cdot K_\Lambda \qquad (4.2)$$

where the first parameter (τ), dependent on the chords ratio and the deflection of the control surface, as also provided by the semi-empirical methods, can be derived from Figure 94, obtained by appropriately interpolating the results of the numerical analyses. The maximum error committed by using this diagram is of the order of $\pm 2\%$, where the error is referred to the deviation of the curves from the CFD data.

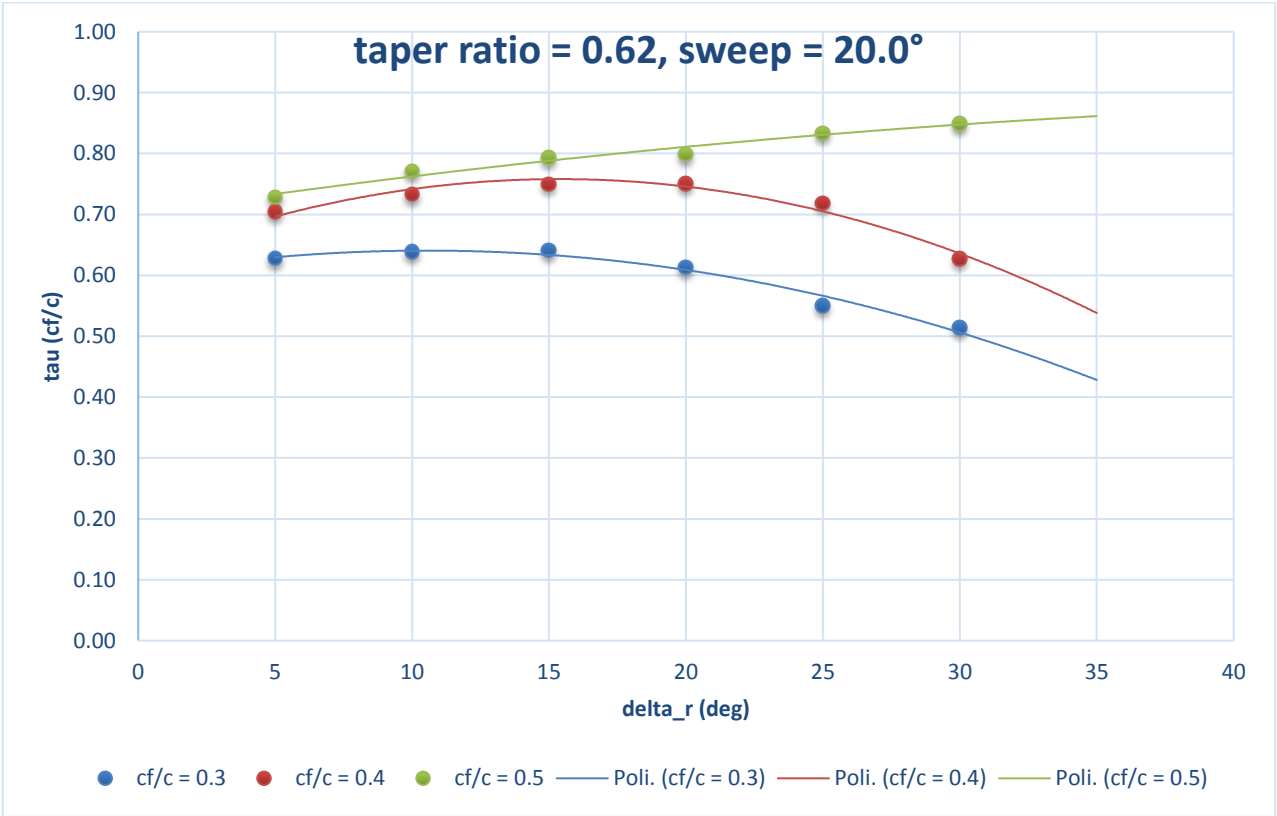

Figure 94: Effectiveness estimation as a function of the chords ratio and the rudder deflection.

In the equation (4.2) are also introduced three multiplier coefficients which take into account the influence of the taper ratio, the sweep angle and the extension of the rudder along the span. These influences have already been discussed in the previous sections, from 4.4.1 to 4.4.4.

The first coefficient, K_λ, takes into account the effect of the taper ratio, and can be obtained by the following equation

$$K_\lambda = -0.2097 \cdot \lambda + 1.1222 \qquad (4.3)$$

This equation was obtained by appropriately interpolating the numerical results, shown in Figure 95, in the same way as done for the $\tau\left(\delta_r, \frac{c_f}{c}\right)$ parameter. The maximum error can be obtained by the following equation

$$err_\lambda = \pm 0.07143 \cdot \lambda \mp 0.04429 \qquad (4.4)$$

in which the error is estimated with respect to the regression line and not with respect to the data, due to the strong scattering of the these (see Figure 95). This error results to be null for geometries with taper ratio equal to 0.62, while it is of the order of $\pm$2% for geometries with taper ratio equal to 0.9.

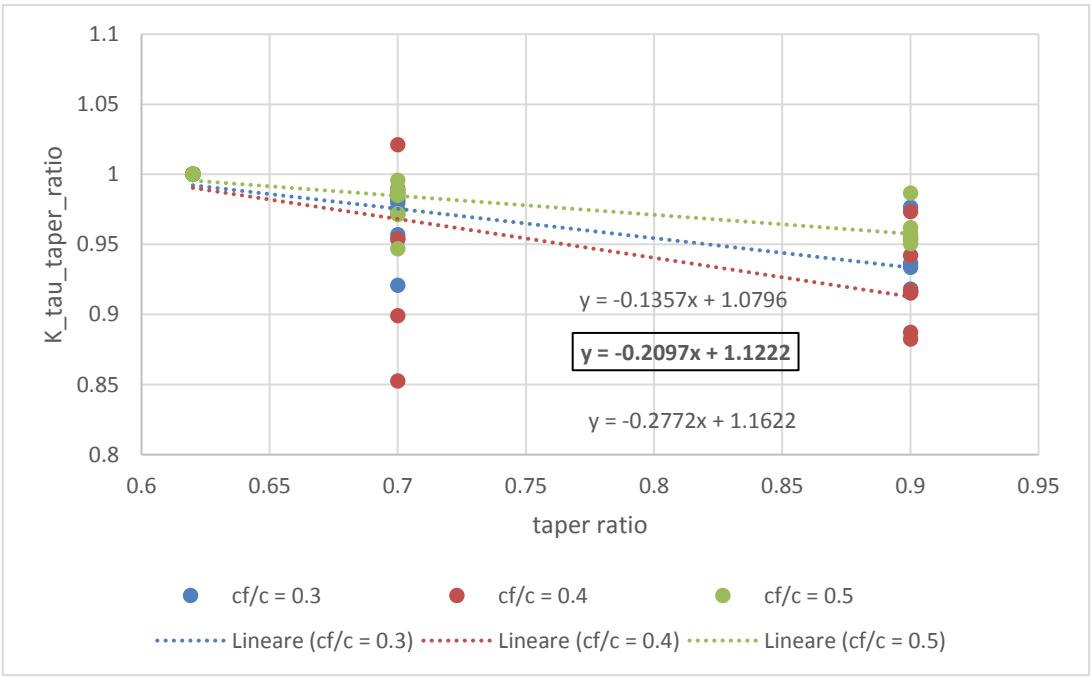

Figure 95: K_λ estimation as a function of the taper ratio.

The second coefficient, K_η, takes into account the effect of the rudder extension along the span, and can be obtained from the following equation

$$K_\eta = 0.7 \cdot \eta + 0.3 \qquad (4.5)$$

valid for $0.8 \leq \eta \leq 1.0$, obtained by a linear approximation of the numerical results (see Figure 96). The highest numerical error made by using this formula is of the order of $\pm 1\%$.

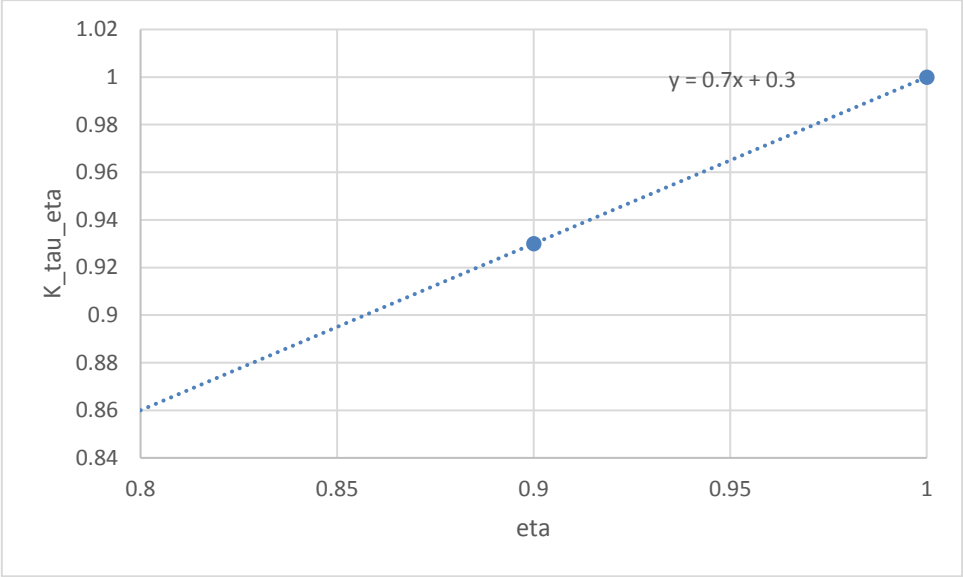

Figure 96: K_η estimation as a function of the rudder extension along the span.

The third coefficient, K_Λ, takes into account the influence on the effectiveness of the sweep angle at the leading edge, and can be obtained from the following equation

$$K_\Lambda = -0.0005 \cdot (\Lambda_V)^2 + 0.0207 \cdot (\Lambda_V) + 0.78 \qquad (4.6)$$

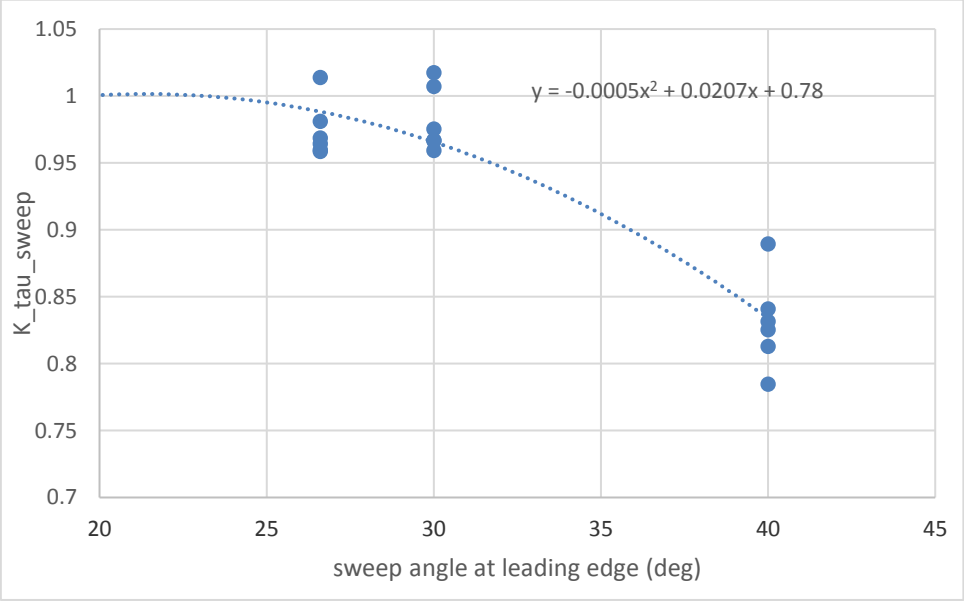

Figure 97: K_Λ estimation as a function of the sweep angle at leading edge.

obtained by a quadratic approximation of the numerical results (see Figure 97). The highest numerical error made by using this formula is of the order of $\pm 5\%$.

The maximum total error is given by the multiplication of all the maximum errors relating to each coefficient present in equation (4.2), and can be thus estimated equal to

$$err_{TOT} = (\pm 1.02) \cdot (\pm 1.02) \cdot (\pm 1.01) \cdot (\pm 1.05) \approx 10\%$$

which results to be an acceptable error during the preliminary design of the vertical tail plane. This error is the one made by using the simple formulas provided above, which do not take into account the actual rudder deflection but only the influence of the parameter of interest. For greater precision, it could be used curves at different rudder deflections.

After developing the method, comparisons were made to verify its validity. From Figure 98 to Figure 100 are shown the comparisons between the results obtained by applying the new method and the results obtained from the CFD analyses used to build it. In Figure 101, instead, is shown the comparison between the results obtained by the new method and the results obtained from numerical analyses and wind tunnel tests carried out by the DAF research group for the vertical tail plane of the Tecnam P2012. The results appear to be very close to those obtained previously, with a maximum error that settles down, as expected, around 10%. In particular, the compliance with the wind tunnel tests (performed on the complete aircraft model, with both dorsal fin and horn balance) appears to be almost total (with a maximum error of 3%), except for the results obtained at high angles of rudder deflections. All these considerations make it possible to state that the developed method seems to be more than reliable.

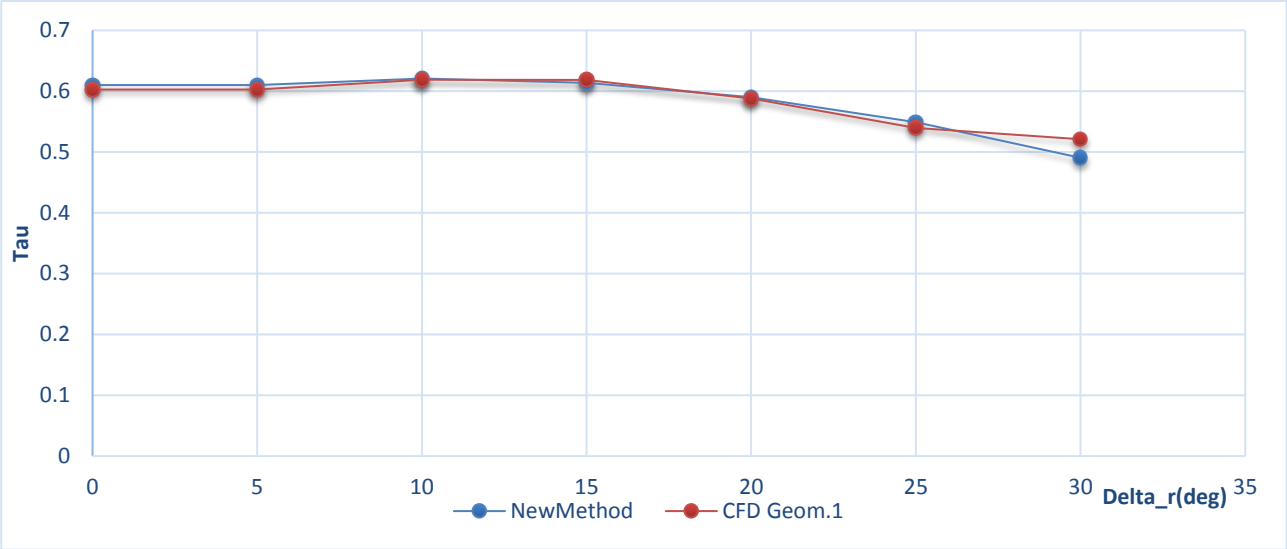

Figure 98: Effectiveness comparison between CFD and New Method results for Geometry 1. Maximum error equal to 5.9%.

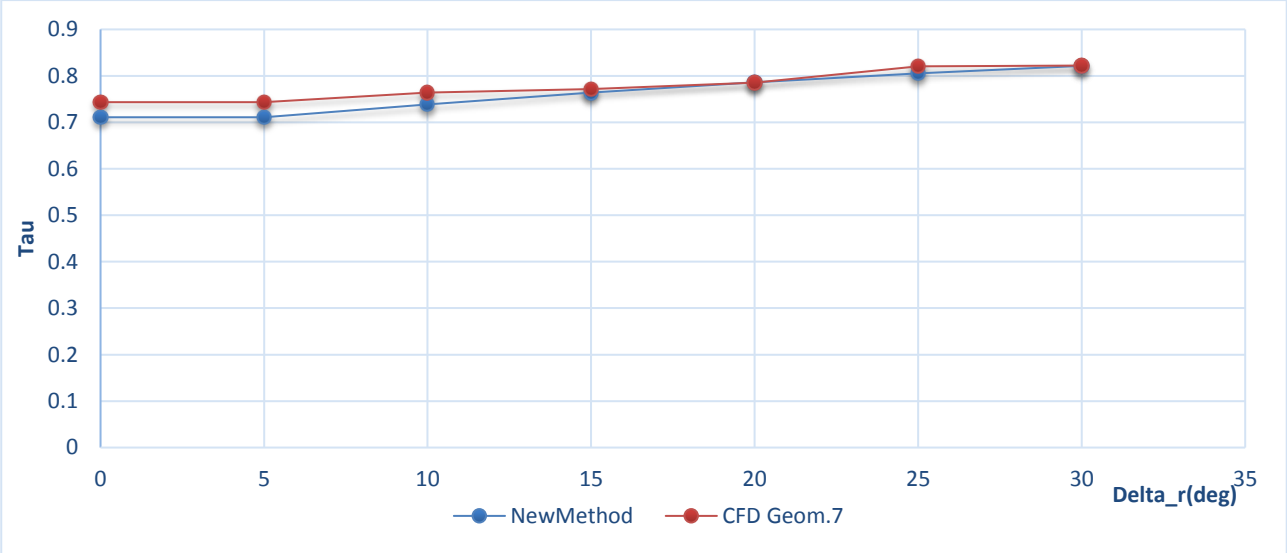

Figure 99: Effectiveness comparison between CFD and New Method results for Geometry 7. Maximum error equal to 4,4%.

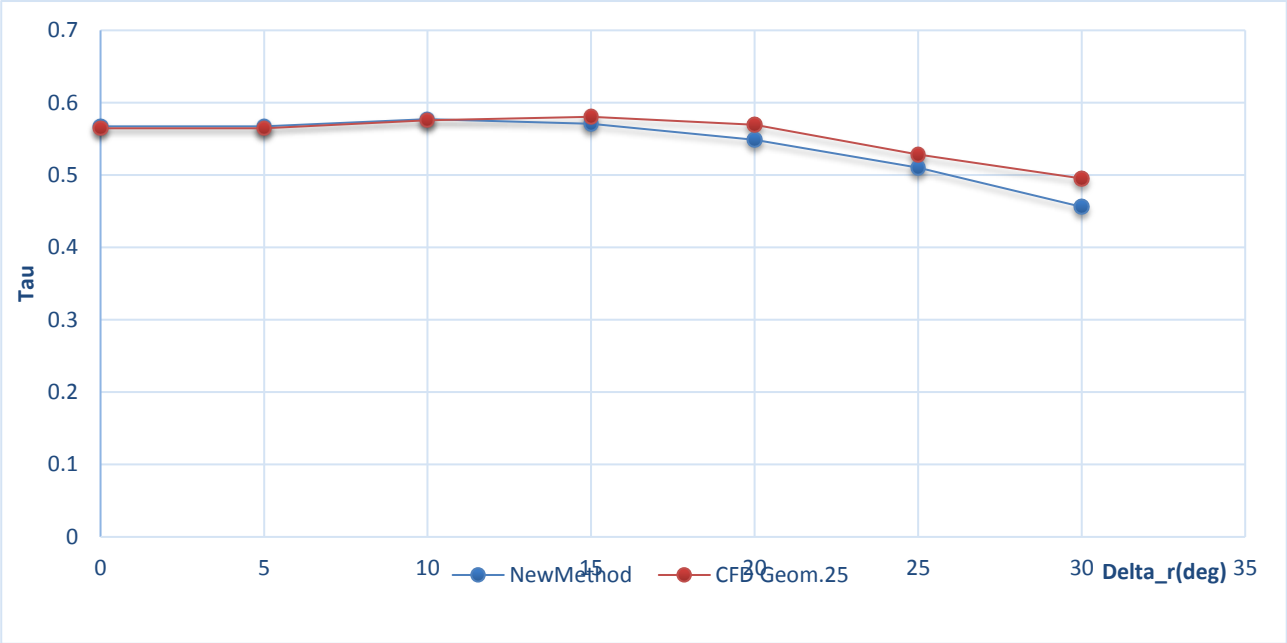

Figure 100: Effectiveness comparison between CFD and New Method results for Geometry 25. Maximum error equal to 7,9%.

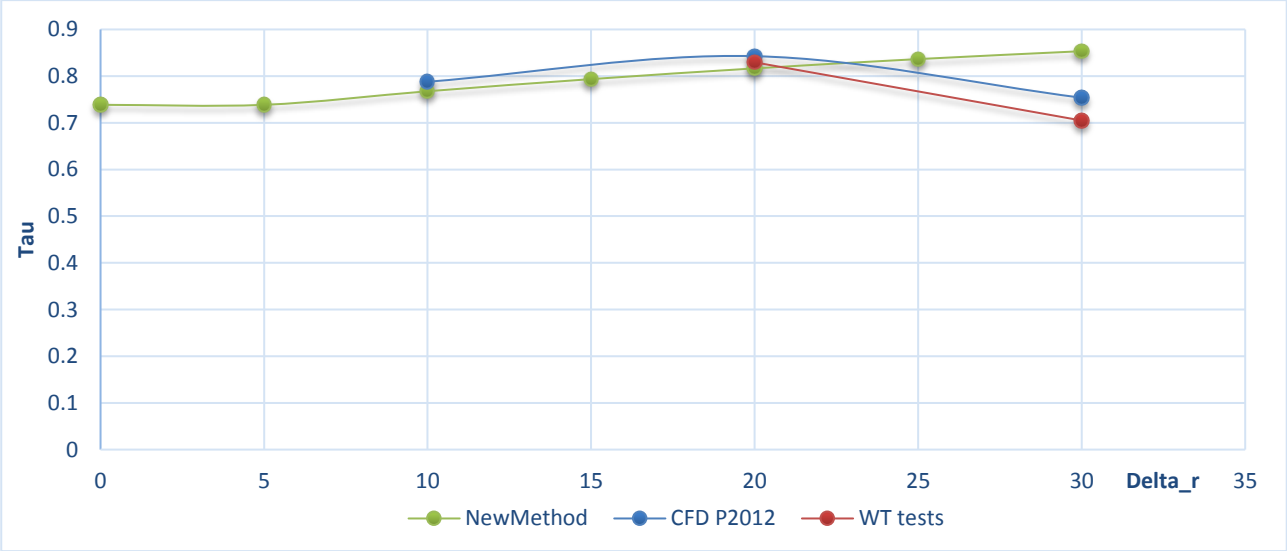

Figure 101: Effectiveness comparison between CFD, wind tunnel tests and New Method results for P2012 vertical tail plane.

5 Conclusion

The objective of this thesis work was to implement a new preliminary design procedure for the estimation of the rudder effectiveness, through the Computational Fluid Dynamics. As a matter of fact, vertical tail plane's design necessarily passes through the determination of the control derivatives and the more accurate the latter, the better the former. At time of writing, several semi-empirical methods exist for the determination of the rudder effectiveness. All of them evaluate this parameter by means of semi-empirical factors to account for the effect of the chords ratio, the rudder deflection and others. These methods have the great advantage of being quickly applied and easy to understand, but at the same time involve great disadvantages. First of all, they do not take into account the influence of other vertical tail plane's geometric parameters (leading edge sweep, taper ratio ecc.). Furthermore, the non-linear effects are not taken into account in the correct way (these effects drastically reduce the effectiveness for deflections of rudder greater than 15 degrees). This latter effect is probably due to the relatively higher aspect ratio of the planforms presented in literature, while vertical tail planes usually have an aspect ratio around 1.5.

The semi-empirical methods, proposed on the Roskam, Torenbeek and McCormick texts, although starting from the same basic theory, come to different results in the linear field (small deflections of the rudder) and also in non-linear field (large deflections of the rudder). In particular, the one proposed by Roskam is the most complete, as it takes into account the effects on the effectiveness of a great number of geometric parameters, while the methods proposed in Torenbeek and McCormick texts are easier to use, due to the reduced number of data to take into account.

Once reviewed these issues, a new method was realized from the results of numerical analyses.

Nowadays computing power permits complex CFD analyses both on desktop computers and cluster grids. For the purpose of this work, the commercial software Star-CCM+ was used, both in local and on the SCoPE University's computational grid. Several test cases, excerpted from the same NACA reports to which semi-empirical methods are based, were simulated to verify the compliance of CFD results to the experimental data and the results were comforting. After this compliance, the

analyses for the definition of the new procedure, objective of this work, were planned. An analysis matrix was built, with 40 different vertical tail planes geometries. The dimensions of the CAD model were dictated by the size of previous wind tunnel tests conducted at the Department of Industrial Engineering of the University of Naples. The results of the numerical analyses have conducted to the implementation of a new method for the calculation of the rudder effectiveness. This method allows, through the use of appropriate corrective coefficients, to take into account, in the evaluation of the parameter of interest, the sweep angle to the leading edge, the taper ratio and the extension of the rudder along the span. This result is of considerable interest, since it provides results that agree with recent numerical and experimental analyses on regional and general aviation airplanes (P2012 numerical and wind tunnel tests, [26]). Experimental tests are to be conducted in the future on the most relevant geometries to validate the method.

Bibliography

[1] Ilan Kroo and Juan Alonso. *Tail design and sizing*. Stanford University, 2012. url:http://adg.stanford.edu/aa241/stability/taildesign.html.

[2] *Free online private pilot ground school*. 2012. url: http://www.free-online-private-pilot-ground-school.com/aircraft-structure.html.

[3] *Virtual skies*. 2012. url:http://quest.arc.nasa.gov/aero/virtual/demo/aeronautics/tutorial/structure.html.

[4] Courtland D. Perkins and Robert E.Hage. *Airplane performance stability and control*. Wiley, 1949.

[5] Lab 8 notes – *Basic aircraft design rules*. Massachusetts Institute of Technology. 2006. url:http://ocw.mit.edu/courses/aeronautics-and-astronautics/16-01-unified-engineering-i-ii-iii-iv-fall-2005-spring-2006/systems-labs-06/spl8.pdf.

[6] Egbert Torenbeek. *Synthesis of subsonic airplane design*. Delft University Press, 1976.

[7] Ed Obert. *Aerodynamic design of transport aircraft*. Delft, The Netherlands: Delft University of Technology, 2009.

[8] Daniel P. Raymer. *Aircraft design: a conceptual approach*. American Institute of Aeronautics and Astronautics, 2004.

[9] Snorri, Gudmundsson, *General Aviation Aircraft Design: Applies Methods And Procedures*, Elsevier, 2014.

[10] Robert Thomas Jones, *Wing Theory*, 1990.

[11] R. D. Finck, Hoak et al. *USAF Stability and Control DATCOM*. AFWAL-TR- 83-3048. Flight Control Division, Air Force Flight Dynamics Laboratory.Wright Patterson Air Force Base, Ohio: McDonnell Douglas Corporation, 1978.

[12] Pierluigi Della Vecchia, Danilo Ciliberti, *Numerical Aerodynamic Analysis On A Trapezoidal Wing With High Lift Devices: A Comparison With Experimental Data*, XXII AIDAA Conference, Napoli (Italy), September 9-12, 2013.

[13] Danilo Ciliberti, Fabrizio Nicolosi, Pierluigi Della Vecchia, *A New Vertical TailPlane Design Procedure Through CFD*, Università degli Studi di Napoli Federico II, 2012.

[14] Fabrizio Nicolosi, Pierluigi Della Vecchia, and Salvatore Corcione. *Aerodynamic analysis and design of a twin engine com-muter aircraft*. In: The International Congress of the Aeronau-tical Sciences. 2012.

[15] Jan Roskam. *Airplane design part VI: preliminary calculation of aerodynamic, thrust and power characteristics*. DAR Corporation, 1997.

[16] Barnes W. McCormick, *Aerodynamics, Aeronautics, and Flight Mechanics*, Wiley; 2 edition (September 13, 1994)

[17] P. D. Chappell, R. W. Gilbey, et al. *Lift-curve slope and aerodynamic centre position of wings in inviscid subsonic flow*. Item 70011. Engineering Science Data Unit, 1970.

[18] J.G. Callaghan *Aerodynamic prediction methods for aircraft at low speeds with mechanical high lift aids*, AGARD Lecture Series 67, May 1974.

[19] H. Glauert: *Theoretical relationships for an airfoil with hinged flap*. ARC Rand M No. 1095, 1927.

[20] J.A. Hay.and W.J. Eggington, *An exact theory of a thin aerofoil with large flap deflection*. J. Royal Aero. Soc. Val. 60 (551), Nov. 1956, pp. 753-757.

[21] J.G. Lawry and E.C. Polhamus: *A method far predicting lift increment due to flap deflection at low angles of attack*. NACA TN 3911, 1957.

[22] Cahill, J. F., *Summary of Section Data on Trailing-Edge High-Lift Devices*, NACAR 938, 1949.

[23] Harris, T. A, and Recant, I. G., *Wind Tunnel Investigation of NACA 23012, 23021, and 23030 Airfoils Equipped with 40-Percent Chord Double Slotted Flaps*, N ACAR 723, 1941.

[24] Kelly, J. A., and Hayter, N. F., *Lift and Pitching Moment at Low Speeds of the NACA 64A010 Airfoil Section Equipped with Various Com-binations of a Leading-Edge Slat, Leading-Edge Flap, Split Flap, and Double-Slotted Flap,* NACA TN 3007, September 1953.

[25] Wenzinger, C. J., and Rogallo, F. M., *Rèsumè of Air-Load Data on Slats and Flaps*, NACA TN 690, March 1939.

[26] P. Della Vecchia et al., P2012 WT test report. Unpublished data.

[27] Star-CCM+ *Version 6.06.017 User Guide*. CD-adapco. 2011.

[28] Leonardo Merola. *The SCoPE project*. Final workshop of grid projects 'PON ricerca 2000-2006, avviso 1575'. Università degli studi di Napoli 'Federico II', 2006.

[29] I. Elizabeth Garner, NACA, Wartime Report: *Wind-Tunnel Investigation Of Control-Surface Characteristics: XX - Plain And Balanced Flaps On An NACA 0009 Rectangular Semispan Tail Surface*, October 1944.

[30] Sears, Richard I.: *Wind-Tunnel Data on the Aerodynamic Characteristics of Airplane Control Surfaces.* NACA ACR No. 3L08, 1943.

[31] Wenzinger, Carl J., and Harrìs, Thomas A.: *The Vertical Wind Tunnel of the National Advisory Committee for Aeronautics*. NACA Rep. No. 387, 1931.

[32] Sears, Richard I., and Hoggard, H. Page, Jr.: *Wind Tunnel Investigation of Control Surface Characteristics. II - A Large Aerodynamic Balance of Various Nose Shapes with a 30-Percent-Chord Flap on an NACA 0009 Airfoil*. NACA ARR, Aug. 1941.

[33] D.Ciliberti, F.Nicolosi, L. De Luca: *An improved preliminary design methodology for aircraft directional stability prediction and vertical tailplane sizing.* March 2016.

[34] Vos, J. B. et al., *Navier-Stokes solvers in European aircraft design*. In: *Progress in Aerospace Sciences* 38.8 (2002), pp. 601–697.

[35] Smith, W. G. and Ball, L. H., *Static Lateral-Directional Stability Characteristics of Five Contemporary Airplane Models From Wind-Tunnel Tests at High Subsonic and Supersonic Speeds*. Research Memorandum.National Advisory Committee for Aeronautics, 1956.

[36] Lan, C. E., *Calculation of Lateral-Directional Stability Derivatives for Wing-Body Combinations with and without Jet-Interaction Effects.* Contractor Report 145251. National Aeronautics and Space Administration,1977.

[37] Hall, R. M. et al., *Computational Methods for Stability and Control (COMSAC): the time has come.* Tech. rep. 6121. American Institute of Aeronautics and Astronautics, 2005.

[38] Erickson, L. L., *Panel methods: An introduction*. Vol. 2995. National Aeronautics, Space Administration, Office of Management, Scientific,and Technical Information Division, 1990.

[39] Terzi, A. and Chiu, T. W., *Modern panel method techniques for modeling wake body interference*. In: AIAA Paper 97.1829 (1997).

[40] Obert E., *Tail design. Report H-0-93*. Amsterdam (Netherlands): Fokker Aircraft B.V, 1992.

[41] Hucho W., *Aerodynamics of Road Vehicles: From Fluid Mechanics to Vehicle Engineering*. Elsevier Science, 2013. url:https://books.google.it/books?id=psP8BAAAQBAJ.

[42] Dutt, H. and Rajeswari, S. *Wing-body interference using a hybrid panel method*. In: *Acta mechanica* 106.3-4 (1994), pp. 111–126.

[43] Lamb, M., Sawyer, W. C., and Thomas, J. L. *Experimental and theoretical supersonic lateral-directional stability characteristics of a simplified wing-body configuration with a series of vertical-tail arrangements*. Technical Paper 1878. National Aeronautics and Space Administration, 1981.

[44] Park, M. A. et al. *Determination of stability and control derivatives using computational fluid dynamics and automatic differentiation*. In: *Proceedings of the 17th AIAA Applied Aerodynamics Conference*. 1999.

[45] Johnson, F. T., Tinoco, E. N., and Yu, N. J. *Thirty years of development and application of CFD at Boeing Commercial Airplanes, Seattle*. In: *Computers & Fluids* 34.10 (2005), pp. 1115–1151.

[46] Shang, J. S. *Three decades of accomplishments in computational fluid dynamics*. In: *Progress in Aerospace Sciences* 40.3 (2004), pp. 173–197.

[47] Fujii, K. *Progress and future prospects of CFD in aerospace – Wind tunnel and beyond*. In: *Progress in Aerospace Sciences* 41.6 (2005), pp. 455–470.

[48] Anderson, J. D. *Computational fluid dynamics: the basics with applications*. Mcgraw-Hill, 1995.

[49] O'Neill, C. R. *Determination of flight stability coefficients using a finite element CFD*. Tech. rep. 74077. Stillwater, Oklahoma: Department of Mechanical and Aerospace Engineering, Oklahoma State University,2000.

[50] Papa, R., de Mattos, B. S., and de Castro Santos, L. C. *Considerations about forward fuselage aerodynamic design of a transport aircraft*. In: AIAA Paper (2004).

[51] Rivers, M. B. and Dittberner, A. *Experimental investigations of the NASA common research model in the NASA Langley national transonic facility and NASA Ames 11-ft transonic wind tunnel*. In: AIAA Paper 1126 (2011), p. 2011.

[52] Rudnik, R., Huber, K., and Melber-Wilkending, S. *EUROLIFT Test Case Description for the 2nd High Lift Prediction Workshop*. In: 30th AIAA Applied Aerodynamics Conference. 2012, pp. 25–28.

[53] Rumsey, C. L. et al. *Summary of the first AIAA CFD high-lift prediction workshop*. In: Journal of Aircraft 48.6 (2011), pp. 2068–2079.

[54] Levy, D. W. et al. *Summary of data from the fifth AIAA CFD drag prediction workshop*. In: AIAA Paper (2013).

[55] Spalart, P. R. and Allmaras, S. R. *A one equation turbulence model for aerodinamic flows*. In: AIAA Journal 94 (1992).

[56] Della Vecchia, P. and Ciliberti, D. *Numerical aerodynamic analysis on a trapezoidal wing with high lift devices: a comparison with experimental data*. In: 22th AIDAA Conference. Associazione Italiana di Aeronautica e Astronautica, 2013.

[57] SCoPE. Università degli studi di Napoli 'Federico II'. 2016. url: http://scope.unina.it/

[58] Fabrizio Nicolosi, Danilo Ciliberti, and Pierluigi Della Vecchia. "Aerodynamic Design Guidelines of Aircraft Dorsal Fin", 34th AIAA Applied Aerodynamics Conference, AIAA AVIATION Forum, (AIAA 2016-4330) http://dx.doi.org/10.2514/6.2016-4330